

Master's Thesis

**Verification of simulated precipitation on the
LES scale with focus on its convective evolution**

Submitted by

Patrick Hartung

Hamburg, March 30, 2016

Supervised by

Prof. Dr. Felix Ament
Dr. Verena Grützun

University of Hamburg
Meteorological Institute

Master's Thesis of Patrick Hartung:

Title: Verification of simulated precipitation on the LES scale with focus on its convective evolution

Theme: Verification of simulated precipitation on the LES scale with focus on its convective evolution using radar data and an automated precipitation extrapolator

Universität Hamburg
Fakultät für Mathematik, Informatik und Naturwissenschaften
Studiengang Meteorologie



Foto: Patrick Hartung

Abstract

In this master's thesis the convective evolution of simulated precipitation is investigated and verified on the LES scale [Large Eddy Simulation] with the help of X-band radar measurements in the context of the project HD(CP)² [High Definition Clouds and Precipitation for Climate Prediction]. The specific task is to extract this convective evolution from the total temporal evolution of the precipitation. For this, the nowcasting tool APEX [Automated Precipitation Extrapolator] by Van Horne (2003) is used. It identifies, tracks and extrapolates rainfall areas from available precipitation data. As the forecasted fields only contain advective rainfall the convective evolution can be determined simply by subtraction from the observed or simulated data. Because of the strictly separate consideration of measured and modeled data it is possible to compare particularly the behavior of the convective evolution by different verification scores instead of evaluating the quality of the forecast. The used data originate on the one hand from the PATTERN [Precipitation and Attenuation Estimates from a High Resolution Weather Radar Network] measurement network of the University of Hamburg and on the other hand from COSMO [Consortium for Small-scale Modeling] simulations that are currently used for the weather forecast in Germany.

In the main part of this thesis some important input parameters of the APEX algorithm are tested and tuned for the existing conditions. Example output fields as well as the corresponding categorical verification scores are presented for the application to measurement data and observation data. On this basis the quality and the applicability of the APEX tool are discussed. Results show that with COSMO input data a higher lead time is possible with the same forecast accuracy than with PATTERN input data. The analysis of the convective evolution with the used data from the year 2012 yields that at the considered spatial and temporal scales only weak convective evolution arises. The deviations from APEX or rather the rain rates of the convective evolution within a range of +/- 1 mm/h exist in a fraction of approximately 80 – 90 %. The RMSE [root mean square error] shows that the COSMO simulated convective evolution is stronger than the measured one by trend. Moreover, weak signals of the BIAS point at balanced positive and negative deviations averaged over the whole field. Like in the RMSE score the overestimation of the convective evolution by COSMO is visible in the BIAS because the absolute values of the COSMO BIAS mostly are greater than those of the PATTERN BIAS.

In conclusion, a method for the filtering and investigation of the convective evolution of simulated precipitation fields was developed and tested leading to plausible results. However, it depends strongly on the particular event that is considered and it still contains some error sources. For the operational application further investigations would be necessary.

Kurzfassung

In dieser Masterarbeit wird im Kontext des Projekts HD(CP)² [High Definition Clouds and Precipitation for Climate Prediction] die lokalzeitliche Änderung simulierten Niederschlags anhand von Radardaten auf der LES-Skala [Large Eddy Simulation] untersucht und verifiziert. Die Besonderheit liegt darin, dass diese innere Entwicklung erst aus der totalzeitlichen Änderung des Niederschlags extrahiert werden muss. Dazu wird das Nowcasting-Tool APEX [Automated Precipitation Extrapolator] von Van Horne (2003) eingesetzt, das Regengebiete aus vorhandenen Daten erfasst, korreliert und in die Zukunft extrapoliert. Da der extrapolierte Niederschlag nur advektiver Art ist, lässt sich durch Subtraktion von den beobachteten oder simulierten Daten die lokalzeitliche Änderung ermitteln. Durch die separate Betrachtung von Beobachtungs- und Modelldaten kann mit Hilfe verschiedener Verifikationsindizes allein das Verhalten der inneren Entwicklung bewertet und verglichen werden, statt die Güte der Vorhersage zu berechnen. Die verwendeten Daten stammen zum einen aus dem PATTERN [Precipitation and Attenuation Estimates from a High Resolution Weather Radar Network] Messnetz des Meteorologischen Instituts [MI] der Universität Hamburg und zum anderen aus Simulationen durch COSMO [Consortium for Small-scale Modeling], dem aktuell vom Deutschen Wetterdienst [DWD] operationell laufenden Wettervorhersagemodell für Deutschland.

Im Hauptteil dieser Arbeit werden zunächst einige wichtige Eingabeparameter von APEX getestet und an die gegebene Situation angepasst. Exemplarische Ausgabefelder sowie die dazugehörigen kategorischen Verifikationsindizes werden sowohl für die Anwendung auf Messdaten als auch auf Modelldaten präsentiert. Auf dieser Basis wird außerdem auf die Güte und die Anwendbarkeit von APEX eingegangen. Die Frage, mit welcher der beiden Datengrundlagen mit gleicher Vorhersagegenauigkeit länger in die Zukunft extrapoliert werden kann, fällt zugunsten des Modells aus. Die Analyse der inneren Entwicklung mit den verwendeten Daten aus dem Jahr 2012 ergibt, dass sich auf den betrachteten Zeit- und Raumskalen kaum innere Entwicklung ausbildet. Die Abweichungen von der APEX Vorhersage bzw. die Niederschlagsraten der lokalzeitlichen Änderung liegen größtenteils innerhalb +/- 1 mm/h. Die Betrachtung des RMSE zeigt, dass tendenziell die durch COSMO simulierte innere Entwicklung stärker ausgeprägt ist als die gemessene – sowohl in positive als auch in negative Richtung. Schwache Signale im BIAS weisen außerdem darauf hin, dass positive und negative Entwicklungen sich über das gesamte Feld gemittelt meist ausgleichen. Die Überschätzung der inneren Entwicklung durch COSMO wird hier ebenfalls sichtbar, da die Absolutwerte des COSMO BIAS meist größer sind als die des PATTERN BIAS. Insgesamt wurde hier eine Methode zur Filterung und Untersuchung der lokalzeitlichen Änderung von Niederschlagsfeldern entwickelt und getestet, die durchaus zu plausiblen Ergebnissen führt, jedoch stark vom Einzelfall abhängt und noch einige Fehlerquellen enthält.

Contents

Abstract.....	ii
Kurzfassung	iii
Contents	iv
List of Tables	v
List of Figures.....	vi
1 Introduction.....	1
2 Methodology and data framework	4
2.1 Separation between advection and convective evolution.....	4
2.2 Overview of verification methods.....	8
2.3 The data framework	16
2.3.1 The precipitation network PATTERN.....	16
2.3.2 The model data from COSMO	18
2.4 Short overview of nowcasting algorithms.....	23
2.5 The Automated Precipitation Extrapolator (APEX).....	25
3 Adaptation of APEX	29
3.1 First APEX tests and modifications.....	29
3.2 Final APEX settings.....	39
4 Results and Discussion.....	41
4.1 APEX results and evaluation using categorical scores	41
4.1.1 APEX results from observation data.....	41
4.1.2 APEX results from model data	46
4.1.3 PATTERN versus COSMO – predictability with APEX	51
4.2 Analysis of the convective evolution using continuous scores	59
4.3 Error sources and uncertainties.....	68
5 Conclusion and Outlook	72
List of Abbreviations and Symbols.....	I
References.....	IV
Appendix.....	VIII
Acknowledgement	XII
Eidesstattliche Versicherung.....	XIII

List of Tables

Table 1.1: Listing and description of the Golden Day precipitation events	2
Table 2.1: Coordinates of the PATTERN radars.	17
Table 3.1: List of parameters for the APEX algorithm with nominal values	31
Table 3.2: CSI values for the correlation pair 2012/07/19 6:00 UTC / 6:04 UTC for different FILTER_ROWS and FILTER_COLS values.....	32
Table 3.3: CSI values for the correlation pair 2012/07/19 6:00 UTC / 6:04 UTC for different MAX_SHIFT and CORR_BOXSIZE values.....	33
Table 3.4: CSI values for the correlation pair 2012/07/19 6:00 UTC / 6:04 UTC for different RAIN_THRESH, SEARCH_RADIUS and SPEED_LIMIT values.....	34
Table 3.5: Improvement of the CSI values through the adjustment of the verification method from point to point matching (traditional method) to a neighborhood matching (fuzzy verification).	34
Table 3.6: CSI values for the APEX forecasts from the 19 th of July 2012 6:00 UTC - 7:00 UTC for different ANGLE_TOL values.	35
Table 3.7: List of adapted parameters of the APEX algorithm	40

List of Figures

Figure 2.1: Examples for a curvilinear grid	5
Figure 2.2: Flowchart of the methodology illustrating the way from the data files to the separation of advection and convective evolution and its evaluation.	7
Figure 2.3: Illustration of the idea how to separate advection and convective evolution with the APEX tool.....	8
Figure 2.4: Overview of verification techniques	10
Figure 2.5: Traditional verification vs. fuzzy verification.....	11
Figure 2.6: 2x2 table indicating the four possible categories of precipitation forecast evaluation ..	12
Figure 2.7: Equipment and Arrangement of the PATTERN network instruments.	17
Figure 2.8: Arrangement of the model variables in an Arakawa-C/Lorenz grid structure	20
Figure 2.9: COSMO model domain and PATTERN domain.....	21
Figure 2.10: Application of a radar mask	22
Figure 2.11: Forecast quality against lead time dependent on the forecasting method	24
Figure 2.12: Advection scheme used by the APEX nowcasting method.....	28
Figure 3.1: Visualizatin of the precipitation event ‘2012/07/19, 6 - 7 UTC’ with different ANGEL_TOL values.....	35
Figure 3.2: Averaged verification scores for PATTERN data on the one hand calculated in radar reflectivity Z , on the other hand calculated in rain rate R on ‘2012/07/28, 8 – 9 UTC’.....	36
Figure 3.3: APEX forecast for the 3 rd of August 2012 with COSMO data for different WX_MIN values.	37
Figure 3.4: Application of a pixel filter	38
Figure 4.1: APEX forecast with PATTERN data on ‘2012/07/28, 8 – 9 UTC’	42
Figure 4.2: Verification scores of the APEX forecasts of the 28 th of July 2012 (PATTERN data). ..	43
Figure 4.3: Averaged scores of the APEX forecast of the 28 th of July 2012 (PATTERN data).....	44
Figure 4.4: APEX forecast for the 3 rd of August 2012 with PATTERN data starting from 13:08 UTC illustrating an erroneous forecast.....	45
Figure 4.5: Verification scores of the APEX forecasts of the the 3 rd of August 2012 (PATTERN) .	45
Figure 4.6: Averaged scores of the APEX forecast on ‘2012/08/03, 15 – 16 UTC’(PATTERN).....	46
Figure 4.7: APEX forecast for the 19 th of July 2012 with COSMO data starting from 06:24 UTC .	47
Figure 4.8: Verification scores of the APEX forecasts of the 19 th of July 2012 (COSMO)	48
Figure 4.9: Averaged scores of the APEX forecast on ‘2012/07/19, 6 – 7 UTC’ (COSMO)	48

Figure 4.10: APEX forecast for the 3 rd of August 2012 with COSMO data starting from 14:28 UTC illustrating a result with low verification scores.	49
Figure 4.11: Verification scores of the APEX forecasts of the the 3 rd of August 2012 (COSMO) ...	50
Figure 4.12: Averaged scores of the APEX forecast on ‘2012/08/03, 14 – 15 UTC’ (COSMO).....	50
Figure 4.13: Comparison between PATTERN and COSMO CSIs on 2012/07/19.	51
Figure 4.14: Scatter plots of the PATTERN CSIs versus the COSMO CSIs for the Golden Days....	52
Figure 4.15: Scatter plots of the PATTERN FARs versus the COSMO FARs for the Golden Days .	53
Figure 4.16: Comparison of the measured or rather simulated precipitation fields of the PATTERN radar network and the COSMO simulation on ‘2012/07/19, 7 UTC’	54
Figure 4.17: Differences between mean COSMO and mean PATTERN CSIs of all the investigated data	55
Figure 4.18: Comparison of lead times after a decline on a factor of 1/e.	57
Figure 4.19: Mean precipitation coverage for COSMO and PATTERN as comparison.....	57
Figure 4.20: Illustration of a postive cell dynamic from the 3 rd of August 2012	61
Figure 4.21: Survey of rain rate differences (PATTERN) from the 3 rd of August 2012.	62
Figure 4.22: Convective evolution for the 3 rd of August 2012 between 13 and 14 UTC (PATTERN data) illustrated in pie charts	63
Figure 4.23: RMSE for every hour of the investigated data amount as comparison between the convective evolution of model simulated precipitation and the measured precipitation.	64
Figure 4.24: RMSE normed with the precipitation coverage for every hour of the investigated data amount as comparison between the convective evolution of model simulated precipitation and the measured precipitation.	66
Figure 4.25: BIAS for every hour of the investigated data amount as comparison between the convective evolution of model simulated precipitation and the measured precipitation..	67
Figure 4.26: Comparison of the RMSEs from the 28 th of July 2012 with original observation data and with filtered observation data.	69
Figure 4.27: Example of incorrect displacement from PATTERN observation data with a thin high intensity rainfall band at the 28 th of July 2012 between 7and 8 UTC.....	71

1 Introduction

The thermodynamic processes in the atmosphere, especially concerning clouds and precipitation are not yet completely investigated. The very high spatial and temporal variability of precipitation makes it difficult to prepare reliable predictions and severe weather warnings although there is already much effort in modeling this highly dynamical quantity.

However, precipitation predictions at short time scales are important in areas like aviation safety or flood forecasting as well as at longer time scales particularly in climate prediction and the change in precipitation patterns, frequencies or intensities.

To anticipate mitigating actions authorities are very interested in the quality and usefulness of forecasts because security arrangements are always associated with great expense. For this reason, the uncertainty of predictions must be quantified.

To improve the today's understanding in all these processes and their impact on climate prediction there is a BMBF [Bundesministerium für Bildung und Forschung] funded German-wide research initiative called "High Definition Clouds and Precipitation for Climate Prediction" [HD(CP)²]. Within this project the ICON model [Icosahedral non-hydrostatic], developed by the Max Planck Institute for Meteorology [MPI-M] and the German Weather Service [DWD], will be tuned to a spatial scale of 100 m to simulate clouds and precipitation over Northwest Europe with the aim to advance parameterizations of clouds and precipitation in climate models and to reduce the uncertainty in climate predictions. The high data density in Europe provides a good framework for the verification of the model simulations.

The aim of this work is to develop and to evaluate a method for the investigation and verification of precipitation at such high resolved spatial scales (LES scale [Large Eddy Simulation]) which are rarely considered up to now. Thereby the particular focus is on the separation between advection and the convective evolution of precipitation fields.

For that purpose the project "Precipitation and Attenuation Estimates from a High Resolution Weather Radar Network" [PATTERN] of the University of Hamburg provides reliable precipitation data in high temporal and spatial resolution. So it is possible to evaluate and compare model simulations with measurements.

The model data used in this thesis derive from the standard German weather prediction model named "Consortium for Small-scale Modeling" [COSMO]. Usually, its spatial resolution is 2.8 km. Beuchel (2015) nested down the model domain two times from 2.8 km to 1 km and

1 Introduction

again to 250 m. This is necessary to match the model grid size and the observational data grid size. Likewise the extent of the model domain is adapted to the PATTERN area. Four single convective precipitation events are chosen for the investigation which are classified already by Wünsch (2013) as so-called “Golden Days”. A Golden Day is defined as a precipitation event with measurement signals on all four countryside X-band radars of the PATTERN network during the summer 2012. Table 1.1 composes the Golden Days examined by Beuchel (2015). The verification done in this work is based on these precipitation events except for two hours: At the 7th of August 2012 the hour from 8 to 9 UTC is removed because the forecasts don't provide good results. Instead of that the hour from 16 to 17 UTC at the 3rd of August 2012 is added because in the COSMO data there is a strong cell development in this time.

In the recent years, several verification strategies were developed ranging from traditional verification statistics useful for macroscales to non-traditional verification strategies used for mesoscale problems. As the precipitation patterns here are considered at the very highly resolved LES scale another method is applied for the comparison between the model behavior

Table 1.1: Listing and description of the Golden Day precipitation events [Beuchel, 2015]

Precipitation event	Duration	Formation
2012/07/19	6:00 – 9:00 UTC	Positive vorticity advection and forced uplift
2012/07/28	6:00 – 9:00 UTC	Convergence of air masses at cold front and warm air uplift due to positive vorticity advection
2012/08/03	13:00 – 16:00 UTC	Large-scale surface heating leading to thermal low and thunderstorm development
2012/08/07	8:00 – 10:00 UTC	Showers triggered by dry adiabatic uplift and reaching of the equilibrium temperature.

and the observed data behavior. The precipitation nowcasting tool APEX [Automated Precipitation Extrapolator] provides an algorithm which calculates the advective displacement of a precipitation field half an hour in the future. The algorithm is in the context of this work is not primarily used for nowcasting but rather as an instrument for the separation between advective transport and convective evolution of the rain field. The focus lies on the investigation of the convective evolution or rather the question: Is the behavior of the convective evolution in the model and in the observations the same? To advance on this issue several work steps are necessary that are described in the main chapters of this thesis.

First of all, Chapter 2 gives an introduction to the method that is applied and used as basis for the investigation. Thereby, the already mentioned nowcasting tool APEX is described, a survey of different verification methods is given and the origin of the used data is explained. APEX is the most important instrument to answer of the question above. It needs to be tested and tuned elaborately because the results demand for a tool that fuctions as accurately as possible. Therefore, Chapter 3 describes in detail the parameters and setting options of APEX as well as some tests of it.

The main results are presented in Chapter 4 and are grouped into two parts.

The first part considers the outputs of APEX for the usage with COSMO data as well as with PATTERN data and compares them. On the one hand, radar forecast images are analyzed subjectively. On the other hand, categorical verification scores provide an objective analysis. With the help of these objective scores a mean forecast time with a certain forecast quality is calculated for the model data and for the observation data.

The second part analyzes the convective evolution that is obtained through the APEX tool with the assumption of perfect precipitation forecasts. Its behavior is expressed and evaluated with the help of quantifying verification scores that take into account the intensity of the convective evolution.

2 Methodology and data framework

The verification of precipitation on high spatial resolutions like the LES scale is not a trivial task. There is a variety of different verification methods that can be considered. Often they are specific for a certain spatial scale. In the literature some problems like the double penalty issue are discussed. Especially with increasing resolution of the spatial scale the verification gets more difficult because more and more small scale phenomena are resolved. Moreover, in this work the focus is on that part of precipitation that is caused by convective evolution. In order to get the information about the convective evolution a little trick is applied. A nowcasting tool called APEX is used to generate pure advective rainfall fields that can be used to get the convective evolution. The method is described in detail in section 2.1. Section 2.2 gives a survey of the commonly used verification techniques and some verification scores. The data framework, so the PATTERN network and COSMO are presented in section 2.3. The nowcasting algorithm APEX is introduced by a short overview of different nowcasting methods in section 2.4 and a description of its method in section 2.5.

2.1 Separation between advection and convective evolution

In the recent years, different verification techniques (section 2.2) reaching from global to mesoscale models were developed and applied. Until today, precipitation on the LES scale is almost not studied. Especially for the extraction of the convective evolution from the total precipitation a new method is tested in this work. The available PATTERN and COSMO data can be extrapolated in the near future with APEX separately. The result is an advective transported rainfall field for both data sets. The difference between the observed or modelled data at the according forecasted timestep and the advected fields by APEX provide the convective evolution of the rainfall field over the timestep. The error metrics that appear in both calculations (PATTERN, observational vs. COSMO, modelled) can be compared and consequently it is possible to answer some interesting questions. On the one hand, it allows to evaluate the quality of forecasts. Thereby, the interesting point is the comparison between the forecasts with modeled input data or with observed input data. For this, categorical scores are used that are already introduced in the work of Van Horne (2003) and summarized in section 2.2. They are adapted in a way that they function as fuzzy verification scores, so with a neighborhood (more details in section 2.2). On the other hand, the filtered fields of convective

evolution can be investigated and verified. Continuous variables help to quantify the convective evolution and to compare its behavior between the ‘model world’ and the ‘observation world’. The way from the existing data files to the results of this work is presented in detail in the following.

First of all, the different data sets of COSMO and PATTERN have to be adapted in a way that the entities and the spatial area are the same. As common unit the precipitation rate, or also called rain rate R in [mm/h] is chosen. However, the data exist only in reflectivity values z [mm⁶ m⁻³] or radar reflectivities Z [dBZ] (PATTERN) and total precipitation amounts in [kg/m²] (COSMO). Therefore, a conversion has to be done as described in sections 2.3.1 and 2.3.2. Moreover, only the part of the COSMO model domain that corresponds to the X-band radar measurement area from the PATTERN network is selected. Thereby a negligible error is accepted because the model grid is a curvilinear grid (Figure 2.1) but in the APEX nowcasting tool a cartesian grid is required. So, for each grid cell only an approximated longitude and latitude value is set. The grid resolution of 250 m in the PATTERN composite data is identical with that of the nested COSMO data. Furthermore, a common timestep must be determined. The PATTERN X-band radars provide data in a temporal resolution of 30 s whereas the COSMO model outputs are available in 1 min timesteps. The APEX algorithm in its original form (Van Horne, 2003) calculates with a forecast timestep of 15 min over 8 timesteps, so a total of two hours lead time. The determined timestep in this work should not be too short because of the much higher computing time with increasing temporal resolution. Otherwise, it should be shorter than the initially set 15 min because the considered spatial scale is higher resolved than intended by Van Horne (2003). Therefore, the timestep of the data and the forecast timestep in the APEX algorithm are adapted to 4 min. That leads to a total lead time of 32 min.

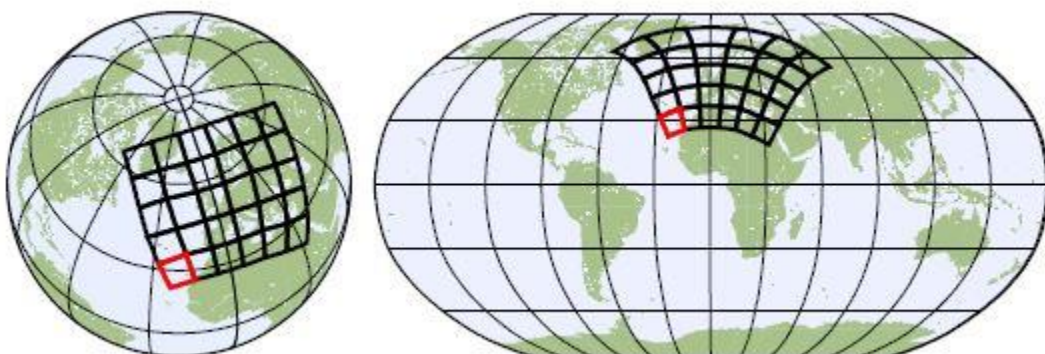


Figure 2.1: Examples for a curvilinear grid (Schulzweida, 2015).

2 Methodology and data framework

Figure 2.2 shows the structure of the methodology. Rectangular boxes represent data fields whereas the blue colored boxes mark the PATTERN fields and the red colored boxes mark the COSMO fields. The oval shaped yellow boxes are calculation procedures. All the above described adaptation steps are summarized in this figure by the first oval yellow box called ‘adaptation & preparation of the data for the APEX code’. The result is an input field that is easily readable for the APEX algorithm.

Based on this input field, the APEX nowcasting tool (second yellow box) is used to calculate eight forecast precipitation fields for each two consecutive input fields. Moreover, the actual weather files are stored. Each forecast field can be compared with the actual weather at the according time. So, the critical success index [CSI], false alarm ratio [FAR] and probability of detection [POD] are calculated to give an idea of the forecast quality. The principle functioning of this precipitation displacement with APEX is described in section 2.5. The specific modifications and settings are described in Chapter 3.

Further investigations of the APEX output fields consider the separation between the advection and the convective evolution of the precipitation field (third oval yellow box). The idea how to filter only that part of the field that is dynamically induced is simple: The APEX algorithm takes two input fields from the timesteps t_0 and $t_0 - 1$ and calculates the forecast fields from $t_0 + 1$ to $t_0 + 8$. Figure 2.3 shows schematically the different observation fields (blue) on a timeline from $t_0 - 1$ to $t_0 + 1$. The red colored box shows one of the the APEX forecast fields (fcst) which results from the observation fields ‘data(-1)’ and ‘data(0)’. From timestep to timestep the changes in the precipitation field consist of an advective part and the convective evolution. However, the APEX tool only perform an advective displacement of the field. Building the difference between the forecast field fcst(+1) and the observation field data(+1) at that time yields to the convective evolution of the rainfall patterns. This is done for every forecast timestep. Then different error metrics can be applied. In this case, the RMSE and BIAS are calculated to show the temporal behavior of the forecast error or rather the convective evolution.

In a final step, the calculated error metrics are used to find some characteristics in the PATTERN and COSMO calculations and to compare them. The evaluation answers the key questions of this work, e.g. if one of both, the observational data or the model data are more appropriate to be forecasted. Furthermore, the convective evolution is investigated more in detail. On the one hand, the categorical scores give answers about the spatial behavior of the convective development, on the other hand the continuous scores describe the intensification or attenuation of rainfall. With this method the COSMO simulated convective evolution can be verified.

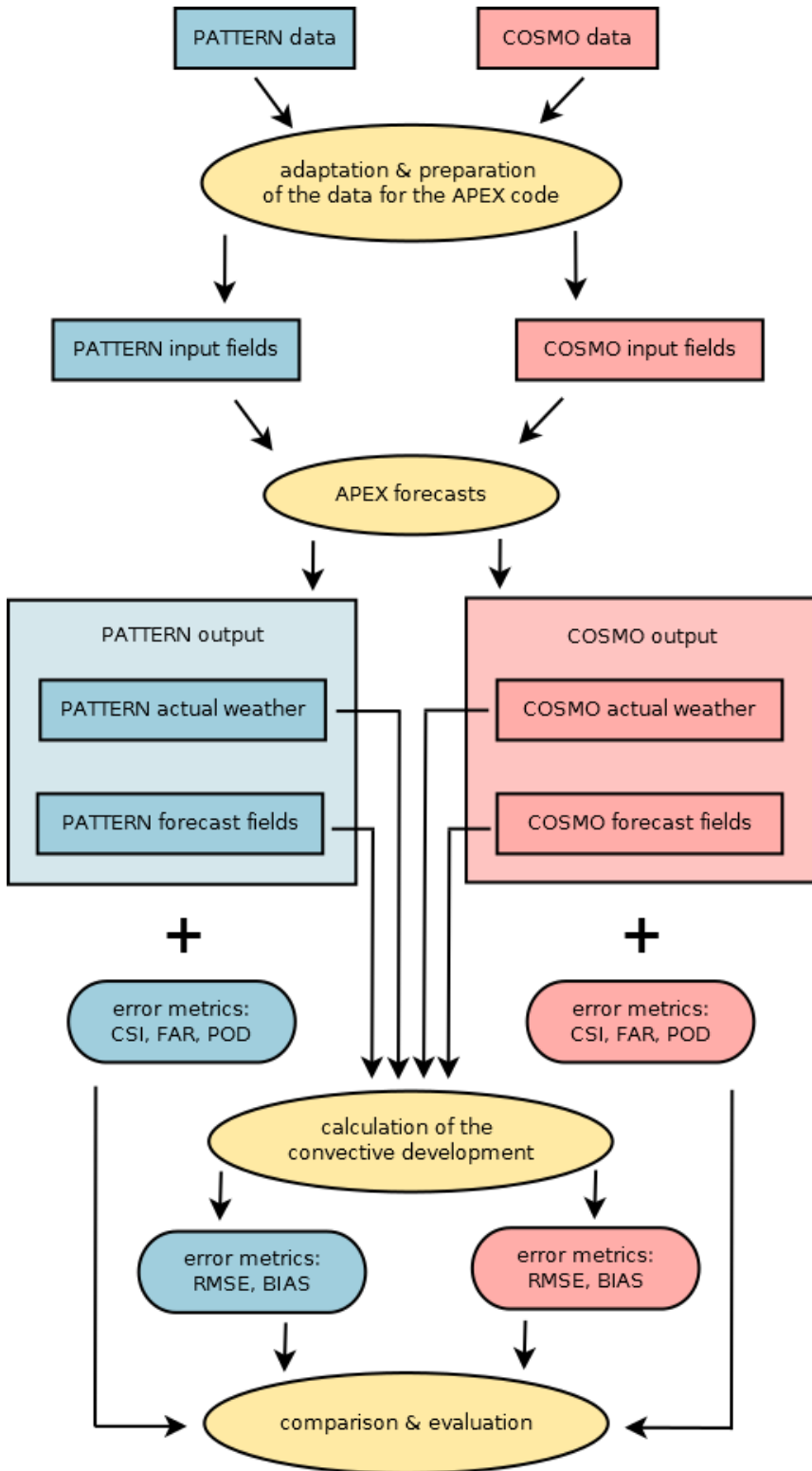


Figure 2.2: Flowchart of the methodology illustrating the way from the data files to the separation of advection and convective evolution and its evaluation. Rectangular boxes mark data fields whereas on the one hand there is a path for the PATTERN data (blue colored fields) and on the other hand for the COSMO data (red colored fields). The oval shaped yellow fields represent calculation procedures.

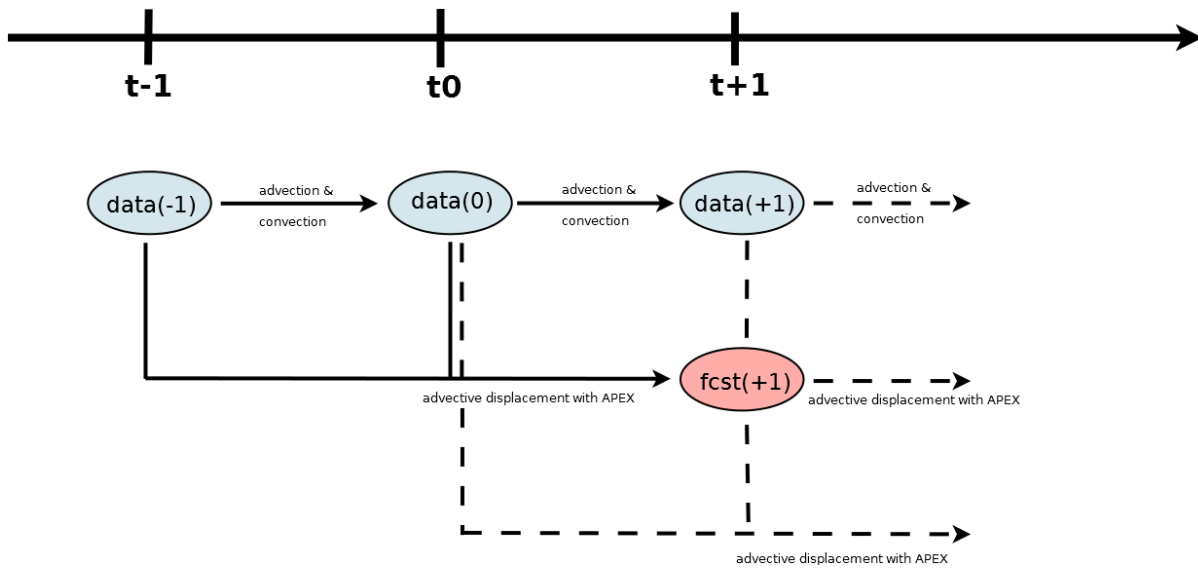


Figure 2.3: Illustration of the idea how to separate advection and convective evolution with the APEX tool on a timeline. The blue colored boxes represent the data fields (PATTERN or COSMO) and the red colored box represents the APEX forecast field (fcst) at the time $t_0 + 1$.

2.2 Overview of verification methods

To anticipate mitigating actions authorities are very interested in the quality and usefulness of forecasts because safety arrangements are always associated with great expense. For that reason, the uncertainty of predictions must be quantified. Until today, more effort has been invested in the development of forecasting techniques than in the study of verification methods. After Rossa et al. (2008) this is due to the increasing complexity of verification tasks with increasing resolution of precipitation forecasts. Traditional verification approaches of gridded forecasts were developed on low resolution NWP [numerical weather prediction] models for global simulations. Higher resolution mesoscale models have to deal with shorter time scales and shorter accumulation periods. At these scales, the traditional verification methods are not sufficient because phenomena like frontal passages are relevant. The timing and the location of such phenomena is important but it is difficult to match precisely observed small scale features. Already small errors may result in the so-called ‘double penalty’. It means that the error of a forecasted event is weighted twice, on the one hand it is ‘observed

but not forecasted' on the other hand it is 'forecasted but not observed'. Then the small scale errors can dominate the total error even if the large scale weather seems to be realistic and predicted well (Ebert, 2008).

Traditional verification strategies match the observed value with the forecast value in the same grid box. Then they compute various metrics on the matched set of all forecasts and observations. In other words, only forecasts corresponding to that grid box in space and time are verified against that observation.

In contrast, the non-traditional verification strategies relax the point-to-point verification and look rather at the main characteristics of fields. These techniques represent the skill of a mesoscale forecast much better and do not require the forecast to match exactly the observation at fine scales. They can be divided into two classes: the object-oriented techniques and the scale-dependent techniques such as 'fuzzy' verification technique and the spatial decomposition method (Figure 2.4).

The object-oriented techniques are pattern recognition methodologies which are quite intuitive and effective. After Ebert (2008) they try to imitate the viewpoint of a human analyst, when presented with a rainfall map. Like the name suggest, they identify weather features or 'objects' in the forecast and observation fields and compare their properties. Examples for object-oriented verification techniques can be found in Ebert and McBride (2000), Davis et al. (2006) or Marzban and Sandgathe (2006).

The fuzzy verification methods (also called neighborhood methods) require that the forecasts are in approximate agreement with observations, so they must be close in space, time or intensity. An object matching is not required anymore so that this method can be applied just as well to amorphous fields. Slight displacements of the forecasts are acceptable whereas the closeness requirements are varied over space and/or time. Therefore, the fuzzy verification technique belongs to the scale-dependent techniques (Figure 2.4). It looks for agreements in a spatial (or sometimes additionally temporal) neighborhood of the point of interest in the forecast field (Figure 2.5). Some methods even consider the neighborhood in the observation field. The development of the fuzzy verification techniques was advanced by several scientists quite independently. Some important works are e.g. Brooks et al. (1998), Zepeda-Arce et al. (2000), Casati et al. (2004), Germann and Zawadzki (2004), Roberts and Lean (2008) or Segawa and Honda (2007).

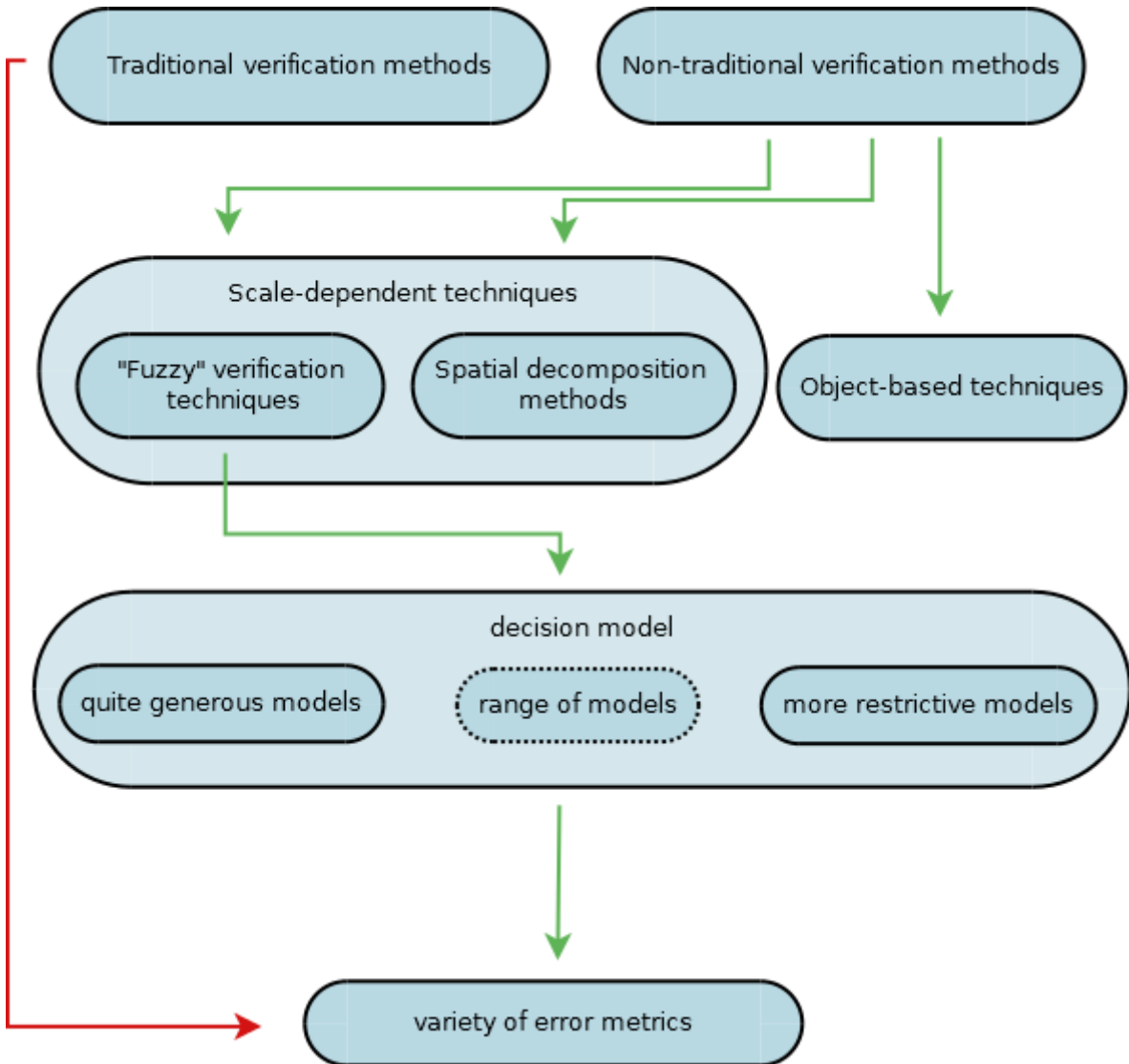


Figure 2.4: Overview of verification techniques: traditional verification methods only do a point to point matching and therefore don't need any decision model (red arrow). Non-traditional verification methods can be divided into “fuzzy” verification, spatial decomposition and object-based techniques (green arrows). The “fuzzy” verification method requires for a decision model for what is a good forecast or not. Finally, a variety of error metrics can be applied.

Multidimensional windows allow the user to investigate closeness in space, time, intensity or others simultaneously. The main differences between the fuzzy techniques are in the choice of the decision models which gives the answer to what is a good forecast. It can be more generous, e.g. a forecast is good if at least one observed event and at least one forecast event are found within the same neighborhood, or more restrictive, e.g. the frequency of events in forecast and observation within the same neighborhood has to be similar. In between there is a range of user defined possibilities of decision models. Finally, a variety of error metrics for

deterministic and probabilistic forecasts can be applied to indicate the quality of the forecast. Deterministic quantitative precipitation forecasts [QPF] can be evaluated either as categorical event or as continuous variable and accordingly the error metrics differ. The categorical approach is more common and easy to apply. It doesn't consider the intensity of rainfall fields but only decides between event and non-event dependent of a threshold between 0.1 mm and 0.3 mm (Rossa et al., 2008). This threshold differs from country to country and means an accumulated precipitation during a 24-hour or 12-hour time period, mostly. The choice of this threshold has a noticeable impact on the verification results. The categorical approach allows four possibilities of decision or in other words it defines a 2x2 contingency table: hits (a), false alarms (b), misses (c) and correct rejections (d) (Figure 2.6).

For binary events (yes/no), an event (yes) is defined by a value greater than or equal to the specified threshold. Otherwise, it is a non-event ('no'). The elements of the table count the number of times each forecast and observed yes/no combination occur in the verification dataset. Many categorical verification scores can be computed from these four values.

In the following, the mainly used scores of traditional verification are presented. If not marked otherwise, the information is from Ebert (2008) or Rossa et al. (2008).

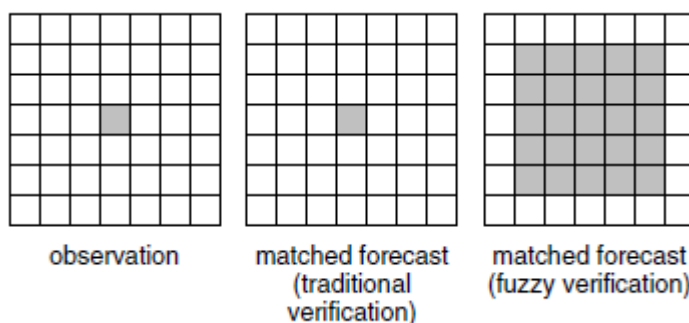


Figure 2.5: For the observation in the domain at left, the traditional verification matches the same grid box in the forecast (center), whereas fuzzy verification considers a neighborhood surrounding the observations (right). (Ebert, 2008)

Event forecast	Event observed		
	Yes	No	Marginal total
Yes	a = hit	b = false alarm	a + b
No	c = miss	d = correct no	c + d
Marginal total	a + c	b + d	a + b + c + d = N

Figure 2.6: 2x2 table indicating the four possible categories of precipitation forecast evaluation [1].

The mean error (ME), also called BIAS, is simply the arithmetic average of the difference between forecasts and observations.

$$ME = BIAS = \frac{1}{N} \sum_{i=1}^N (Y_i - X_i) \quad (2.1)$$

Y_i is the forecast value, X_i is the corresponding observed value, and N is the number of forecast-observation pairs. It is the counterpart to the frequency bias (FBI) in case of categorical QPF.

The mean square error (MSE) measures the average squared error magnitude, and is often used in the construction of skill scores (SS) that measure the fractional improvement of the forecast compared to a reference forecast like the persistence.

$$MSE = \frac{1}{N} \sum_{i=1}^N (Y_i - X_i)^2 \quad (2.2)$$

The root mean square error (RMSE) measures the average error magnitude, giving greater weight to the larger errors.

$$RMSE = \sqrt{\frac{1}{N} \sum_{i=1}^N (Y_i - X_i)^2} \quad (2.3)$$

Due to the second power the MSE and RMSE are much more sensitive to larger errors than the ME. ME, MSE and RMSE all are counted among the verification methods for continuous QPFs. In contrast to the categorical approach they give additional information about the magnitude of the deviation from the corresponding observation.

The frequency bias is the ratio of the forecast frequency to the frequency of observed occurrences. It ranges from zero to infinity and its optimal value is one. The forecast is unbiased when the number of forecasts is exactly the number of observed events. In case of a small number of observed occurrences, the denominator becomes small and consequently the FBI large and unstable. The event is overforecasted when the FBI is greater than one and underforecasted when it is less than one [2].

$$FBI = \frac{\text{hits} + \text{false alarms}}{\text{hits} + \text{misses}} = \frac{\text{total forecast yes}}{\text{total observed yes}} \quad (2.4)$$

The FBI and all the following binary scores only measure categorical events, so they do not provide information on the magnitude of forecast errors.

The probability of detection (POD), also known as hit rate H, measures the fraction of observed events that were correctly forecasted. It ranges from zero to one whereas a perfect score is one.

$$POD = H = \frac{\text{hits}}{\text{hits} + \text{misses}} = \frac{\text{number of events correctly forecasted}}{\text{total number of events observed}} \quad (2.5)$$

The false alarm ratio (FAR) gives the fraction of forecast events that were observed to be non-events. It ranges from zero to one whereas a perfect score is zero.

$$FAR = \frac{\text{false alarms}}{\text{hits} + \text{false alarms}} \quad (2.6)$$

The POD and FAR always has to be considered together. The POD is only sensitive to missed events rather than false alarms. So, it is possible to influence and improve the POD artificially by forecasting the event more often, which lead to fewer misses but simultaneously to more false alarms and an overforecasted FBI [3]. The FAR is only sensitive to false alarms rather than misses. It can be controlled artificially by deliberately underforecasting the event. But this leads simultaneously to a higher number of misses, and as consequence the POD is influenced negatively [4].

The false alarm rate F provides the probability of false detections. It measures the fraction of observed non-events that were forecasted to be events.

$$F = \frac{\text{false alarms}}{\text{correct rejections} + \text{false alarms}} \quad (2.7)$$

The threat score (TS), also called critical success index (CSI), gives the fraction of all events that were correctly diagnosed. It is a commonly used score especially for rare events which ranges from zero to one with a perfect value of one. It takes into account both, misses and false alarms but it ignores correct rejections. Therefore, it is a more balanced score than the POD or FAR.

$$CSI = TS = \frac{\text{hits}}{\text{hits} + \text{misses} + \text{false alarms}} \quad (2.8)$$

The CSI tends to give poorer scores for rare events. To tackle this tendency the equitable threat score (ETS) which similar to the TS is designed. It accounts for the hits that would occur purely due to random chance.

$$ETS = \frac{\text{hits} - \text{hits}_{\text{random}}}{\text{hits} + \text{misses} + \text{false alarms} - \text{hits}_{\text{random}}} \quad (2.9)$$

where

$$\text{hits}_{\text{random}} = \frac{1}{N} (\text{observed yes} \times \text{forecast yes}) \quad (2.10)$$

Furthermore, some probabilistic verification scores like the Brier score (BS), the Brier skill score (BSS) or the rank probability score (RPS) can be defined to compare the forecast probability of an event to the observed occurrence. These scores are only to be mentioned in this context but not described in detail because this work only considers deterministic QPFs. More detailed information about the traditional precipitation verification methods can be found in different text books and articles such as Wilks (2006), Jolliffe and Stephenson (2003) or Nurmi (2003).

After Rossa et al. (2008), categorical scores provide a more meaningful information of the quality of forecasts than continuous variables because precipitation is a not normally distributed quantity. Deviations of the forecasted precipitation field in the rainfall intensity can lead to large errors. Especially those scores using squared errors are very sensitive.

Another type of scale-dependent verification is called ‘spatial decomposition method’. A spatial filter separates the forecast and observation fields into different spatial scales. For each scale, the errors are computed separately and summed up to the total error (Rossa et al., 2008). Afterwards, continuous, categorical or probabilistic verification metrics may be applied for quantification. This method allows to link the errors to according phenomena.

On the one hand, the diversity of verification approaches reflects the efforts of the recent years concerning the significance of forecast quality measures. On the other hand, this diversity holds the risk that the comparison of verification results becomes more and more complex. Therefore, some organizations like i.e. the ECMWF [European Centre for Medium-Range Weather Forecasts], published a list of recommendations for their member states to harmonize verification results (Rossa et al., 2008). The choice of the correct verification method is strongly dependent on the purpose (e.g. hydrological applications or model development) and the available verification data. Users who only have access to rain gauge data are more limited in the choice of verification techniques than those who also have radar data. When using high resolution data, the double penalty problem may lead to poorer verification results. For verifying gridded data from radars, the evaluation tool has to be more diagnostic and spatial verification methods are more useful (Rossa et al., 2008). For NWP forecasts the upscaling method, one of the neighborhood verification methods, is appropriate to satisfy the requirements of hydrologists or model developers who are interested in rainfall amounts or water balances.

2.3 The data framework

Verification of precipitation or other quantities means that model simulated meteorological data have to be compared to a reference, the observational data. For both of these pillars the data sources used for the verification of precipitation on the LES scale are presented in this chapter. Thus, section 2.3.1 describes the background of the observations and section 2.3.2 gives an overview of the derivation of the modeled data.

2.3.1 The precipitation network PATTERN

The Precipitation and Attenuation Estimates from a High Resolution Weather Radar Network [PATTERN] provide a suitable data source which allows to compare highly resolved observation data with high resolved model data. The project is a collaboration between the Max Planck Institute Hamburg [MPI] and the University of Hamburg [5] and funded by the German Science Foundation [DFG] (Lengfeld et al., 2012). It consists of five low-cost high resolution X-band rain radars of which one covers the urban area of Hamburg [HHG] and four are located in the northwest countryside of Hamburg in a way that there is an overlapping of these four radars (Figure 2.7). The exact locations are Bekmünde [BKM], Hungriger Wolf [HWT], Moordorf [MOD] and Quarnstedt [QNS]. Table 2.1 gives an overview of the exact locations of the PATTERN radars. The arrangement is ordered purposely to investigate and correct attenuation errors in the measurements and to improve the accuracy of rain rate measurements (Feiertag et al., 2011). The first of these High Resolution Weather Radars [HRWR] are in operation since winter 2011. They provide data with 60 m range, 1° azimuthal and 30 seconds temporal resolution, respectively. The elevation is fixed. Compared to conventional C-band radars which are in operational use by the DWD for example, their advantages are the much more compact construction, the much lower costs and the higher resolution. On the other hand, their maximum measurement distance is very limited so that the application is restricted to small areas of interest.

Furthermore, four micro rain radars [MRRs], four rain stations consisting of MMR, rain gauge [RG] and anemometer and five stations for observing surface fluxes, turbulence and radiation budget are installed. All these measurements are expected to record a long term precipitation data set for both, research applications and operational use in flash flood warning systems. However, for the investigation in this thesis only the X-band radar data are used.

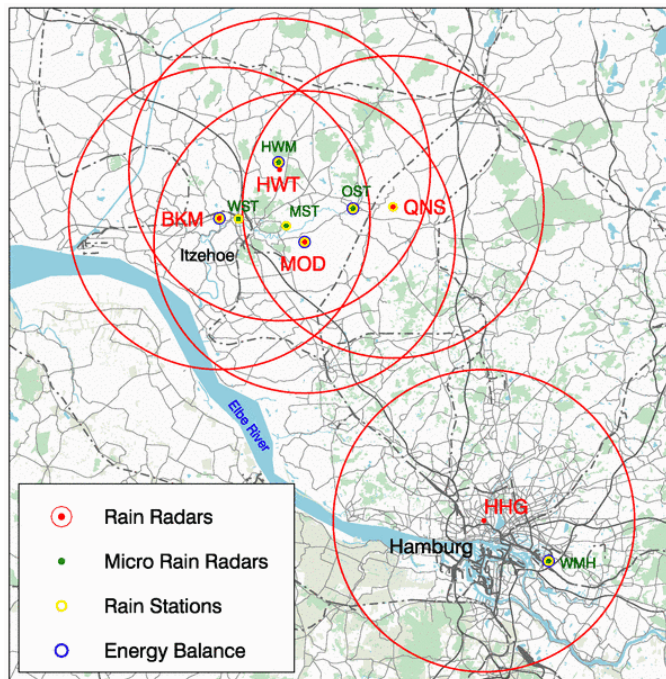


Figure 2.7: Equipment and Arrangement of the PATTERN network instruments in the metropolitan area of Hamburg.

Table 2.1: Coordinates of the PATTERN radars.

Radar	Latitude	Longitude
HWT	53.9889°N	9.5688°E
MOD	53.9024°N	9.6183°E
QNS	53.9431°N	9.7984°E
BKM	53.9314°N	9.4459°E

In recent years, first studies already engaged in the project. For example Lengfeld et al. (2012) utilized the advantage of the overlapping to calculate and correct the attenuation and to remove clutter, spikes and noise. Thanks to this work, further studies are enabled. Also the APEX algorithm described in section 2.4 requires for these processed data. Ongoing topics and measurements can be seen on the PATTERN homepage [5] or at facebook.com/wetternetzuhh.

If not marked otherwise, the information about the PATTERN network is taken from the PATTERN homepage which is linked under the reference [5].

The PATTERN data are available as composite of the corrected radar reflectivity. Because the X-band radars measure the energy intensity which is backscattered from rain droplets as a reflectivity value z in [$\text{mm}^6 \text{ m}^{-3}$] or the more commonly used radar reflectivity Z in [dBZ] which calculates as

$$Z = 10 \cdot \log(z) \quad (2.11)$$

the units have to be adapted to get a more demonstrative quantity and make the data comparable with the COSMO data. As common unit the rain rate R in [mm/h] is chosen. For the conversion from Z to R the so-called Z - R -relationship is applied. The DWD and the PATTERN workgroup use the following relationship to derive the precipitation intensity R (Beuchel, 2015):

$$z = a \cdot R^b \begin{cases} Z \leq 36.5 \text{ dBZ}: & a = 320, b = 1.4 \\ 36.5 \text{ dBZ} < Z \leq 44.0 \text{ dBZ}: & a = 200, b = 1.6 \\ Z > 44.0 \text{ dBZ}: & a = 77, b = 1.9 \end{cases} \quad (2.12)$$

Z denotes the radar reflectivity, z the non-logarithmic value of Z , a and b are specific parameters for different radar reflectivity values.

The processing steps that happen from the raw data to the processed data that are used here can be referred in Lengfeld et al. (2013) and Lengfeld et al. (2014).

2.3.2 The model data from COSMO

The “Consortium for Small-scale Modeling” [COSMO] model is the standard German numerical weather prediction [NWP] model in operating state. It is a nonhydrostatic limited-area atmospheric prediction model (Schättler et al., 2013) based on the primitive thermo-hydrodynamical equations for compressible flows in the moist atmosphere without any scale approximations. The German Meteorological Service [Deutscher Wetterdienst, DWD] uses it operationally since 1999 as a fusion of the formerly known “Lokalmodell” [LM] and the

triangular mesh global gridpoint model GME. After Schättler et al., COSMO is designed not only for the operational weather prediction but also for scientific research applications on the meso- β and meso- γ scale or for case studies. The grid used in this model is orientated on rotated geographical coordinates and a generalized terrain following height coordinate. Like in nearly every more complex model, some physical processes are parameterized also in the COSMO model. To run it, further steps like data assimilation, interpolation of boundary conditions from a driving model and postprocessing utilities are required (Schättler et al., 2013).

Before the development of the COSMO-model, many NWP-models operated with a grid resolution of 10 km or even lower. The aims of the new model with a resolution from 1 to 3 km over large domains were to resolve deep moist convection and the associated feedback mechanisms to larger scale phenomena. That makes it possible to capture small-scale severe weather events. The expectations are to simulate i.e. supercell thunderstorms, intense mesoscale convective complexes, prefrontal squall-line storms and others.

Concerning the scientific and technical purposes, examples like large-eddy simulations, studies on orographic systems and storm dynamics, development and validation of large-scale parameterizations schemes by fine-scale modeling, and test of computational strategies and numerical techniques can be mentioned.

For all these different applications, a number of communities adapted the model for example in climate mode [CCLM] or the online coupled module for aerosols and reactive trace gases [ART].

The variables of the COSMO-model are formulated on an Arakawa-C grid structure and a Lorenz vertical grid staggering (Schättler et al., 2013; Baldauf et al., 2011). Figure 2.8 illustrates the arrangement of the model variables in such a grid structure. Its coordinates are defined by $(\zeta, \lambda, \varphi)$. After discretization these coordinates are represented by a finite number of grid points (i, j, k) , where i corresponds to the λ -direction, j to the φ -direction and k to the ζ -direction. The horizontal velocity components u and v are set in the center of the grid box sides whereas u is located on the northern and southern borders and v on the western and eastern borders. The vertical wind component w is located at the top and bottom layer of the grid box side. All scalar variables are located in the center of the grid box.

The model equations are solved numerically by the traditional finite difference method. That means, spatial differential operators are replaced by finite difference operators. The time

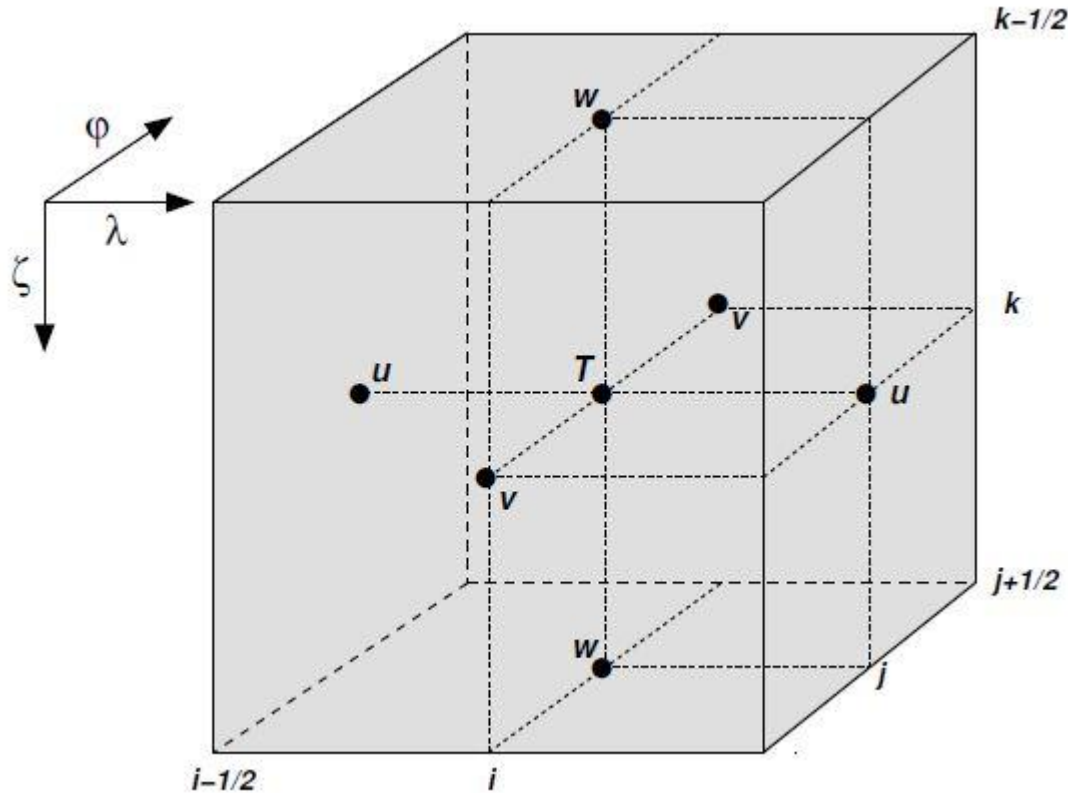


Figure 2.8: Arrangement of the model variables in an Arakawa-C/Lorenz grid structure. The grid box volume is $\Delta V = \Delta\zeta\Delta\lambda\Delta\gamma$ [Schättler et al., 2013; Baldauf et al., 2011].

discretization uses a fixed time step Δt as well. A detailed list of the model dynamics, the numerical settings, the initial and boundary conditions and the physical parameterizations can be found in Schättler et al. (2013).

The COSMO-model provides in addition to the observational data from the PATTERN network the model data for the verification task in this work. Its spatial resolution of ~ 2.8 km was nested down by Beuchel (2015) two times from 2.8 km to 1 km and again to 250 m to ensure that the model grid size and the observational data grid size fit together. Also the simulation area with an expanse of 150.25 km \times 112.75 km, going from 53.223 – 54.241°N and 8.426 – 10.734°E (Beuchel, 2015) is adapted to the PATTERN area (Figure 2.9).

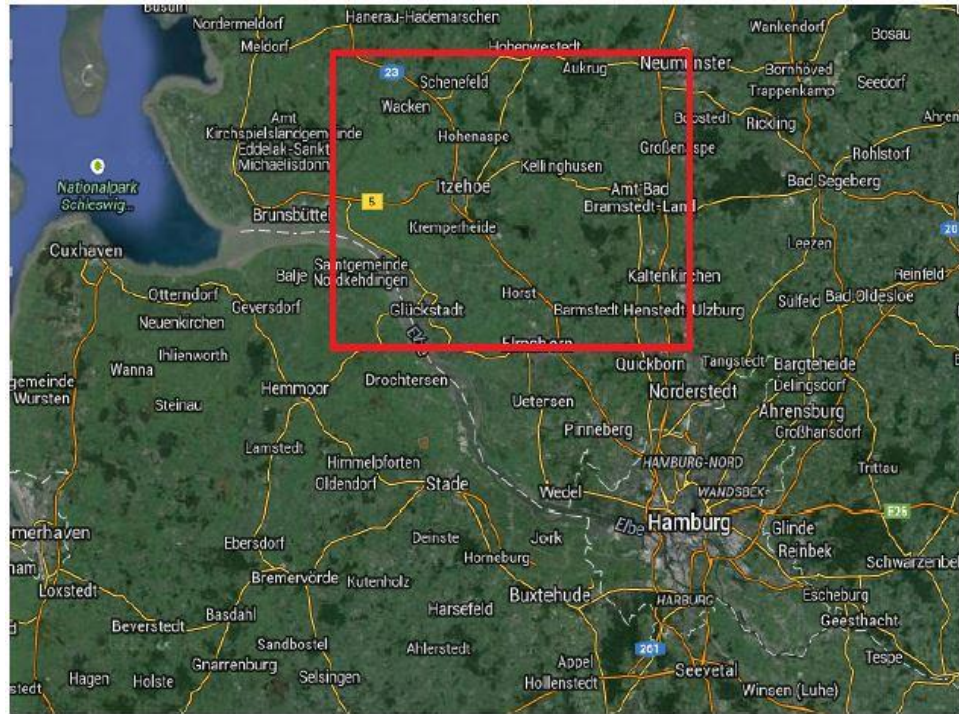


Figure 2.9: The map section shows the COSMO model domain. The PATTERN domain is marked by the red rectangular (Beuchel, 2015).

Amongst others, the output variables of the COSMO model are the wind components u , v and w , air temperature, air pressure, specific cloud ice content, specific humidity, specific snow content, surface snow amount, snow surface temperature, freshness of snow, density of snow, specific cloud liquid water content, specific rain content and specific graupel content (Beuchel, 2015). For the purpose of this thesis only the total precipitation amount [kg/m^2] is relevant. To make the data comparable with the PATTERN data it is required to have consistent entities. The most intuitive entity for the reader when viewing a radar image is the rain rate R [mm/h]. Since, the COSMO output files are available in one minute time steps, the total precipitation amount has to be multiplied by 60 to get the value in [mm/h]:

$$\left[\frac{\text{kg}}{\text{m}^2 \text{min}} \right] = \left[\frac{\text{mm}}{\text{min}} \right] = \frac{1}{60} \left[\frac{\text{mm}}{\text{h}} \right] \quad (2.13)$$

Furthermore, a radar mask is set over the output images of the COSMO data. After that, only the parts of the image are visible which are covered by the PATTERN radars. So, it is ensured that the verification area is the same in the PATTERN data and the COSMO data. Figure 2.10

2 Methodology and data framework

presents an example from the 28th of July 2012 at 8 UTC. COSMO simulated a precipitation field covering about half of the image and ranging from the northern border to the southern border (Figure 2.10 (b)). Figure 2.10 (a) shows the radar mask where the red colored region is the area that is covered by the PATTERN X-band radars. The gaps on the southeast-side of the image result from steady obstacles like buildings that restrict the radar sight distance. Figure 2.10 (c) shows the precipitation field of (b) after applying the radar mask (a).

The scales of the precipitation fields in rain rates [mm/h] are logarithmic. The advantage is that the lower precipitation amounts are visible much better. Otherwise, large parts of the image would be lost or only hardly visible because precipitation is a not normally distributed quantity.

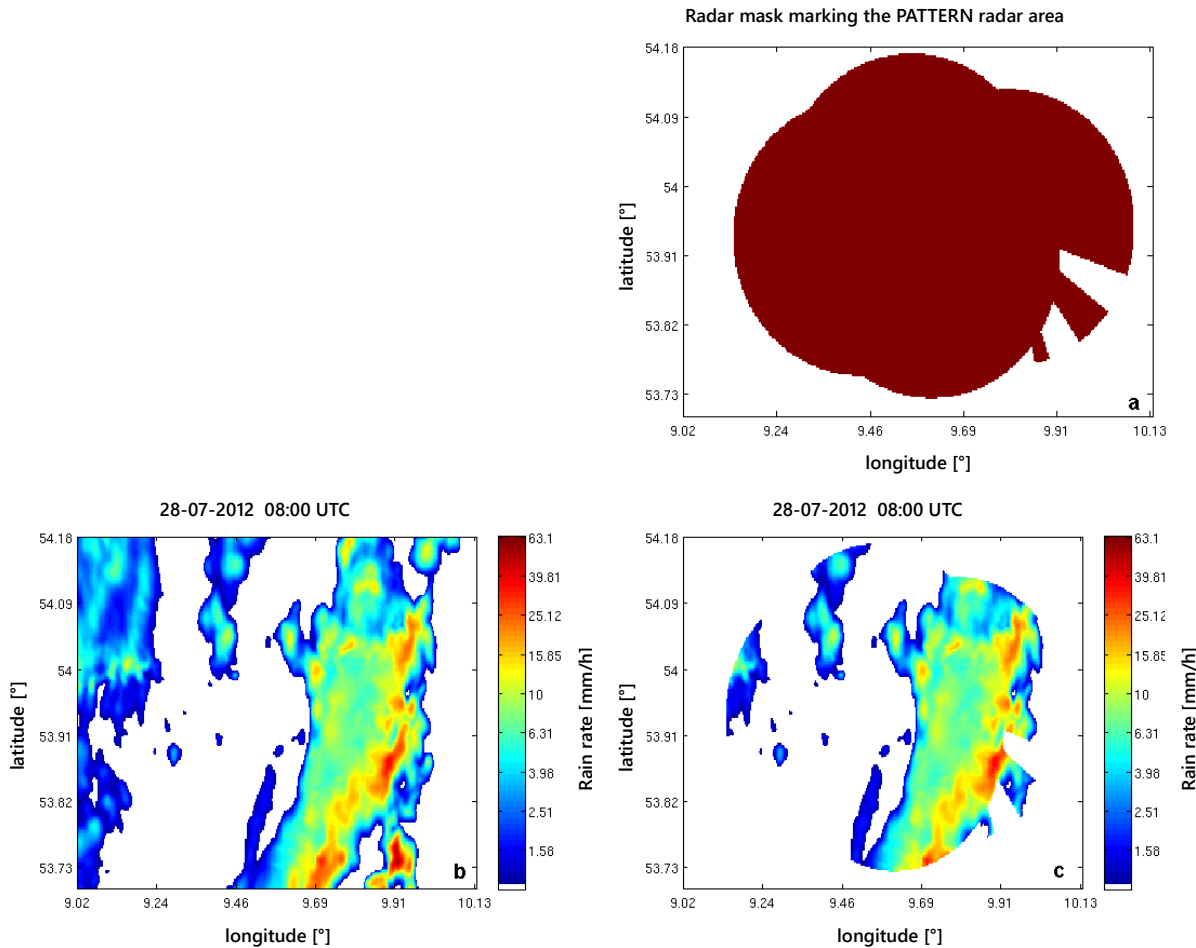


Figure 2.10: The radar mask (a) shows the red colored region that is covered by the PATTERN X-band radars. It is applied to the precipitation field (b) simulated by the COSMO model and nested down by Beuchel (2015). The remaining precipitation field is shown in (c).

Four single convective precipitation events are chosen for the investigation by Beuchel (2015) which are classified already in 2013 by Wünsch (2013) as so-called “Golden Days”. A Golden Day is defined by Wünsch (2013) as a precipitation event with measurement signals on all four countryside X-band radars of the PATTERN network during the summer 2012. Table 1.1 composes the Golden Days examined by Beuchel (2015). The verification done in this work is based on these precipitation events.

2.4 Short overview of nowcasting algorithms

For today’s weather forecast numerical weather prediction [NWP] models are indispensable. The increasing computing power and linked to that the increasing grid resolution of the models improved the weather forecast over the last decades enormously. Nevertheless, the meteorologist still has an important function when a precise prediction for the publicity has to be done, especially in case of severe weather warnings. Weather experts have to decide if they trust a model output or if they have to correct it. Particularly in the area of nowcasting humans still give a better quality prediction than computers and NWP models. Nowcasting means a weather prediction with lead times up to 6 hours or sometimes up to 12 hours, depending on the definition. In Figure 2.11 the quality of forecasts by the different forecast methods against the forecast lead time is presented. Reasons for the very limited forecast quality of NWP models in the first 6 hours are e.g. that the model formulations and grid lengths doesn’t resolve relevant physical or dynamical processes accurately or that the atmospheric system responds in a non-linear way to small perturbations for such short forecast lead times (Pierce et al., 2012). However, precise forecasts at short temporal scales and high spatial resolutions are important in many applications like aviation, flash flood warnings and others. Therefore, in the recent years many nowcasting techniques were developed. Concentrating on the precipitation nowcasting, this can be done by eye using satellite or radar observation data or with automated nowcasting tools which extrapolate the observed data in the near future of several hours.

Part of this work was to find a suitable tracking and extrapolation method which uses the existing radar data from the PATTERN network and calculates a short term precipitation nowcast. The different techniques can be divided into cell tracking and area tracking algorithms for the usage in convective precipitation situations or in stratiform precipitation situations, respectively. Only few methods can handle both. Besides, there were developed

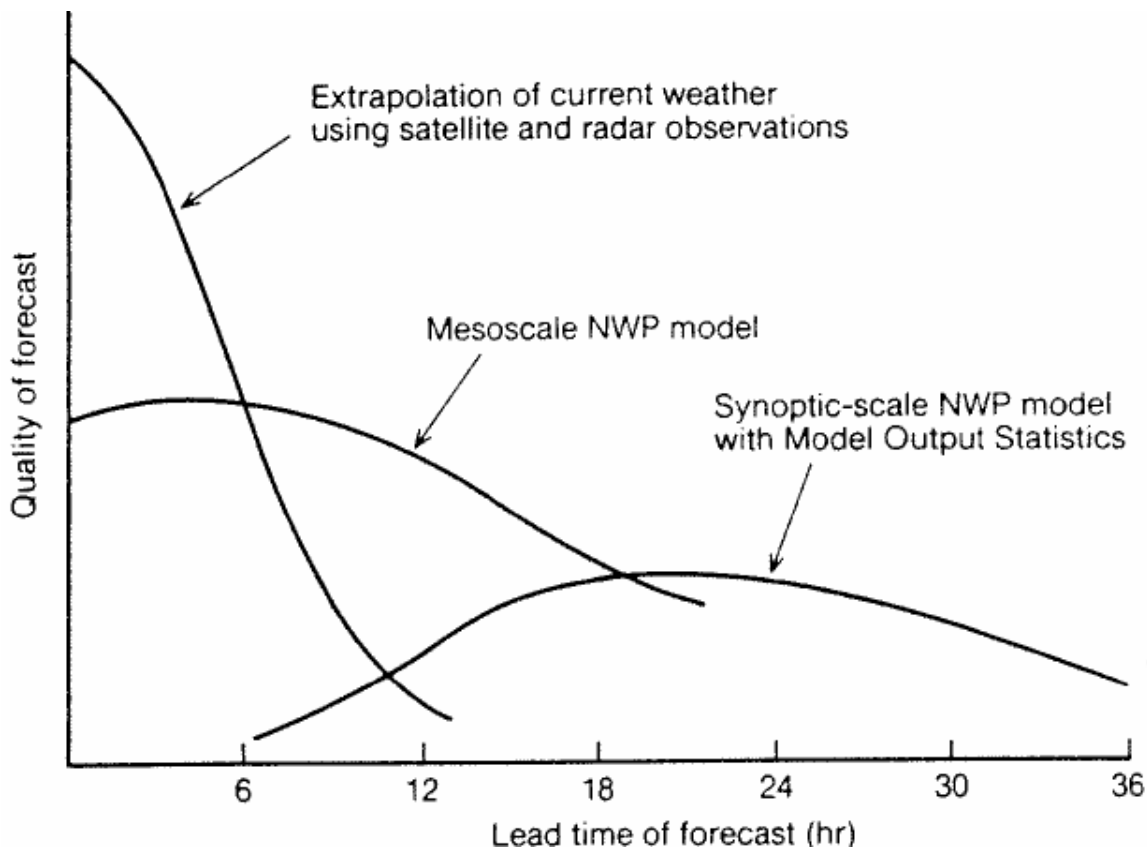


Figure 2.11: Schematic visualization of the forecast quality against the forecast lead time dependent on the forecasting methodology. [Pierce et al., 2012]

some stochastic methods which represent the atmospheric evolution by statistical models and some multimodal methods which combine radar data with other meteorological data or NWP model outputs. Further information and examples for the different methods can be looked up in a schematic overview from Ruzunski (2010).

For the daily weather forecast and the typical rainfall patterns and amounts in our central Europe position, a common used method is the COTREC algorithm (Li et al., 1995) which is a continuity of the TREC algorithm (Rinehart and Garvey, 1978). These two methods are based on calculating cross-correlations between subgrids in successive radar images. A few years later, the ‘Growth and Decay Storm Tracker’ [GDST] was developed by Wolfson et al. (1999). It is also based on the TREC method but an image pre-filtering is included. Van Horne (2003) investigates and compares in his work the GDST with the Automated Precipitation Extrapolator [APEX] and provides its algorithm as a free source code. APEX combines concepts of different previous developed algorithms and uses amongst others the cross-correlation method of TREC to generate the velocity field for the displacement of rainfall pixels. In some test storm events, APEX shows good results. Particular, at short lead times it scores higher than the GDST (Van Horne, 2003). In this thesis, the APEX tool is used as an

instrument for the separation between advection and convective evolution and is therefore described more detailed in Chapter 2.5.

2.5 The Automated Precipitation Extrapolator (APEX)

The Automated Precipitation Extrapolator [APEX] presented here is one of the nowcasting methods described in the previous section. It was developed by M. P. Van Horne at the Massachusetts Institute of Technology in 2003 and uses radar rainfall fields as input to calculate very short-term precipitation nowcasts both for stratiform and convective precipitation fields. According to Van Horne (2003) its method is based on a correlation analysis between two consecutive radar images combined with spatial filtering to produce a gridded velocity field for the advection of rainfall fields. The theoretical base is a steady state assumption which means that the precipitation intensities and spatial patterns stay constant over short timesteps. The forecasted rainfall rate at the point (x_F, y_F) is presented by Van Horne in a simplified way by

$$\Psi_F(t_0 + \tau, x_F, y_F) = \Psi_I(t_I, x_I, y_I) \quad (2.14)$$

$$x_F = x_I + \tau * u(x_I, y_I) \quad (2.15)$$

$$y_F = y_I + \tau * v(x_I, y_I) \quad (2.16)$$

where Ψ_F is the forecasted rainfall field, Ψ_I the initial rainfall field, (x_I, y_I) the location of the considered pixel in the initial field, (x_F, y_F) the location of the pixel after being displaced, t_0 the start time, τ the forecast timestep and $u(x, y)$ and $v(x, y)$ are the velocities from west to east and from north to south.

The imported data from the PATTERN network (section 2.3.1) are already edited by a clutter filter and a noise filter. After van Horne (2003) this step is necessary to ensure an undisturbed functionality of the APEX algorithm. The imported COSMO data don't need such a pre-filtering because modeled data are free from such measurement perturbations.

The execution of the algorithm follows seven steps:

In the first step, the rainfall field data are filtered by a two-dimensional convolution between the input field and a low-pass averaging filter. This technique leads to a spatial smoothing. Its benefit is to remove the small scale and high intensity convective cells and to improve the large scale advection.

The second step computes a correlation between two consecutive input fields to get a mean displacement vector of the entire field during the according timestep. This global motion analysis is necessary for biasing the local area correlation [LAC] analysis, for eliminating velocities with large deviations from the global displacement direction and to assure forecasting with a uniform velocity applied to all pixels.

In the third step, the LAC analysis starts. It takes sub-images from the two input fields and calculates a field of lag cross correlation coefficients for each pair of sub-images. In this case, Van Horne chose the zero-mean, variance normalized correlation coefficient, so that the coefficient field is independent of variations in intensity and in the spatial gradient of the intensity due to normalization by mean and the variance (Van Horne, 2003). It is a function of the lags in x - and y -directions:

$$\gamma(i,j) = \frac{\sum_{x,y} [S_{t_0-t_s}(x,y) - \overline{S_{t_0-t_s}}] [S_{t_0}(x-i,y-j) - \overline{S_{t_0}}]}{\{\sum_{x,y} [S_{t_0-t_s}(x,y) - \overline{S_{t_0-t_s}}]^2 \sum_{x,y} [S_{t_0}(x-i,y-j) - \overline{S_{t_0}}]^2\}^{0.5}} \quad (2.17)$$

where $S_{t_0-t_s}$ refers to the sub-image from the first input field, called the search field, S_{t_0} refers to the sub-image from the second input field, called the sample template and x and y are the horizontal coordinates with the lags i and j respectively. Indeed this step only computes points that show rainfall in the second image (the reflectivity has to be greater than zero) and that have more than a certain percentage of rainy pixels in both sub-images. These conditions conserve computer resources.

In the fourth step, the correlation surface filtering, is due to the high variability in the relative location of the maxima in the limited area correlation surfaces over small spatial scales. Therefore, the correlation meta surface [CMS] filtering was implemented by Van Horne. For more detailed information about this method, the interested reader may have a look at Van Horne's work.

Step five is a quality control to identify still existing inferior quality displacement vectors according to three criteria:

- I) *The directional deviation of vectors from the global angle is greater than a determined angle of tolerance.*

This criterion ensures that the directional deviations of each pixel displacement from the global displacement vector is not too large and so gaps in the forecasted precipitation field are avoided.

- II) *The magnitudes of vectors is greater than a determined speed limit.*

This criterion ensures that there are no very strong speed divergencies and so gaps in the forecasted precipitation field are avoided.

- III) *The maximum correlation coefficient is smaller than a certain correlation coefficient threshold.*

This criterion ensures that too low correlation values can lead to erroneous displacements.

All these criteria avoid adverse impacts on forecast accuracy.

In the sixth step, some vectors have to be interpolated because the quality control might have eliminated vectors. For this, the x - and y -direction pixel displacements are converted into velocities in meters per second, so that there is a physical meaning. To conserve computer resources the interpolation is realized only where the second input field shows rainfall greater than zero. Then each interpolated pixel is replaced by the local average of the valid velocity values within a determined area around the considered pixel. This leads to a smoothing in the final vector field to avoid sharp changes in the displacements over short spatial scales.

In the last step, the generated velocity field is applied to the second input field to create the forecast fields. To avoid holes by a divergent displacement of pixels each pixel is advected with its eight neighboring pixels. In this case, more than one value can influence the target pixel. Therefore, the final forecast pixel is an average of all input pixels that were put into that location (Figure 2.12).

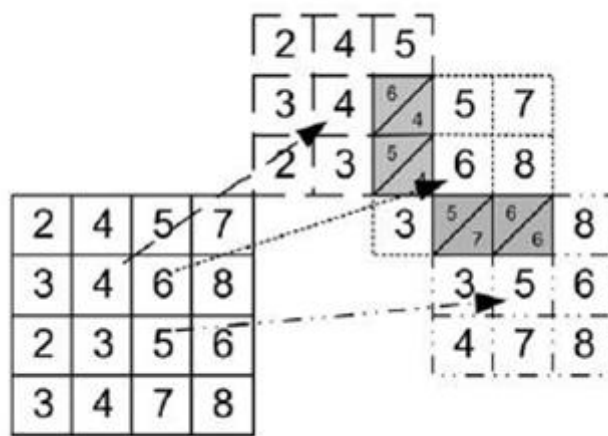


Figure 2.12: Advection scheme used by the APEX nowcasting method. [Van Horne, 2003]

The calculated forecast timestep then is set as initial timestep and the whole procedure will be repeated. Further details to the APEX algorithm can be found in Van Horne (2003).

3 Adaptation of APEX

The basic concept of the APEX algorithm by Van Horne (2003) is already discussed in the chapter 2.5. For its application with the PATTERN and COSMO data, some adaptations were made. The first part of this work tests and adapts the APEX tool in a way that it can be used as instrument for filtering the convective evolution of a precipitation cell or area on the LES scale. To get an idea how the free parameters influence the functionality of the APEX tool, they are varied over a small range around the original setting based on an exemplary precipitation event from the 19th of July 2012, 06 – 07 UTC. Especially the CSI is taken as index for an improvement or deterioration of the precipitation forecasts. First precipitation forecasts still show a variety of artificial behavior of the rainfall fields. These erroneous displacements are removed widely by the variation of the free parameters and the implementation of additional filters. With relation to these tests (section 3.1) the final APEX settings for this work (section 3.2) are determined.

3.1 First APEX tests and modifications

Thankfully, the APEX algorithm by Van Horne (2003) is appended as program code to his work. A detailed user's guide describes the meaning of various parameters which are cited in the following and summarized in Table 3.1:

FILTER_ROWS and FILTER_COLS:

Sets the vertical and horizontal size of the filter used for scale separation filtering done prior to the local correlation analysis. The values of the filter size parameters should be odd numbers so the filter can be properly centered.

MAX_SHIFT:

Component of the field parsed from the first input file. The field is a square with a side length of $2 * \text{MAX_SHIFT} + 1$ whose center pixel is the pixel that the correlation surface and resulting vector displacement correspond to. The value of this parameter can be either even or odd.

CORR_BOXSIZE:

Size of the sample from the second input file that is correlated against the **field** (defined above) in the local correlation analysis. This number should be smaller than $2 * \text{MAX_SHIFT} + 1$ and an odd number to produce a good correlation analysis and a sub-image that is centered on the pixel in question.

X_RES and Y_RES:

The horizontal resolution of the input files in meters.

TIME_SPACING:

The temporal resolution of the input files in minutes.

ANGLE_TOL:

Specifies the maximum deviation, in degrees, between a local vector and the global vector computed in the global correlation analysis.

RAIN_THRESH:

A minimum filtered rainfall value allowed to persist through the code.

WX_MIN:

A minimum percentage of valid weather in the **sample** and **field** subimages needed to perform a local correlation between the two sub-images.

RANGE:

A distance parameter that is used in multiple instances to define areas for interpolation or filtering. Used as a side length in the correlation meta surface [CMS] filtering process and as a side length of an area of influence for vector interpolation.

SIGMA:

Used in the generation of the two dimensional Gaussian filter employed for CMS filtering. In conjunction with the RANGE parameter, SIGMA serves as an input to the *fspecial* function found in the image processing tool box.

Z_THRESH:

Sets a minimum correlation coefficient value for a valid maximum.

SPEED_LIMIT:

Sets a maximum displacement for local vectors. Vectors with magnitudes over this value are eliminated and interpolated later.

SEARCH_RADIUS:

Defines an area around the endpoint of the global vector in which to search for the maximum correlation coefficient. Is a component of the correction values, that turn displacements from the global vector endpoint into displacements from the center pixel.

Table 3.1: List of parameters for the APEX algorithm with nominal values based on the spatial and temporal resolution shown in the work of Van Horne (2003). For the individual use of APEX these parameters should be adapted accordingly (Van Horne, 2003).

Parameter Name	Nominal Value	Units
FILTER_ROWS	41	pixels
FILTER_COLS	41	pixels
MAX_SHIFT	10	pixels
CORR_BOXSIZE	7	pixels
X_RES	4762.5	meters
Y_RES	4762.5	meters
TIME_SPACING	15	minutes
ANGLE_TOL	30	degrees
RAIN_THRESH	0.1	mm
WX_MIN	0.25	fraction
RANGE	11	pixels
SIGMA	1.5	pixels
Z_THRESH	0.55	fraction
SPEED_LIMIT	5	pixels
SEARCH_RADIUS	3	pixels

The nominal values are set to the spatial and temporal resolution of Van Horne's test area. In the case of the PATTERN X-band radars, the resolutions in time and space are much higher than the nominal values for the variables X_RES, Y_RES and TIME_SPACING which determine the spatial resolution in x- and y-direction and the temporal resolution of the two consecutive input files and that of the lead time. The PATTERN input data are available every 30 seconds. However, the timestep is set to 4 min because a too short or too long timestep leads to freeze frames, so no advection can be computed if the temporal resolution does not fit

to the spatial resolution. The latter is fixed to 250 m by the adjustment of the four single X-band radar signals in the area of Itzehohe to one composite image. For the adaptation of the other parameters in Table 3.1 a single precipitation event is chosen as example (19.07.2012, 06 – 07 UTC) and then the parameters are varied over a range of values around the nominal value. The CSI serves as indicator for an improvement or deterioration of the forecast.

First APEX runs with real observation data still exhibit errors. These include e.g. fragmentary displacement of precipitation fields, so in particular the peripheral areas of the image are not advected. Sometimes the transition between advected and non-advected parts of the same precipitation field is visible as a linear cut and between these two parts a fishbone pattern develops with every timestep. In other cases, it is possible that the whole image is frozen and no advection takes place. Furthermore, it could be that a single correlation pair of two images shows a totally different displacement direction than the pair before or after the faulty one. Looking at the verification scores (CSI, POD and FAR) it is remarkable that in many cases the FAR is nearly zero and as consequence the CSI and POD are almost the same. To tackle all these problems, it is necessary to find and to test the most important free parameters for the tuning of the APEX tool.

The variation of the parameters FILTER_ROWS and FILTER_COLS (values 41, 21, 11 and 1) shows slight differences of the precipitation patterns. With lower filter values more pixels can be advected but the shape of the precipitation area is more unstable and the risk for gaps within such an area is higher. To determine the impact on the CSI only the correlation pair 6.00 UTC and 6.04 UTC is considered and the maximum lead time is restricted to 16 min. Table 3.2 shows that with lower filter settings the CSI gets higher. For further tests a value of 11 is set for both, FILTER_ROWS and FILTER_COLS.

Table 3.2: CSI values for the correlation pair 2012/07/19 6:00 UTC / 6:04 UTC with lead times up to 16 min and a timestep of 4 min for different FILTER_ROWS and FILTER_COLS values.

Filter / Lead time	0 min	4 min	8 min	12 min	16 min
41	1	0.6684	0.5157	0.4255	0.3688
21	1	0.6806	0.5305	0.4413	0.3801
11	1	0.7012	0.5520	0.4547	0.3952

In a next step, the parameters MAX_SHIFT and CORR_BOXSIZEx are varied. MAX_SHIFT is set to the values 40, 80 and 100 and CORR_BOXSIZEx accordingly to the values 27, 47 and 67. The resulting images show that with higher values of the two parameters the erroneous displacement direction of some correlation pairs is corrected. However, the boundaries of the

precipitation field stay fixed and the fishbone patterns show longer stripes. For the investigation of the CSI the same procedure like above is performed. The restriction to four lead time steps and one correlation pair saves much computing time. First of all, only the MAX_SHIFT value is changed with a fixed CORR_BOXSIZE value of 27. The computing time increases from 140 s to 145 s between MAX_SHIFT = 40 and MAX_SHIFT = 80 and from 145 s to 280 s between MAX_SHIFT = 80 and MAX_SHIFT = 100 whereas the CSI values stay nearly constant (Table 3.3). Because of the subjective better displacement of precipitation fields with increasing MAX_SHIFT its value will be fixed to 80 in the further tests. Afterwards, the CORR_BOXSIZE value is varied. The CSI values improve with increasing CORR_BOXSIZE values but also the computing time strongly increases. Therefore, a CORR_BOXSIZE value of 47 is set for further tests.

Table 3.3: CSI values for the correlation pair 2012/07/19 6:00 UTC / 6:04 UTC with lead times up to 16 min and a timestep of 4 min for different MAX_SHIFT and CORR_BOXSIZE values. At first, only the MAX_SHIFT value is varied, then the CORR_BOXSIZE value is varied with a fixed MAX_SHIFT = 80.

MAX_SHIFT / Lead time	0 min	4 min	8 min	12 min	16 min
40	1	0.7012	0.5520	0.4547	0.3952
80	1	0.7046	0.5519	0.4514	0.3934
100	1	0.7056	0.5540	0.4541	0.3947
CORR_BOXSIZE / Lead time	0 min	4 min	8 min	12 min	16 min
27	1	0.7046	0.5519	0.4514	0.3934
47	1	0.7102	0.5624	0.4548	0.3947
67	1	0.7126	0.5671	0.4534	0.3952

Table 3.4 presents the CSI results for different RAIN_THRESH, SEARCH_RADIUS and SPEED_LIMIT values. An increasing RAIN_THRESH value decreases the CSI. So, the preset value of 0.1 mm remains. A SEARCH_RADIUS of 7 instead of 3 doesn't improve the CSI but increases the computing time from 233 s to 402 s in this example. Consequently, the preset value of 3 is set for further application. An increasing SPEED_LIMIT value increases also the CSI without changing the forecast images much. Here, a SPEED_LIMIT of 20 is set for all further tests.

Up to now, the last line of Table 3.4 shows the best CSI which can be controlled by the above tested parameters. Before continuing with the parameter variations, a basic setting in the APEX code is changed which has a great impact on the magnitude of the CSI: Van Horne (2003) let the choice in the APEX algorithm how to calculate the verification scores. The user is able to select either a point to point matching method (traditional verification method) or a

3 Adaptation of APEX

Table 3.4: CSI values for the correlation pair 2012/07/19 6:00 UTC / 6:04 UTC with lead times up to 16 min and a timestep of 4 min for different RAIN_THRESH, SEARCH_RADIUS and SPEED_LIMIT values.

RAIN_THRESH / Lead time	0 min	4 min	8 min	12 min	16 min
0.1	1	0.7102	0.5624	0.4548	0.3947
	1	0.7088	0.5605	0.4517	0.3901
SEARCH_RADIUS / Lead time	0 min	4 min	8 min	12 min	16 min
3	1	0.7102	0.5624	0.4548	0.3947
	1	0.7012	0.5647	0.4549	0.3918
SPEED_LIMIT / Lead time	0 min	4 min	8 min	12 min	16 min
5	1	0.6788	0.4988	0.4122	0.3639
	1	0.7102	0.5624	0.4548	0.3947

point to neighborhood matching method (fuzzy verification). The different methods are explained in Chapter 2.2. Furthermore, it is possible to select a squared verification area, a cross verification area or a rectangle verification area with optional window size, respectively. For this work a 3x3 pixel verification area is set. If at least one pixel in this area indicates rain, the initial point will be counted as a hit. The adjustment from the point to point matching (which was preset) to the squared verification area influences the CSI as shown in Table 3.5.

Table 3.5: Improvement of the CSI values through the adjustment of the verification method from point to point matching (traditional method) to a neighborhood matching (fuzzy verification).

Verification area / Lead time	0 min	4 min	8 min	12 min	16 min
1 pixel	1	0.7102	0.5624	0.4548	0.3947
	1	0.7771	0.6859	0.6217	0.5476

Based on current presented settings, the parameter ANGLE_TOL shall be tested. For this, the whole hour from 6 UTC to 7 UTC is calculated and not only one correlation pair like in the previous tests. Table 3.6 shows that the difference in the CSI scores between ANGLE_TOL = 10 and ANLGE_TOL = 30 is very small. For ANGLE_TOL = 60 there can be achieved clearly higher CSI scores. Looking at the precipitation images, for this example there are one the one hand slightly less fishbone patterns with higher values for ANGLE_TOL but on the other hand the risk for gaps within the rainfall field is higher. Figure 3.1 shall present this fact exemplary.

The red marked area shows that some of the fishbone patterns disappear with higher ANGLE_TOL. This is also visible in other images of this hour (not shown here). However,

Table 3.6: CSI values for the APEX forecasts from the 19th of July 2012 6:00 UTC - 7:00 UTC with lead times up to 16 min and a timestep of 4 min for different ANGLE_TOL values.

ANGLE_TOL / Lead time	0 min	4 min	8 min	12 min	16 min
10	1	0.8082	0.7028	0.6282	0.5754
30	1	0.7946	0.6912	0.6179	0.5679
60	1	0.8274	0.7249	0.6523	0.5974

the green marked area is a counterexample, so at other places new erroneous forecasts appear. Furthermore, in many figures of this hour more gaps arise like in the magenta marked area. Because of the high uncertainty of the effect on the visual artifacts the ANGLE_TOL value stays 30 degrees although an angle of 60 degrees provides higher CSI scores.

APEX can handle both, radar reflectivity factors Z [dBz] or rain rates R [mm]. The upper tests were performed all with radar reflectivity factors (as can be seen in Figure 3.1) because that is the unit of the available PATTERN data. However, the rain rate R is a more reader-friendly quantity. For this reason, the input data for APEX are converted to rain rates R in the following (see sections 2.3.1 and 2.3.2 for conversion details). Because R is not normally distributed, the scales of the colorbars must be logarithmic. Otherwise, huge parts of the precipitation images wouldn't be visible because the rain rates are too weak. A secondary effect of this conversion from Z to R is only noticeable with a look at the verification scores presented in Figure 3.2.

The left side of Figure 3.2 shows the averaged scores of a PATTERN example from the 28th of July 2012 from 8 to 9 UTC calculated in Z whereas the right side shows the same example but

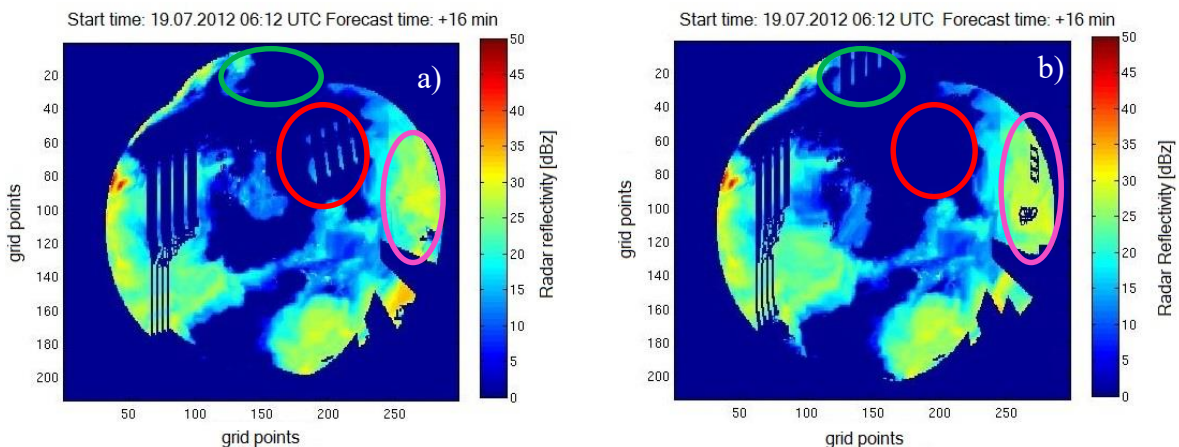


Figure 3.1: The same precipitation event (2012/07/19 6 - 7 UTC) with a) ANGLE_TOL = 10 and b) ANGLE_TOL = 30. The main differences are marked.

3 Adaptation of APEX

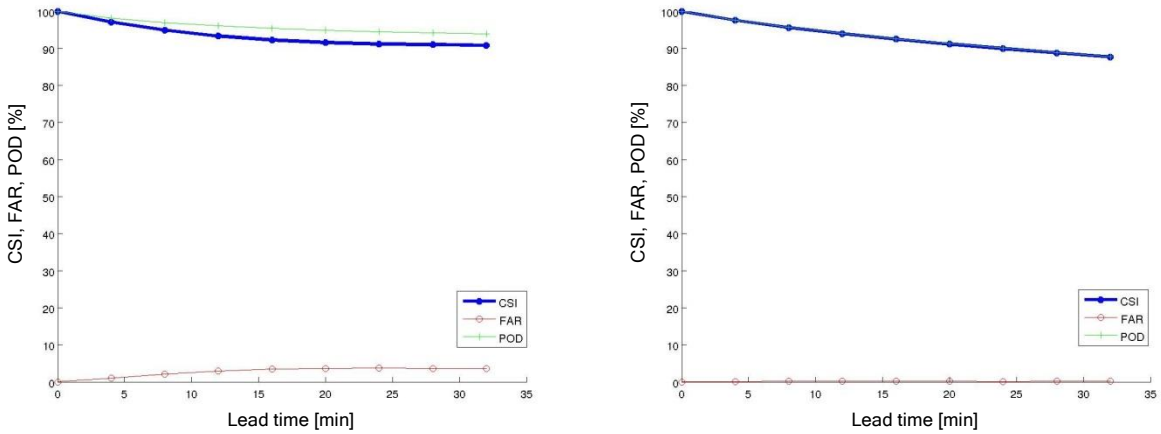


Figure 3.2: Comparison of the averaged verification scores for the 28th of July 2012 between 8 and 9 UTC (PATTERN data) on the left side calculated in radar reflectivity Z , on the right side calculated in rain rate R .

calculated in R . Obviously, there are no more false alarms when using rain rates as input data for APEX and resulting from this, the CSI and POD are exactly the same. The reason for this behavior is that in the data field of rain rates a lot of values are near zero. These values are not visible in the precipitation image but they count as precipitation pixels for the categorical verification scores. To tackle this problem the threshold for a precipitation pixel is set to 1 mm, so that all values below 1 do not count as precipitation. This threshold is variable and freely selectable by the user. At this point, there is the possibility to manipulate the scores manually which makes a comparison to other forecast tools impossible.

A further detail that has to be taken into account when looking at the scores is precipitation that reaches the radar area during the forecast. It could decrease the CSI or other scores which are defined with misses in the denominator because misses are produced by this procedure. In this thesis all the pixels in the boundary area (towards the advection direction) which are not part of the forecast are not considered, so following precipitation in the observation field is not taken into account by the calculation of verification scores.

A parameter from Table 3.1 that has a great impact on the fishbone patterns and the frozen parts of the images is the WX_MIN value. Figure 3.3 presents in a) a COSMO simulated precipitation event from the 3rd of August 2012 at 15:12 UTC. The APEX forecast with a lead time of 32 min shows in b) that with the original WX_MIN value of 0.25 there are some fishbone patterns at the left side and the lower part of the image is frozen. In c) this value was changed to 0.05 and obviously both problems are solved. However, applying this to other precipitation examples not all of the artifacts of this kind disappear. That is why an additional modification is done which makes forecast visually better. In the APEX code there is a function that interpolates missing vectors with the average of the surrounding vector magnitudes. The half boxsize of the interpolation area is multiplied by a factor of ten. This procedure reduces the amount of frozen precipitation cells enormously. The parameters

SIGMA, Z_THRESH, RANGE and RAIN_THRESH stay preset to the default values.

A problem that is only visible by eye with negligible effect on the verification scores is that some precipitation displacements leave a kind of traces at arbitrary positions of the edges of the precipitation field (Figure 3.4). The cause of these traces could not be found in the program code. That is why an additional filter is implemented which removes areas of less than twenty contiguous pixels. Figure 3.4 shows the effect of this filter on the basis of two examples, one with PATTERN data and the other one with COSMO data. On the left side, the rainfall field is not yet displaced (forecast time = 0). The right side of the image shows the rainfall field 32 min later, displaced by the APEX forecast with and without the additional filter, respectively. Obviously, this kind of filter is very effective. Just in the upper part of the figure (COSMO data) there is one trace left. Other problems like gaps in the precipitation field remain.

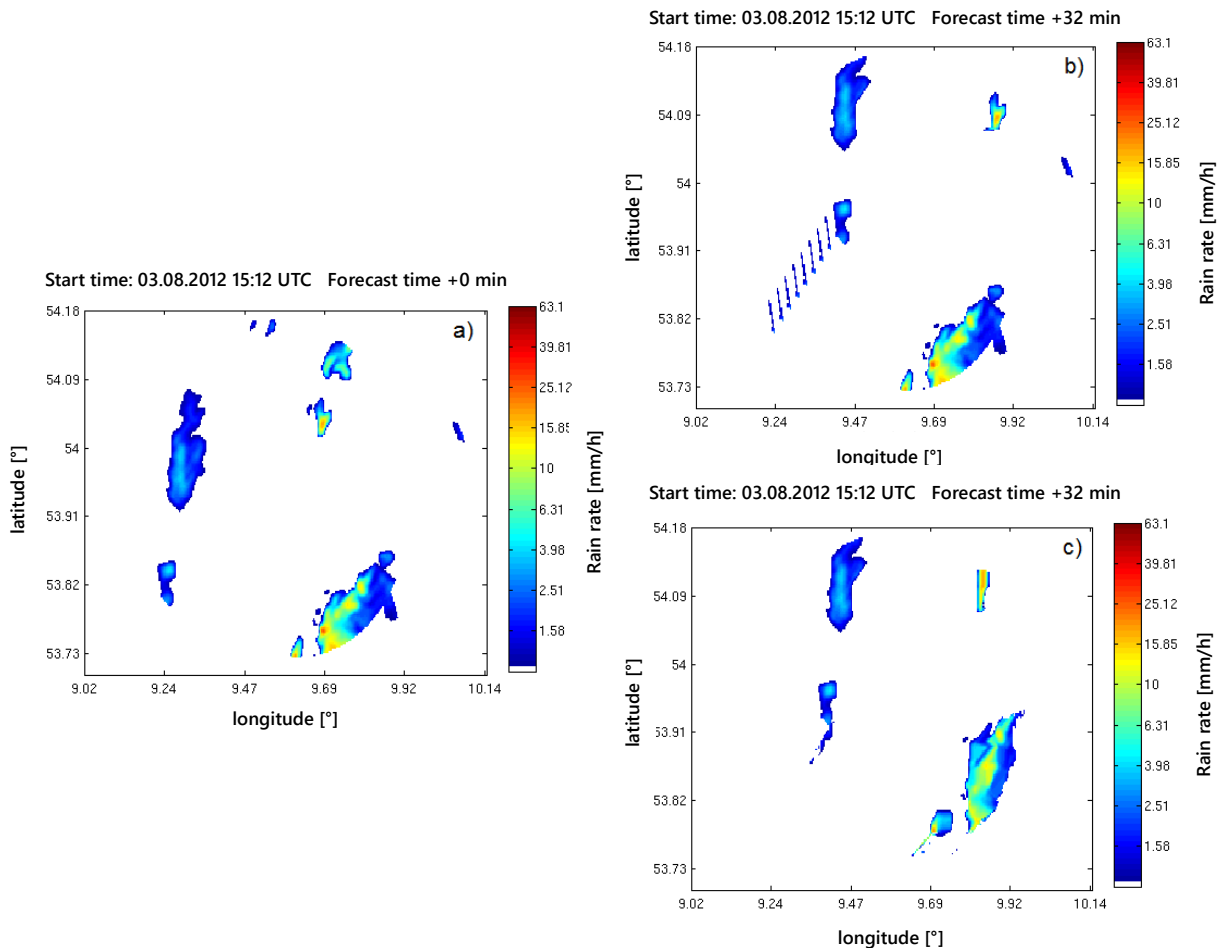


Figure 3.3: APEX forecast for the 3rd of August 2012 with COSMO data starting from a) 15:12 UTC up to a maximum lead time of 32 min with b) the preset WX_MIN value of 0.25 and c) the modified WX_MIN value of 0.05.

3 Adaptation of APEX

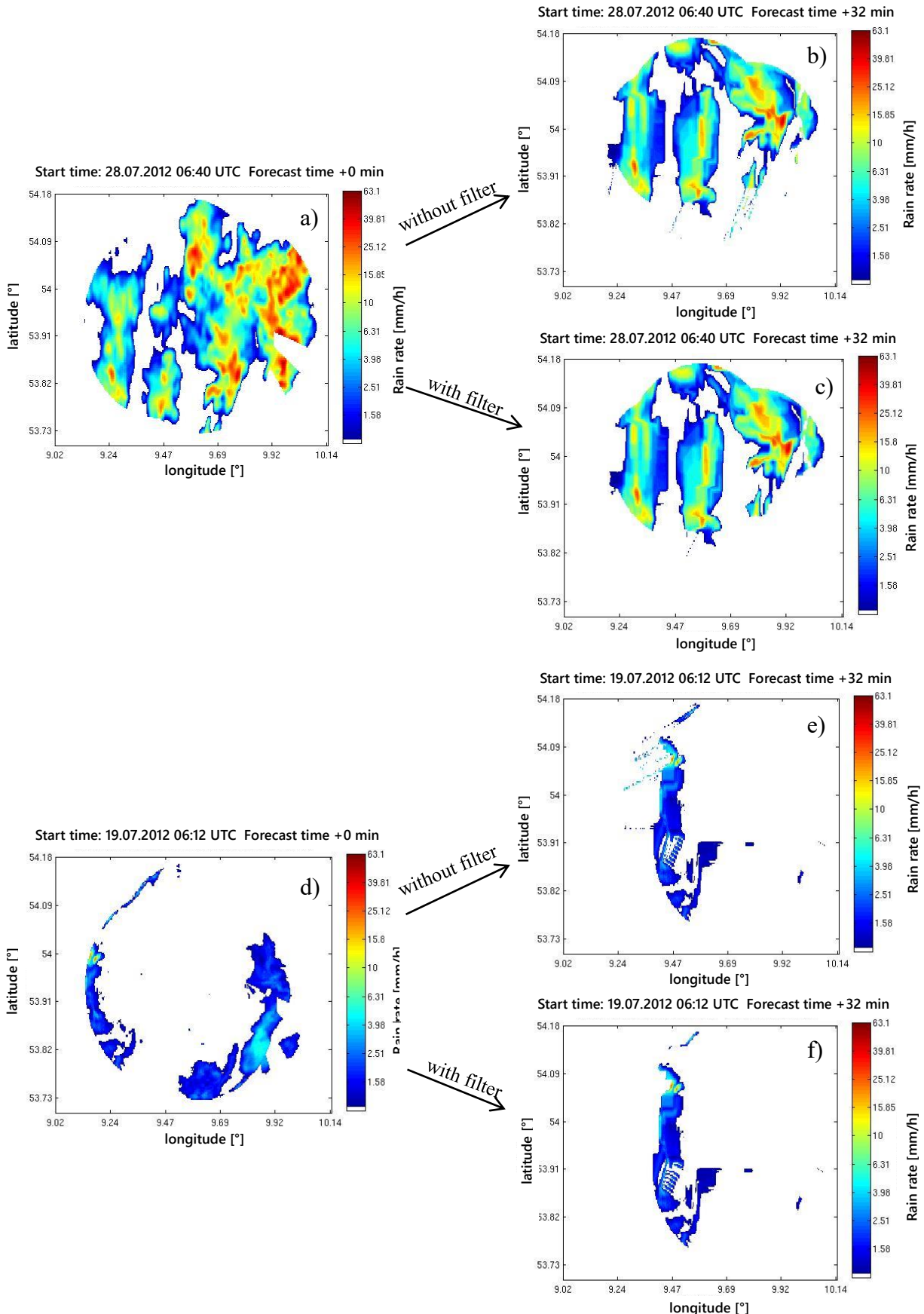


Figure 3.4: All areas with less than twenty contiguous pixels are removed. The images a) and d) show the original precipitation field at the according time for COSMO data (a) and PATTERN data (d), respectively. The images b) and e) show the unfiltered precipitation fields. After application of the filter that removes small pixel areas, the images c) and f) result.

To avoid these gaps and frozen parts of the images an additional implementation is done. The wind field is smoothed with a 2D smoothing function that builds means over a rectangular area within the field. Thus, strong transitions from higher to lower velocities disappear and the displacement the rainfall field becomes more realistic.

With the methods and modifications described in this chapter many of the problems could be solved for the chosen test events but they can still exist for single other events. However, further improvement probably would cost a lot of time and makes the forecast only visually better but the verification scores wouldn't change much. That is why the current settings are fixed and summarized in section 3.2.

3.2 Final APEX settings

The final values of the different setting options and modifications in the APEX algorithm are summarized in the following. First of all, the parameters of Table 3.1 are listed here again in Table 3.7 with the adapted values resulting from the tests described in the previous section.

The spatial resolution of 250 m, represented by the variables X_RES and Y_RES, is determined by the PATTERN and COSMO input data. Based on these values the temporal resolution must be adapted from 15 min to 4 min. Higher temporal resolutions need much more CPU resources and with too low resolutions it becomes more and more difficult to correlate the consecutive images correctly. Likewise, the parameters MAX_SHIFT and CORR_BOXSIZE influence the CPU time enormously but they also have a great effect on the shape and structure of the precipitation fields. So, the visual improvement of the forecast fields is highly dependent on these two parameters. Reasonable results concerning the subjective analysis of the precipitation images as well as the objective analysis looking at the CSI scores are found with values of MAX_SHIFT = 80 and CORR_BOXSIZE = 47. The filter values which smooth the input fields are set to 11. To eliminate some images without advection the WX_MIN value is set to 0.05 instead of 0.25 and the SPEED_LIMIT value is modified from 5 to 20. Default values are used for the parameters ANGLE_TOL, RAIN_THRESH, RANGE, SIGMA, Z_THRESH and SEARCH_RADIUS.

Furthermore, the interpolation area for the interpolation of missing or erroneous vectors is extended by a factor of 10 for the half boxsize of this area. Moreover, an additional filter that removes all precipitation with an expanse lower than 20 contiguous pixels is implemented. The wind field is smoothed because in the original APEX algorithm some gradients from

3 Adaptation of APEX

Table 3.7: List of parameters for the APEX algorithm adapted to the PATTERN and COSMO area.

Parameter Name	Value	Units
FILTER_ROWS	11	pixels
FILTER_COLS	11	pixels
MAX_SHIFT	80	pixels
CORR_BOXSIZE	47	pixels
X_RES	250	meters
Y_RES	250	meters
TIME_SPACING	4	minutes
ANGLE_TOL	30	degrees
RAIN_THRESH	0.1	mm
WX_MIN	0.05	fraction
RANGE	11	pixels
SIGMA	1.5	pixels
Z_THRESH	0.55	fraction
SPEED_LIMIT	20	pixels
SEARCH_RADIUS	3	pixels

higher to lower velocities seemed to be too strong. In a further step, stationarity of the wind field is set.

All these adaptations lead to really improved forecasts for the PATTERN and COSMO data on the LES scale. Especially, the modifications in the wind field, so stationarity and smoothing, correct effectively unrealistic displacement patterns in the precipitation forecast fields. Many problems and artificial behavior of forecast displacements could be solved: Gaps within precipitation fields, frozen and cut images, traces behind the precipitation areas, fishbone patterns or attached boundaries of the radar area are removed widely through the modifications. The displacement in different directions that appears in several cases between two consecutive correlation pairs could not be corrected. Probably it causes just due to the correlation analysis. Then the variation of the timestep could change this behavior but it shall be fixed to 4 min in this work. So, the few cases with this error must be treated with attention in the evaluation of the results.

4 Results and Discussion

In Chapter 3 the APEX settings for the precipitation nowcasting are specified and defined. Now the Golden Days observation data from the PATTERN X-band radar network as well as the model data from the nested COSMO model are used to simulate 32 min – forecasts with a 4 min – timestep. The results of APEX are presented in Chapter 4.1 with a focus on the comparison between the prediction of observation data and model data. The interesting question is whether there are differences in the forecast performance or in other words: Is there a higher lead time with the same forecast quality for the observation or model data? Then conclusions about the convective evolution can be drawn on the basis of categorical verification scores. In Chapter 4.2 the convective evolution is analyzed from another point of view. Here, the focus is on the variability and strength of deviations in the fields of convective evolution and the comparison of quantitative verification scores. Chapter 4.3 hints at possible constraints of the verification method and other error sources that have to be considered when the presented results are interpreted.

4.1 APEX results and evaluation using categorical scores

As mentioned in Chapter 3 the advection of rainfall fields through the APEX algorithm could be adapted and improved enormously but in some few cases there are still displacements in wrong directions or frozen images. In the following, examples for good results as well as for suboptimal results are presented. The sections 4.1.1 and 4.1.2 present the APEX forecasts for PATTERN data and for COSMO data, respectively. The results will finally be compared in section 4.1.3.

4.1.1 APEX results from observation data

On the 28th of July 2012 the PATTERN X-band radar network measures precipitation that is caused by the convergence of air masses at a cold front and warm air uplift due to positive vorticity advection. As depicted by Figure 4.1 in the radar area the precipitation coverage is high. Every subimage shows a different lead time to visualize the development and movement of the precipitation field. The areas with the strongest rain rates reach intensities up to 15 mm/h. A subjective evaluation leads to satisfying results. The displaced forecast fields look

4 Results and Discussion

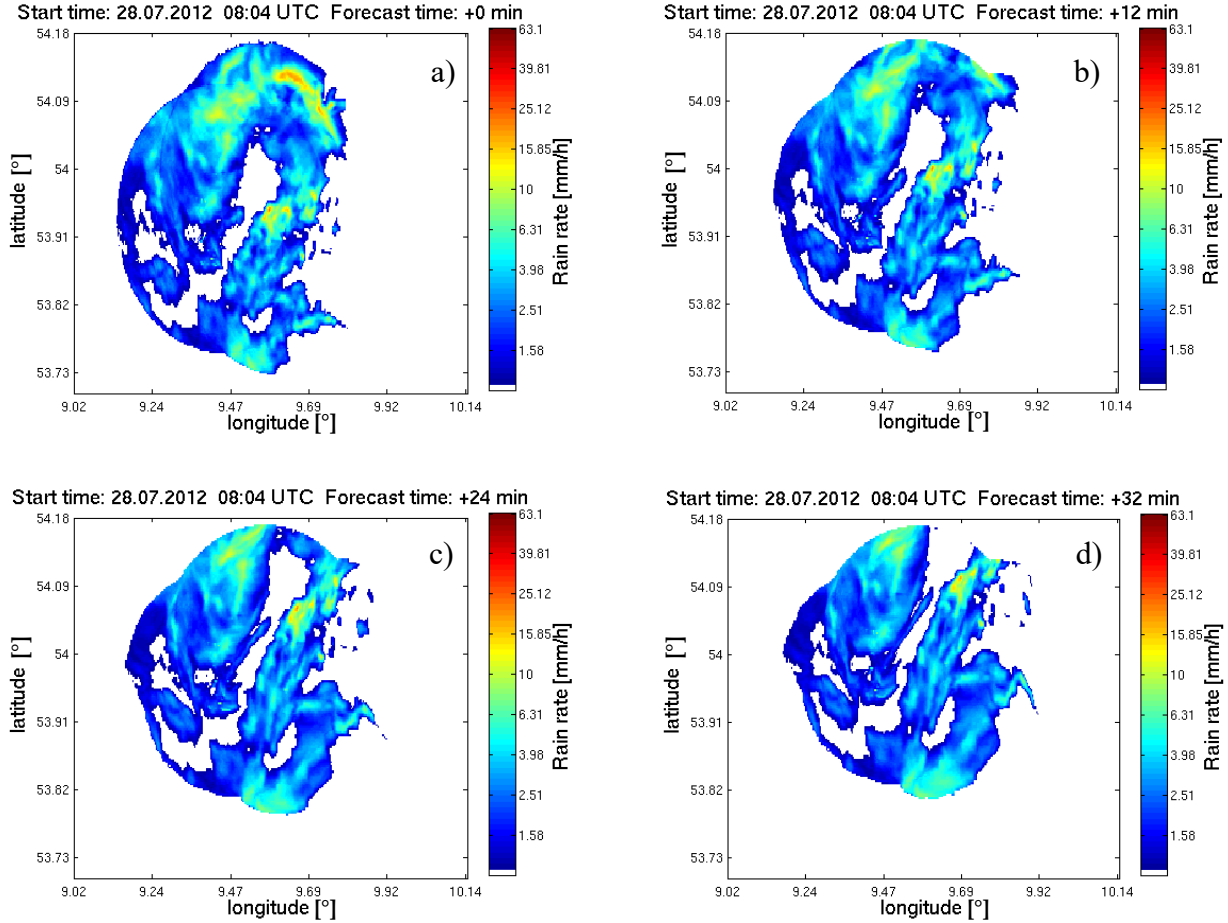


Figure 4.1: APEX forecast for the 28th of July 2012 with PATTERN data starting from 08:04 UTC with lead times a) 0 min b) 12 min c) 24 min and d) 32 min.

reasonable and reveal no artefacts.

An objective analysis can be done with the respective verification scores that are given as output from APEX. Figure 4.2 shows the development of the CSI, FAR and POD with the lead time. Every line in the figure belongs to a certain pair of two consecutive rainfall images within the denoted hour that is correlated by APEX. With a forecast timestep of four minutes a set of 14 pairs results. In all the three subimages from Figure 4.2 the spreading of the pairs increases with forecast time. Such a behavior can be expected because longer forecast times result in higher forecast errors and larger variability of forecast accuracy. Also the trend of the curves proves this: There is a steady decreasing of the CSI and POD values whereas the FAR increases with the forecast time. In case of the CSI the decrease means that the ratio of hits over the sum of hits, misses and false alarms becomes smaller. In other words, there are more misses and false alarms with increasing forecast time. In case of the POD it is the same without considering the false alarms. That is why the POD is always higher than the CSI in

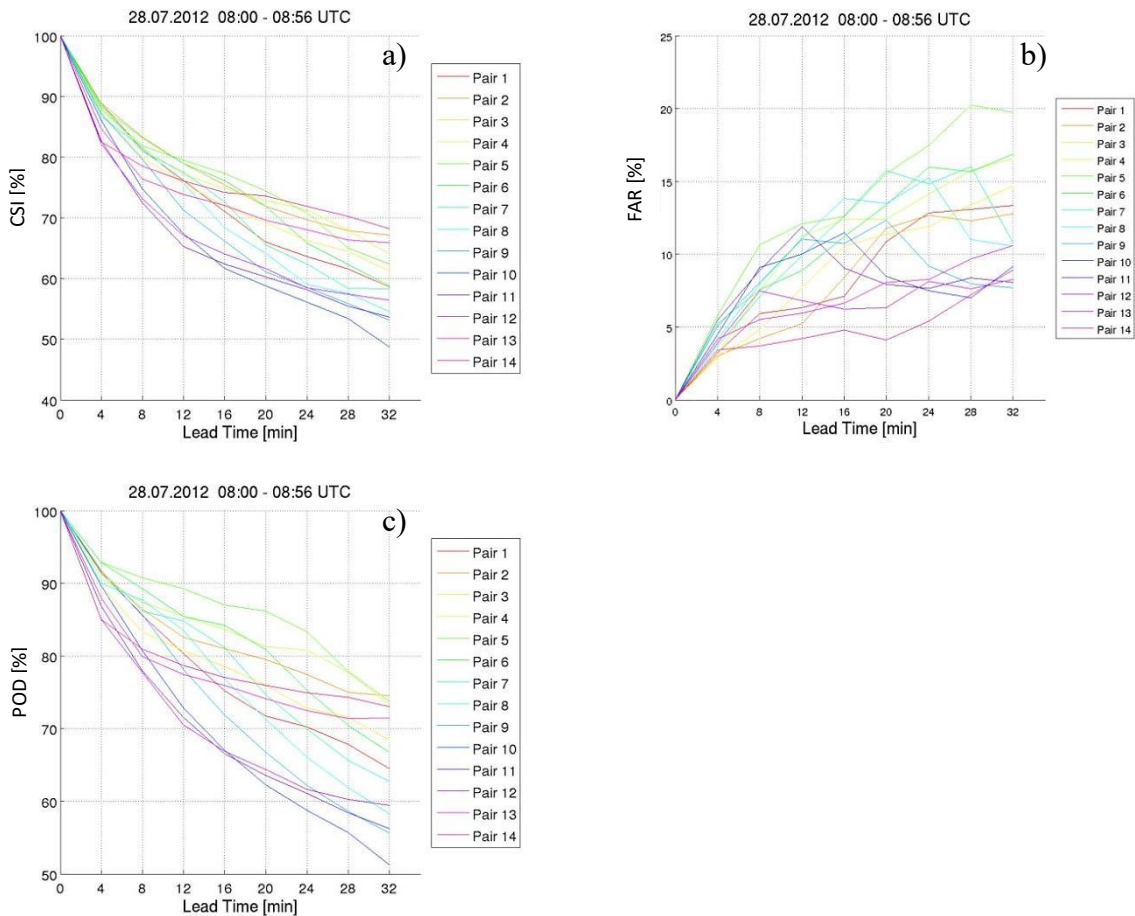


Figure 4.2: Verification scores of the APEX forecasts of the 28th of July 2012 (PATTERN data). Every line results from a pair of two consecutive rainfall images within 8 and 9 UTC. The subimage a) shows the CSI, b) the FAR and c) the POD.

the presence of false alarm values. The increase of the FAR curves means that the number of hits sinks with increasing forecast time and the fraction of false alarms increases.

This assessment of the forecast quality could not be drawn subjectively from the rainfall forecast images (Figure 4.1) even with a comparison to the observed radar images.

The number of figures can be reduced by summarizing these three verification scores in one figure and averaging the single correlation pairs over one hour. Figure 4.3 shows the averaged scores with the standard deviations of all considered forecasts. An increase of the standard deviations with forecast time is observable in every score. This is simply due to the increasing inaccuracy of a prediction with forecast time.

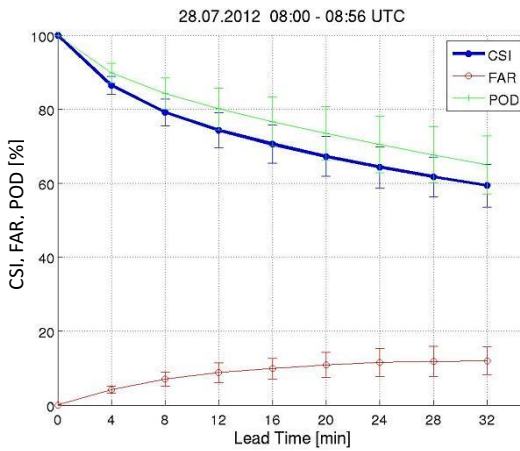


Figure 4.3: Averaged verification scores of the APEX forecast of the 28th of July 2012 (PATTERN data) over one hour from 8 to 9 UTC.

Not all the APEX forecasts have as good results as presented in Figure 4.3. In spite of several tuning procedures in the APEX tool there are still precipitation events that cause erroneous displacements. On the 3rd of August 2012 the radar images indicate precipitation that is caused by large-scale surface heating leading to thermal low and thunderstorm development. The precipitation coverage between 15 and 16 UTC is very low. Under these circumstances correct forecast is very difficult for APEX. Figure 4.4 a) and b) are almost the same identical. Obviously only one single precipitation cell is displaced by a forecast time of 32 min (marked red) while the rest of the image is frozen. This forecast is based on the correlation images from 15:04 UTC and 15:08 UTC. Likewise, other correlations in the same hour lead to totally wrong displacement directions (not shown here). Only a few correlations lead to reasonable displacements. Moreover, there is almost no precipitation in the observation data in the second part of this hour. Consequently, the verification scores (Figure 4.5) are significantly worse than those of the previous example (Figure 4.2).

The scores fall to zero (CSI, POD) or they rise to 100 (FAR) very quickly. This effect is also reflected by the averaged scores (Figure 4.6). The CSI and POD sink much faster than in Figure 4.3 and the FAR goes to 100 % very quickly. Also the standard deviations representing the spread of the single pair curves are much higher than in the example before.

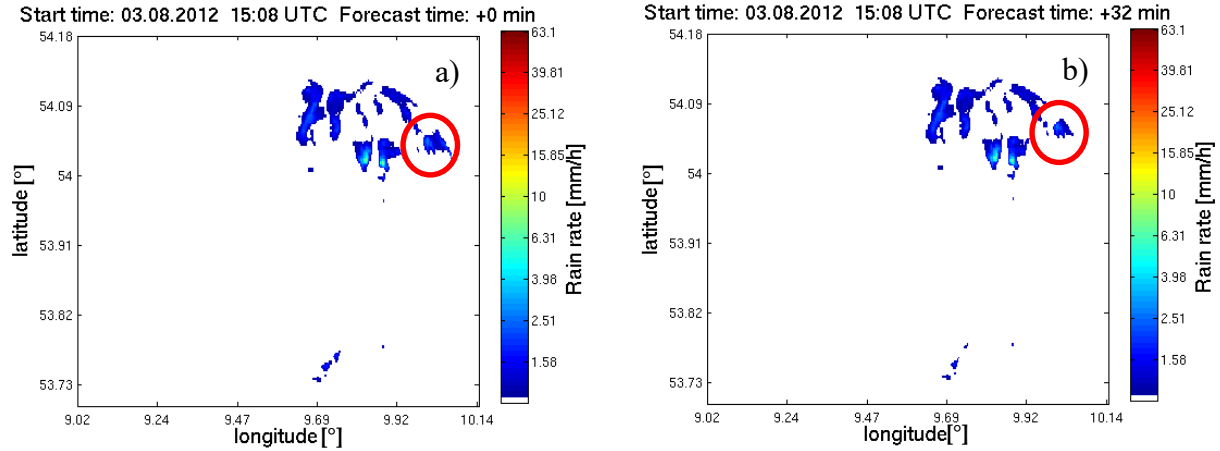


Figure 4.4: APEX forecast for the 3rd of August 2012 with PATTERN data starting from 13:08 UTC with lead times a) 0 min and b) 32 min illustrating an erroneous forecast.

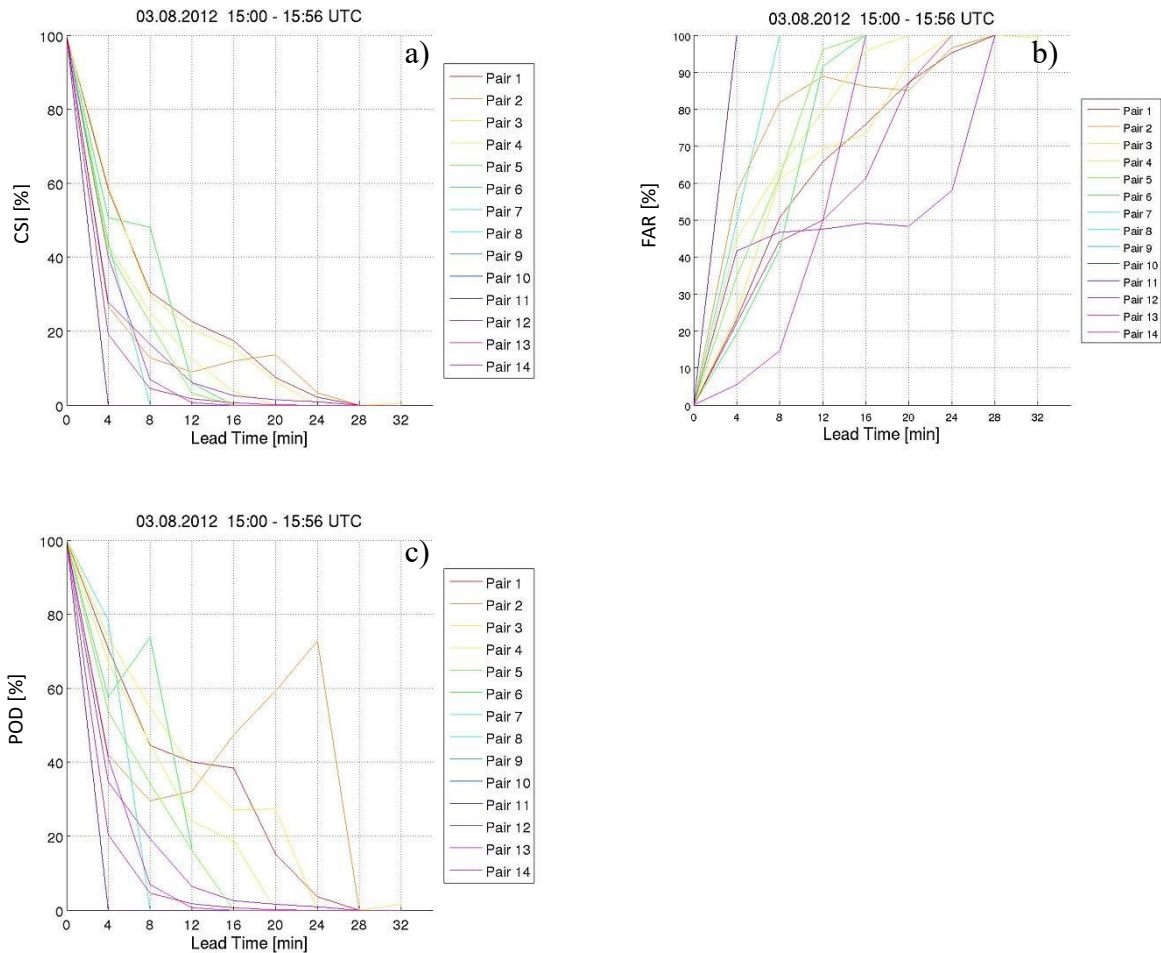


Figure 4.5: Verification scores of the APEX forecasts of the the 3rd of August 2012 (PATTERN data). Every line results from a pair of two consecutive rainfall fields within 15 and 16 UTC. The subimage a) shows the CSI, b) the FAR and c) the POD.

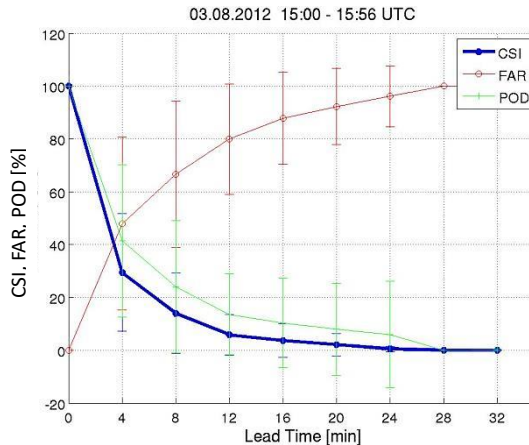


Figure 4.6: Averaged verification scores of the APEX forecast of the 3rd of August 2012 (PATTERN data) over one hour from 15 to 16 UTC.

These two examples - one with good APEX results and the other one with bugs - illustrate that the forecast quality isn't the same for different precipitation events. Most examples of the Golden Days that are considered in this work provide plausible scores. Probably, APEX has the greatest trouble with low coverage precipitation fields.

4.1.2 APEX results from model data

Similar to the previous section where the results of the APEX forecast for PATTERN data were presented, now the forecasts for COSMO data are discussed based on one example of a successful forecast and one example with low verification scores.

On the 19th of July 2012 the PATTERN X-band radar network measures precipitation that is caused by positive vorticity advection and forced uplift between 6 and 9 UTC. Figure 4.7 a) shows the modeled rain intensity by COSMO at 6.24 UTC and the subimages b), c) and d) present the APEX forecasts starting from the image a). The areas with the strongest rain rates reach values up to 50 mm/h. Like in the PATTERN example the displacement reveals no obvious problems. Comparing Figure 4.1 (PATTERN) and Figure 4.7 (COSMO) by eye give no great differences between a forecast of PATTERN data and one of COSMO data. Having a closer look also to additional images (other dates that are not shown here) one can recognize that the PATTERN images exhibit sharper edges of precipitation areas and more small cell structures.

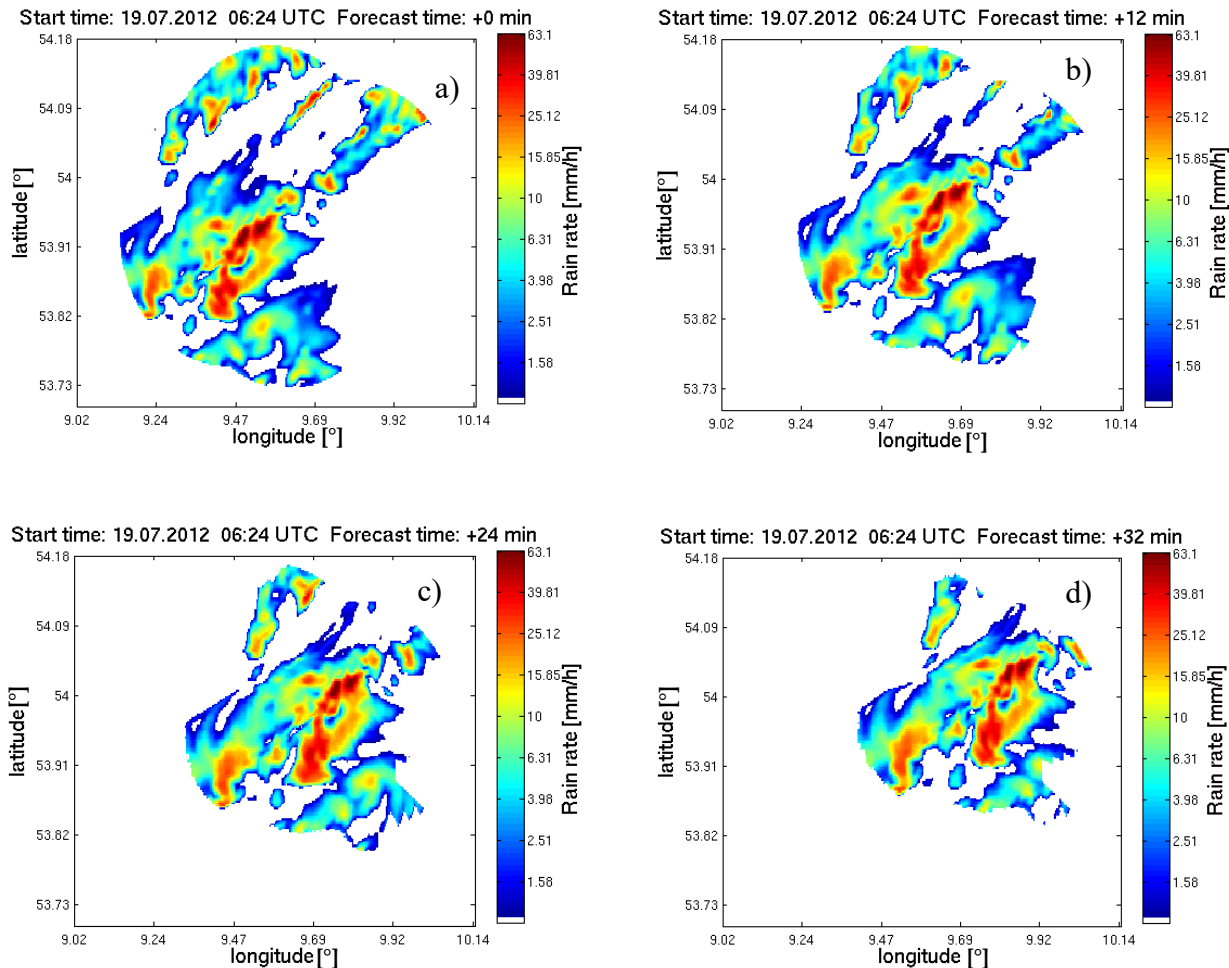


Figure 4.7: APEX forecast for the 19th of July 2012 with COSMO data starting from 06:24 UTC with lead times a) 0 min b) 12 min c) 24 min and d) 32 min.

The single verification scores for each correlation pair (Figure 4.8) as well as the averaged scores (Figure 4.9) look similar to the corresponding result of the PATTERN example (Figure 4.2 and Figure 4.3). The CSI and POD are decreasing monotonously, the FAR is increasing monotonously. The spread of the single scores (or standard deviation of the averaged scores) is increasing with increasing forecast time. However, this is only a single example. Therefore, a comparison of all the investigated cases from the Golden Days will be done in the section 4.1.3

4 Results and Discussion

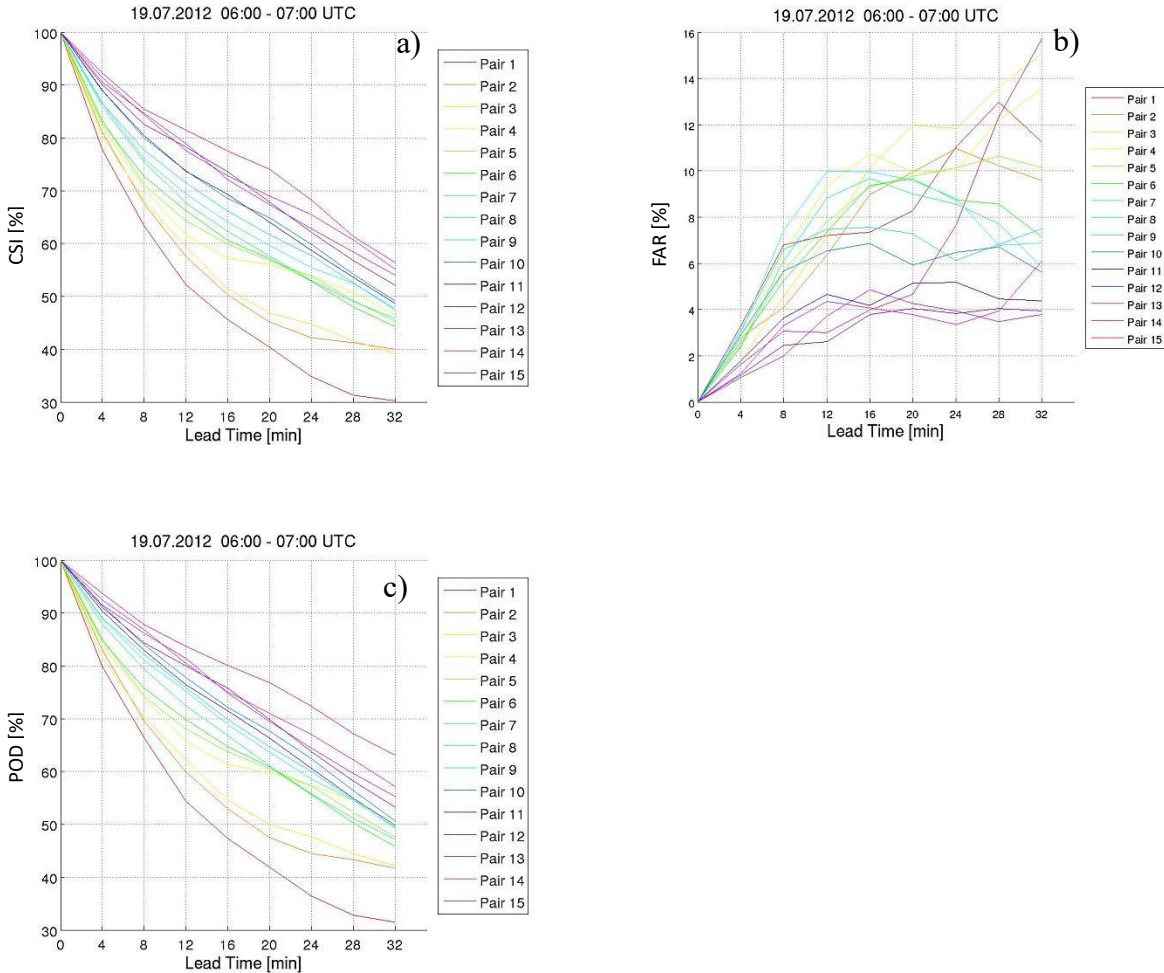


Figure 4.8: Verification scores of the APEX forecasts of the 19th of July 2012 (COSMO data). Every line results from a pair of two consecutive rainfall fields within 6 and 7 UTC. The subimage a) shows the CSI, b) the FAR and c) the POD.

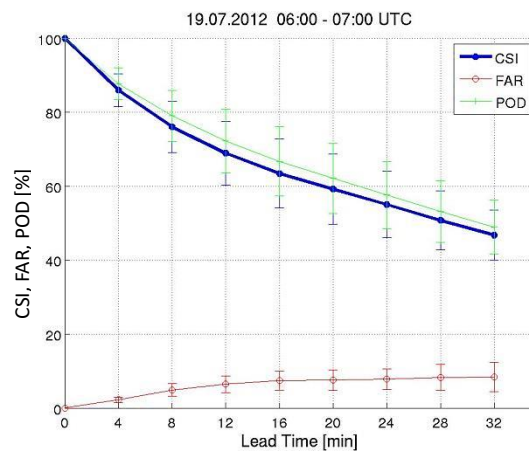


Figure 4.9: Averaged verification scores of the APEX forecast of the 19th of July 2012 (COSMO data) over one hour from 6 to 7 UTC.

The next example is from the 3rd of August 2012 between 14 and 15 UTC. The COSMO model simulates a low precipitation coverage at this day. Figure 4.10 depicts the APEX forecast starting from 14:24 UTC. Although there are only some single rainfall cells, the nowcasting tool could displace all of it. In the previous section a similar example for the PATTERN data led to some frozen precipitation cells. There is no obvious explanation for this different behavior. Nevertheless, the decreasing of the CSI and POD and the rising of the FAR is stronger than in the example before (Figure 4.11 and Figure 4.12). This confirms the hypothesis that the APEX algorithm works better with higher precipitation coverage or stratiform precipitation than with small cells.

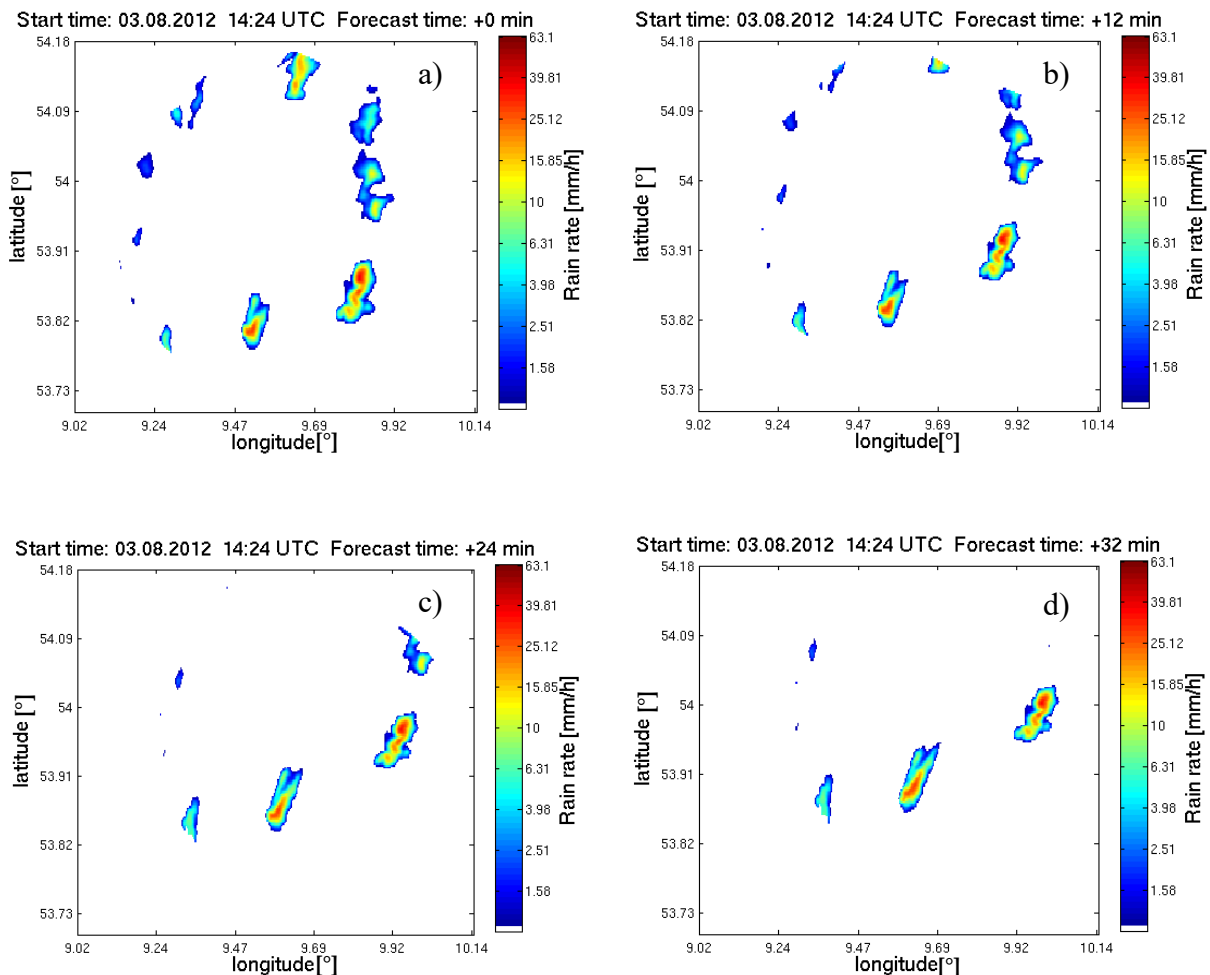


Figure 4.10: APEX forecast for the 3rd of August 2012 with COSMO data starting from 14:28 UTC with lead times a) 0 min b) 12 min c) 24 min and d) 32 min illustrating a result with low verification scores.

4 Results and Discussion

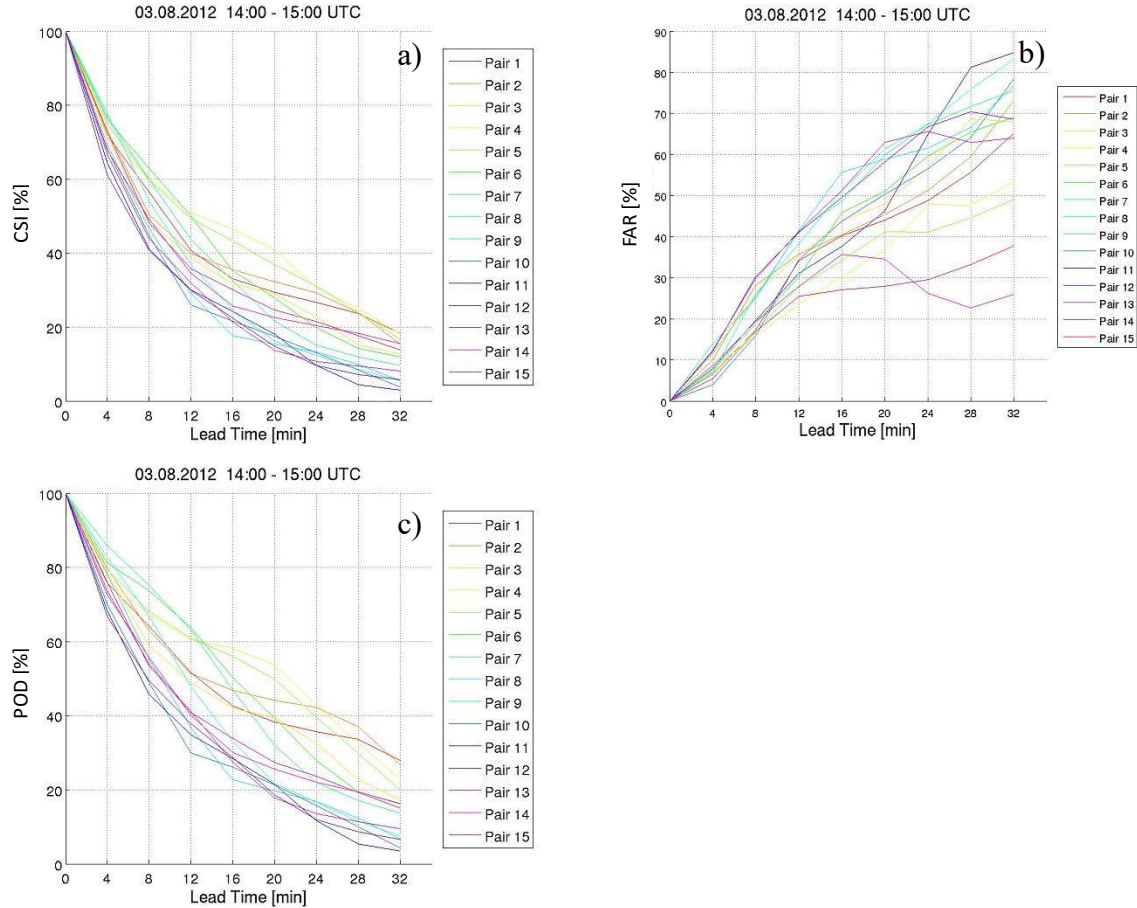


Figure 4.11: Verification scores of the APEX forecasts of the 3rd of August 2012 (COSMO data). Every line results from a pair of two consecutive rainfall fields within 14 and 15 UTC. The subimage a) shows the CSI, b) the FAR and c) the POD.

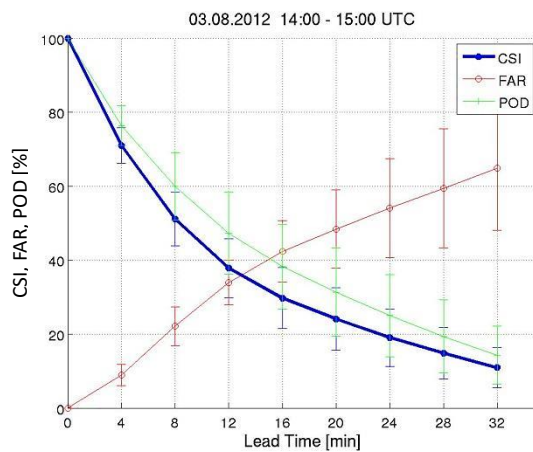


Figure 4.12: Averaged verification scores of the APEX forecast of the 3rd of August 2012 (COSMO data) over one hour from 14 to 15 UTC.

4.1.3 PATTERN versus COSMO – predictability with APEX

In this section a comparison of the prediction quality from PATTERN data and from COSMO data shall be conducted. For this, the already introduced verification scores are plotted now in a way that the COSMO scores and PATTERN scores become directly comparable. Moreover, the single scores and averaged scores are summarized in one figure. Figure 4.13 displays this e.g. for the 19th of July 2012 (06 – 07 UTC). The full dots and empty circles mark the individual CSI values. The lines indicate the averages over the whole hour. The red part of the figure results from the COSMO data whereas the blue part depicts the PATTERN output from APEX.

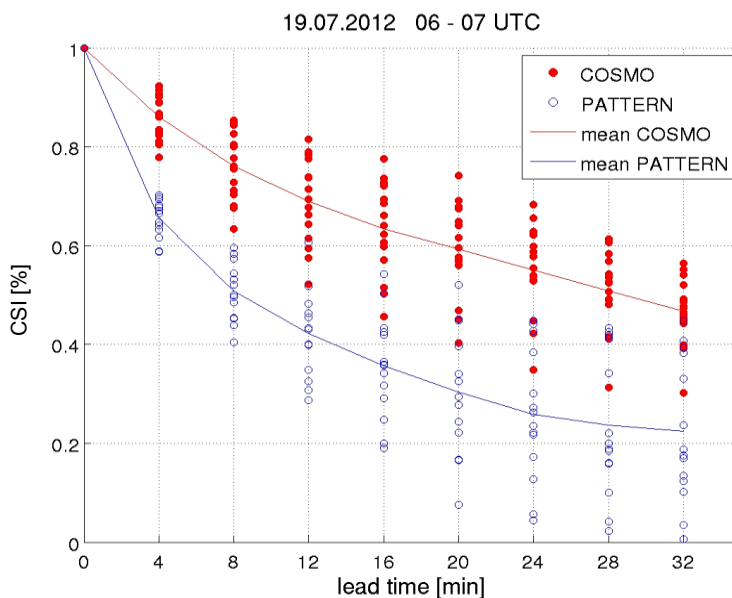


Figure 4.13: Example from the 19th of July 2012 as comparison between PATTERN and COSMO CSIs. Dots and circles mark single CSIs from every correlation pair between 06 and 07 UTC. The lines mark the averaged scores over this hour.

In this example the mean COSMO CSI score is always higher than the mean PATTERN CSI. Up to a lead time of 8 min even all single scores (meaning the scores from every correlation pair) of PATTERN lie below corresponding values of COSMO. Only after a lead time of 12 min several single scores begin to overlap. This kind of figure is useful to see whether extreme values influence the average. Furthermore, it holds information about the spread of the non-averaged values. Another illustration to compare the PATTERN and COSMO scores is depicted in Figure 4.14 for the CSIs and in Figure 4.15 for the FARs. These scatter plots unite more data into one plot and give a comprehensive survey over the whole data amount investigated in this work.

4 Results and Discussion

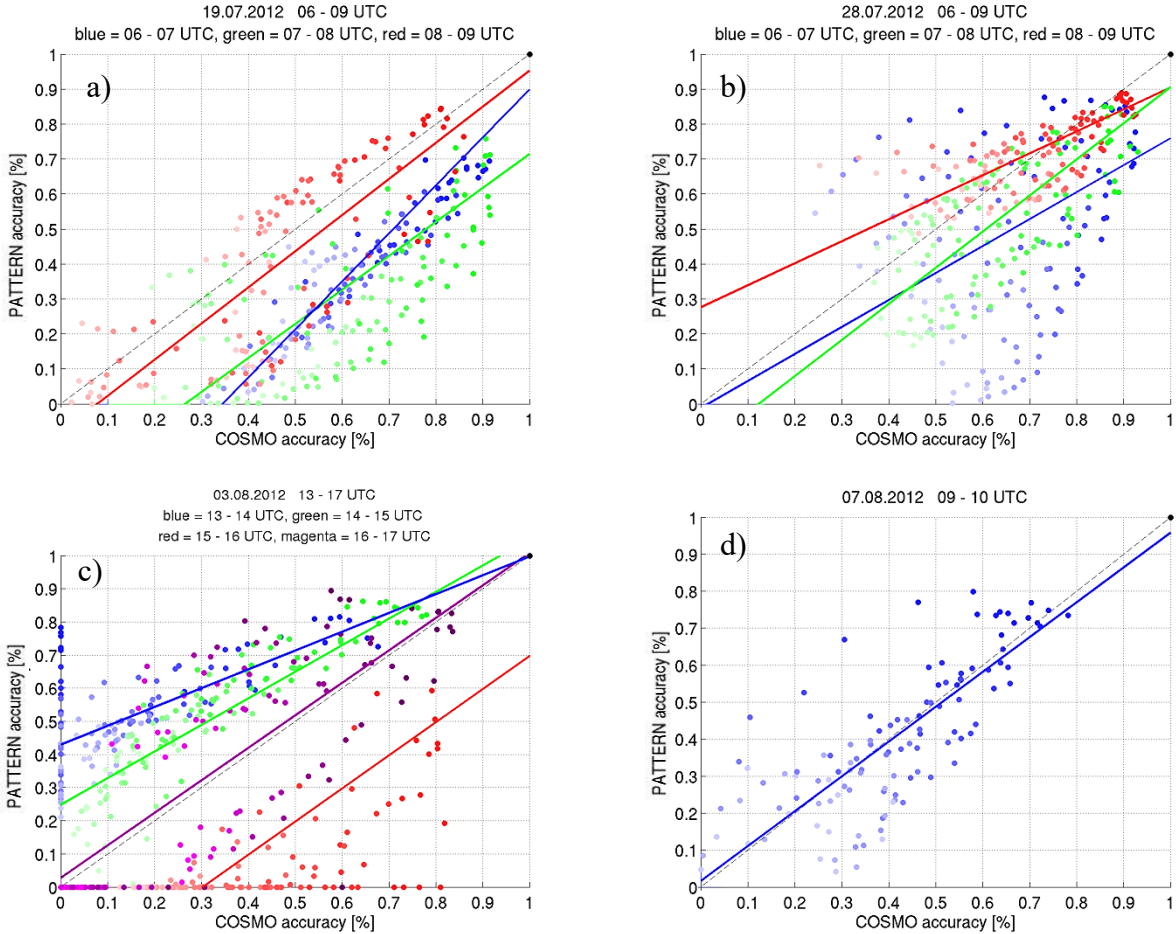


Figure 4.14: Illustration of the PATTERN CSI scores versus the COSMO CSI scores. Every subplot presents one of the four Golden Days where a) shows the 19th of July 2012, b) the 28th of July 2012, c) the 3rd of August 2012 and d) the 7th of August 2012. The black dashed lines are the equilibrium lines where PATTERN and COSMO CSIs would have the same values. The continuous black lines are the particular least square lines for every color group. The brightness of the colors hints at the lead time. Dark colors are short lead times and bright colors long lead times.

Every subplot summarizes one of the four Golden Days whereas the hours refer to a particular color. So, the example from Figure 4.13 can be found in Figure 4.14 a) with a look at the blue dots. The temporal behavior is not assigned to one of the axes anymore but it is visible by the color gradient. At the timestep zero there is no displacement of the precipitation fields. That means the forecast field (which is not really a forecast field at this timestep) matches exactly the observation field. Consequently, the CSI and POD values are one because there are no misses and no false alarms. Following from this, the FAR values are zero. This explains the black dot in the upper right corners of Figure 4.14 and in the bottom left corners of Figure 4.15. Then the colors of every hour begin to fade out with every forecast timestep. Like in Figure 4.13 it is clear to see that the CSIs decrease with increasing lead time but not in the same way for the PATTERN and COSMO simulations. Mostly the COSMO CSI scores higher than the PATTERN CSI as nearly all the blue dots from the 19th of July 2012 between 6 and 7 UTC lie below the equilibrium line. If all the dots lay exactly on this straight line, it

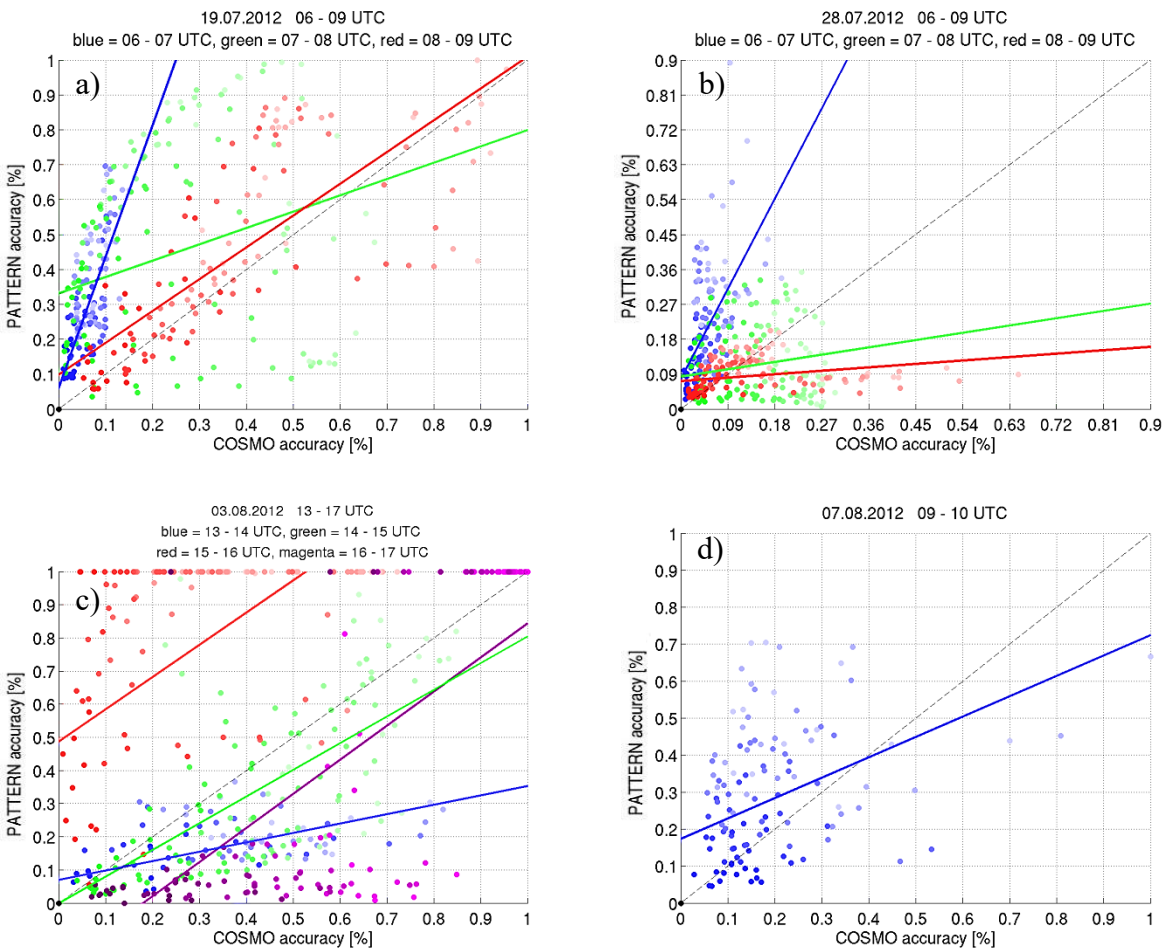


Figure 4.15: Illustration of the PATTERN FAR scores versus the COSMO FAR scores. Every subplot presents one of the four Golden Days whereas a) is from the 19th of July 2012, b) from the 28th of July 2012, c) shows the 3rd of August 2012 and d) the 07th of August 2012. The black dashed lines are the equilibrium lines where PATTERN and COSMO FARs would have the same values. The continuous black lines are the particular least square lines for every color group. The brightness of the colors hints at the lead time. Dark colors are short lead times and bright colors long lead times.

would mean that the scores from PATTERN and COSMO are the same. The FAR values increase stronger for PATTERN data which explains the lower CSIs. Also the periods from 7 to 8 UTC and from 8 to 9 UTC show a similar behavior whereas the spread of the scores is more expanded which means that there is a high variability in the PATTERN scores as well as in the COSMO scores. Nevertheless, the tendency of higher COSMO CSIs and lower COSMO FARs remains visible. Figure 4.16 can give a possible explanation by looking at the measured or rather simulated precipitation fields: The COSMO field (left image) is smoother than the PATTERN field (right image). The area is more continuous and there are less differentiated small precipitation areas. Furthermore, the precipitation coverage is higher in the simulated image. All these factors cause fewer false alarms in the COSMO forecasts and consequently a higher CSI.

Figure 4.14 b) and Figure 4.15 b) present in the same way the CSIs and FARs for the 28th of July 2012. Compared to subfigure a) there is a higher spread especially in the CSI scatter

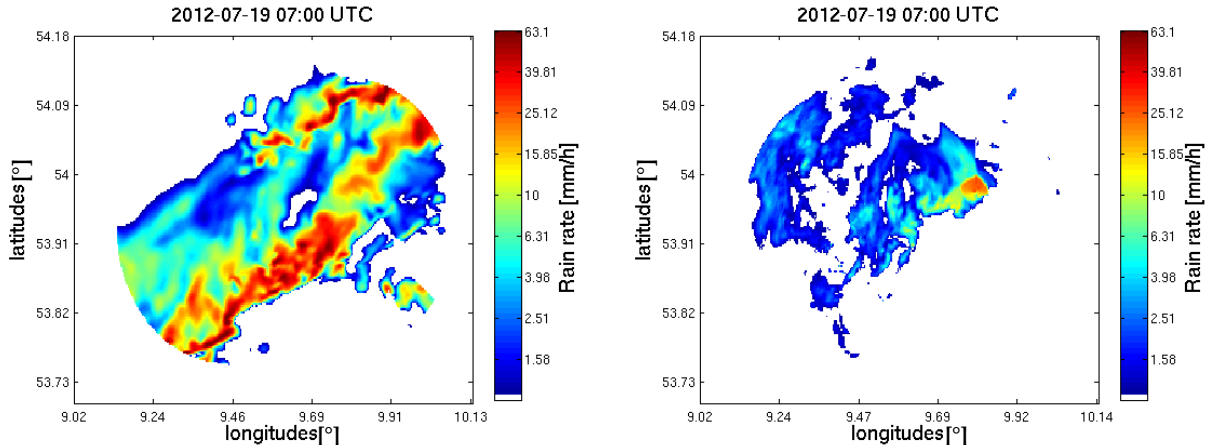


Figure 4.16: Comparison of the measured or rather simulated precipitation fields of the PATTERN radar network (right) and the COSMO simulation (left) at the 19th of July 2012, 07 UTC.

plots. Most of the dots are arranged in the right part of Figure 4.14 b), so the main part of the CSIs for COSMO is above 0.5. On the PATTERN scale only the red dots (8 – 9 UTC) are accumulated nearly completely above 0.5 whereas between 6 and 8 UTC the scores disperse over the whole scale. Moreover, also in this case most of the CSI dots lie below the dashed diagonal. So, the COSMO forecast reaches higher CSI scores than the PATTERN forecast. The FARs are very small compared to those of part a) of Figure 4.15. A look at the precipitation fields (not illustrated here) shows that also at this day the precipitation coverage is higher than 50 % mostly which explains the low FARs.

On the 3rd of August 2012 (Figure 4.14 c) and Figure 4.15 c)) the situation seems to be very different. Only between 15 and 16 UTC (red dots) the COSMO CSI scores higher than the PATTERN CSI while its FARs lie clearly over the equilibrium line. Between 15 and 17 UTC (red and magenta dots) many of the CSIs go down to zero for the PATTERN forecasts. Accordingly, the FARs at the same time rise to one. Between 13 and 14 UTC (blue dots) even some CSIs of the COSMO forecast go down to zero. The explanation can be found again in the precipitation images that are not shown here. Between 13:00 and 13:20 UTC there are only some small rain cells in the COSMO simulation that are not displaced by APEX. Consequently, the FAR rises rapidly whereas the CSI falls to zero. In the case of the PATTERN forecasts there is nearly no precipitation measured between 15:20 and 16:20 UTC. In this period the APEX forecasts are very erroneous. The few existing rainfall pixels are displaced in various directions for different correlation pairs. Therefore the scores are quite poor. Nevertheless, some correlation pairs provide good results. The PATTERN forecast scores higher than the COSMO forecast between 13 and 15 UTC. Probably this is due to the higher precipitation coverage in the measurements compared to the simulation at this time.

Part d) of Figure 4.14 and Figure 4.15 considering the 07th of August 2012 presents a case where the least square fit lies near the equilibrium line. So, the PATTERN and COSMO scores show nearly the same behavior and no tendency can be emerged.

Concentrating now on the CSI, Figure 4.17 gives a survey of all the mean CSI differences between COSMO and PATTERN. So, all positive bars (red colored) mark a higher COSMO CSI and all negative bars (blue colored) mark a lower COSMO CSI compared to the PATTERN CSI. In general, in 7 of 11 cases the COSMO CSI scores higher at all or nearly all lead times. In three cases, the PATTERN CSI scores higher than the COSMO one and in one case there is a dichotomy. Up to 16 min lead time the COSMO CSI still scores higher and from 20 min on it lies under the PATTERN CSI (Figure 4.17 f)). The maximum deviations lie between 30 % and 40 % in positive as well as in negative direction.

The 19th of July 2012 shows a nearly constant behavior for all the three hours. Only between 8 and 9 UTC (Figure 4.17 c)) the deviations are smaller because in the modelled rainfall fields the precipitation leaves the radar area and no new precipitation follows. This leads to several CSI curves that decrease much stronger than the others and consequently the differences are lower. On the 28th of July in two of the three investigated hours the COSMO CSI scores higher for all lead times, likewise. Between 8 and 9 UTC there are positive and negative

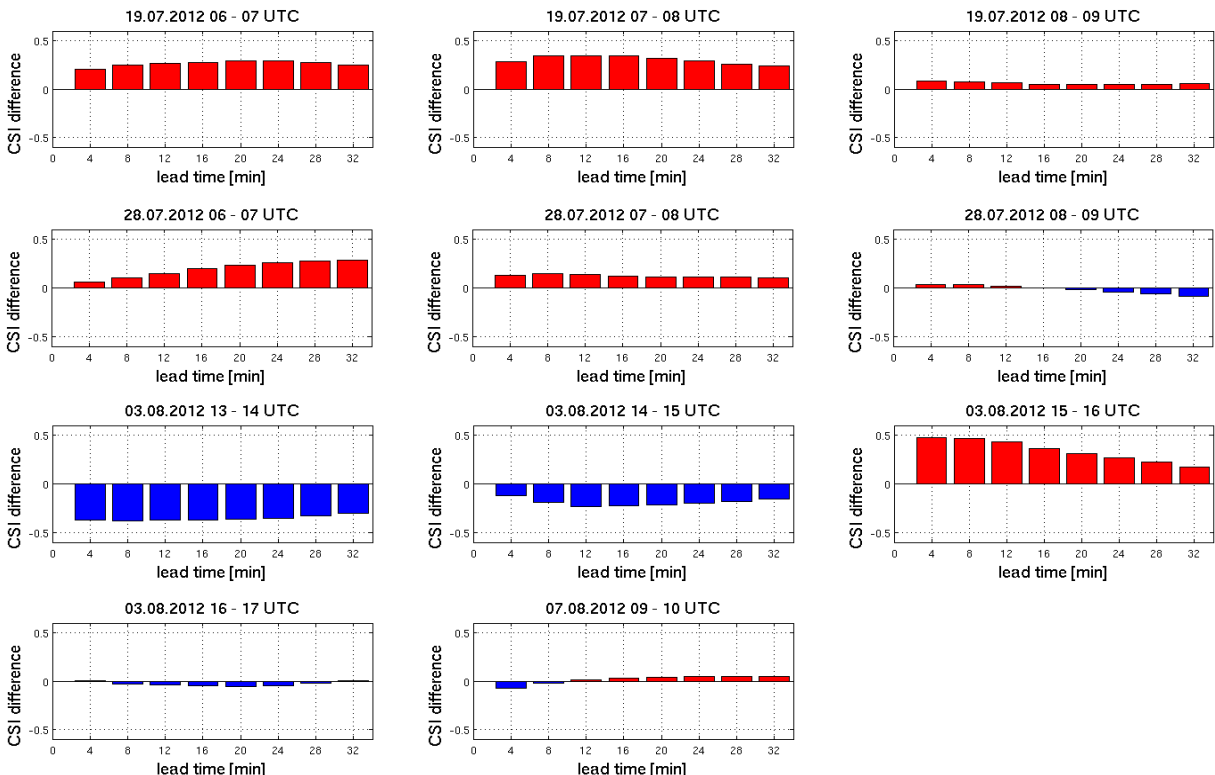


Figure 4.17: Differences between mean COSMO and mean PATTERN CSIs of all the investigated data. Every subplot shows the averaged values over one hour.

deviations with amplitudes lower than 10 %. In this hour the rainfall field of the measured data shows very high precipitation coverage, so that the mean PATTERN CSI does not fall below 60 % after a lead time of 32 min. However, in the hours before it falls to 35 % and 20 %. This extraordinary high mean CSI explains why the differences in Figure 4.17 f) are so small. On the 3rd of August, it is interesting that in the first two hours the PATTERN CSI overbalances the COSMO CSI and between 15 and 16 UTC the deviations are strongly in the opposite direction. Note that from 15.20 UTC on nearly no precipitation was measured. This hour generally provides no good quality data and the results must be ignored. From 16.15 UTC on new precipitation appears in the radar area and the differences between the mean CSIs are near zero. The strong negative deviations between 13 and 15 UTC are caused by extremely low COSMO CSIs which originate from low precipitation coverage or erroneous APEX forecasts. On the 7th of August (Figure 4.17 l)) the differences are small. In this case, also the precipitation fields look very similar.

In conclusion, these results always have to be considered with the information about the precipitation field and the APEX forecast fields. Especially on the 3rd of August the CSIs are influenced by exceptional precipitation fields or forecasts. These examples should be taken out of the evaluation. Reasonable results can be found on the 19th and 28th of July and on the 7th of August where the model mostly dominates the observation. This behavior was expected because the simulated rainfall images are smoother and without sharp edges or gaps. With the applied categorical verification such rainfall fields produce fewer false alarms and the CSI scores are consequently higher.

The interesting question is whether the APEX forecast with PATTERN data or with COSMO data has a longer lead time for the same forecast quality. For that purpose, the averaged CSIs are fitted exponentially, so they can be extrapolated to lead times longer than the calculated 32 minutes. When these CSIs reach a value of $1/e$ from the initial value the lead time is plotted in Figure 4.18. The lead times with the same forecast quality are confronted between the averaged PATTERN CSIs and the averaged COSMO CSIs for every hour. The result is heterogeneous. In 7 of 11 cases the APEX forecast with COSMO input data reaches a longer lead time than with PATTERN data. Those 7 cases are the same as already selected in Figure 4.17 where the COSMO CSI is higher than the PATTERN CSI. Thus, the reasons why there is no clear structure are very low or high precipitation covered fields or erroneous APEX forecasts as well.

Figure 4.19 depicts a bar chart with the mean precipitation coverage for every hour of the investigated data. Excluding the cases with nearly no precipitation in the simulations or in the measurements or with very high differences in the coverage between COSMO and PATTERN

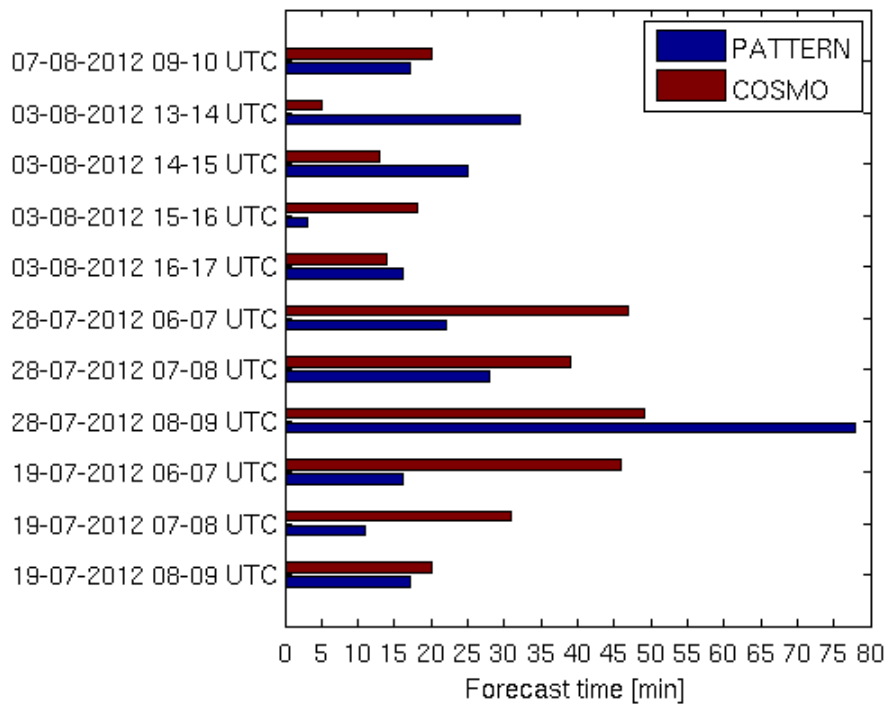


Figure 4.18: For every hour of the Golden Day's precipitation events the averaged CSI is considered and fitted exponential. Then the period after which the CSI has declined to a factor of $1/e$ is calculated.

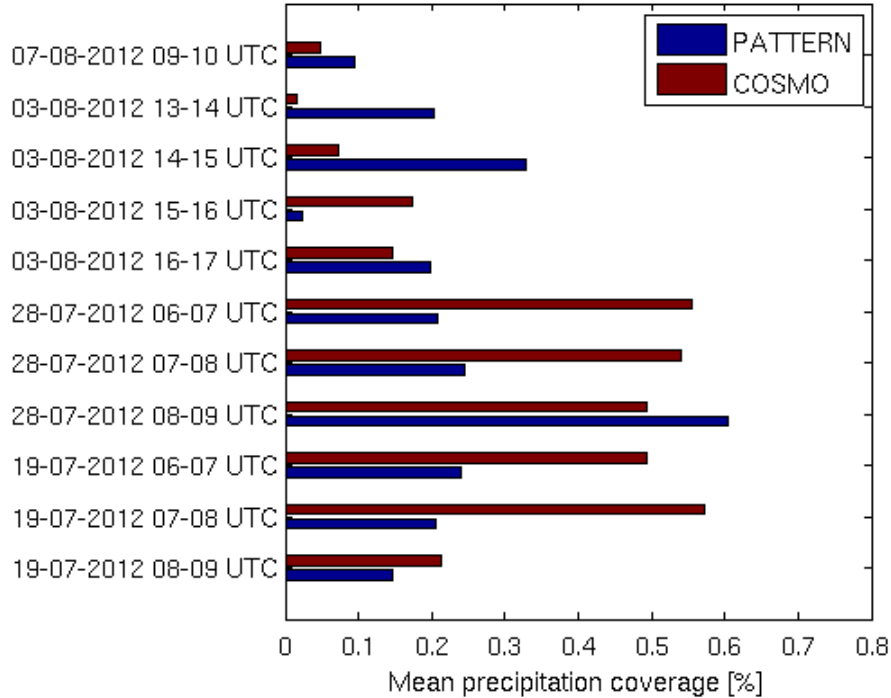


Figure 4.19: For every hour of the Golden Day's precipitation events the mean coverage of the precipitation fields is presented for the PATTERN data (blue) and the COSMO data (red).

4 Results and Discussion

(3rd of August 2012 from 13 to 16 UTC) there is a tendency that with the COSMO simulated data a longer forecast with the same forecast quality is possible. Explicitly, it means a mean lead time of 33 min for the COSMO simulations and 26 min for the PATTERN data until a decrease to the factor $1/e$. Without the PATTERN outlier on the 28th of July 2012 between 8 and 9 UTC the mean lead time even goes down to 18 min. Then the difference in the lead time between model and observation is 15 min.

In this chapter, the functionality of the APEX tool was examined with the aid of categorical verification scores. This means that the results are based only on investigations of the plain because categorical scores only decide between ‘precipitation yes’ and ‘precipitation no’. The strength of the deviation in the intensity is disregarded.

The scores show that the forecasted precipitation fields don’t match exactly the measured or COSMO simulated fields. The inaccuracy originates from two different aspects. Firstly, APEX is assumed to forecast perfectly in this thesis but in fact it doesn’t. But even with faultless APEX forecasts the CSIs wouldn’t be one because APEX does not account for the convective evolution of the rainfall fields. Indeed, a possible intensification or attenuation cannot be quantified with categorical verification scores but a convective evolution is also associated with an increasing or decreasing rainfall area. In conclusion, the results of this section show a stronger convective evolution for the measurements than for the simulations because the deviations from the truth are higher for PATTERN data (lower CSIs).

For the evaluation with continuous variables and the filtering of the convective evolution it is assumed further that APEX advects the rainfall images faultlessly. With this assumption section 4.2 analyses the strength of deviations that can be interpreted as convective evolution in the intensity.

4.2 Analysis of the convective evolution using continuous scores

The main focus of this thesis is on the separation between the advective and the convective evolution of a rainfall field that passes the radar area. The nowcasting tool APEX is used to displace the precipitation 32 minutes into the future. In this way, it provides the advection part of the rainfall field. However, in reality a precipitation field can intensify or attenuate. This part is not considered by the APEX forecasts. Based on the assumption that the forecasts are perfect the difference between a forecasted rainfall field and the original measured or simulated rainfall field at the corresponding timestep indicates the convective evolution, so the intensification or the attenuation during the timestep. This methodology is explained and plotted in section 2.1 in detail.

So far, the quality of the APEX forecasts is presented and it is compared between forecasts of modeled data by COSMO and measured data by the PATTERN radars. The evaluation scores are categorical scores that separate only between ‘precipitation yes’ and ‘precipitation no’ at a certain pixel. With this kind of evaluation the scores indicate how well the precipitation area is forecasted. As presented in the previous section the scores are strongly dependent on the precipitation coverage and the shape of the precipitation fields. Therefore, scores like the CSI or POD can look very different for specific events. Figure 4.16 shows the same precipitation event simulated by COSMO and measured by the four PATTERN radars, respectively. Although the two images match in time and in space they look quite different. A direct comparison as in section 4.1 is only reasonable looking at the forecast quality of APEX but in this section there are two things different. Firstly, continuous variables (BIAS and RMSE) are used instead of categorical scores. They do not only provide a ‘yes/no – analysis’ but rather quantify the difference of the two rainfall fields via point-to-point matching. Secondly, the evaluation does not aim for the forecast quality but to a similar behavior of the forecast errors. E.g. usually a forecast is good when the RMSE between model and observation is small. But here the ‘model world’ and ‘observation world’ are separated strictly and the RMSEs are calculated between the APEX forecasts and the simulated or measured rainfall field. The result is good when the RMSEs are equal or in other words when the difference between the RMSEs is near zero.

The guiding of this chapter consider the variability and strength of deviations from the APEX forecast fields. These deviations are interpreted as convective evolution. The point of interest is the verification of the convective evolution between the model simulations and the observation data of PATTERN.

4 Results and Discussion

To get the rain rate differences and with it the dynamical part of the precipitation development the APEX forecast fields are subtracted from the observed or simulated rainfall field depending on whether the input data for APEX are from COSMO or from PATTERN. Because this produces a large amount of data and difference fields only examples are presented. A particularly good and strong convective evolution is visible in the COSMO simulation from the 3rd of August 2012 between 16 UTC and 16.30 UTC.

Figure 4.20 shows the original simulation by COSMO (a) c), e)) and the dynamical part (b), d), f)). In this example, there is a growth of the rainfall cell. As APEX only calculates the part of the precipitation that is caused by advection the positive deviations are overbalanced on the right side of Figure 4.20. Furthermore, the meaning of the term advection always contains a spatial displacement. However the subtracted APEX values must be interpreted as the part of the rainfall field that is caused by advection. The subtraction from the original fields at the according timestep would produce an image of the convective evolution that is moving anyway. To avoid misunderstandings the forecast fields and the according observation fields are displaced back by the global displacement vector and then the differences are calculated as they can be seen in Figure 4.20. Therefore, the axis labels do not contain longitudes and latitudes anymore but only grid points.

This example shows that the method for filtering the convective evolution of a rainfall image works well and it gives a hint at the magnitude of the deviations. However, not all cases offer such clear cell dynamics. In a large part of examples the deviations are in a range of +/- 20 mm/h and the fields of rain rate differences show stained patterns.

Generally, it should be remarked that on the LES scale and in the range of the X-band radars there is little strong convective evolution. The precipitation that occurs at a certain location predominantly comes from advection of rainy clouds. This poses the question how much of the convective evolution is visible at all or in other words: how strong are the deviations from zero in the rain rate difference fields as shown in Figure 4.20? A simple histogram of the rain rate differences can give a first view on this topic. Figure 4.21 depicts an example from the 3rd of August 2012 with PATTERN forecasts. The rain rate differences are summed over every lead time between 13 and 14 UTC on this day. Most of the differences are close to zero so that the ordinate is cut at a value of 25000. Otherwise, the shape of the histogram wouldn't be visible as it is in Figure 4.21. With increasing lead time the deviations seem to become stronger. The effect is not very distinctive but the tendency exists also at other times for PATTERN forecasts as well as for COSMO forecasts. Like in this example the histograms become wider in both directions. On the one hand this could be induced by the growth or decay of rainy clouds, on the other hand it could hint at forecast inaccuracies from the displacement by APEX that are more and more dominant with increasing lead time

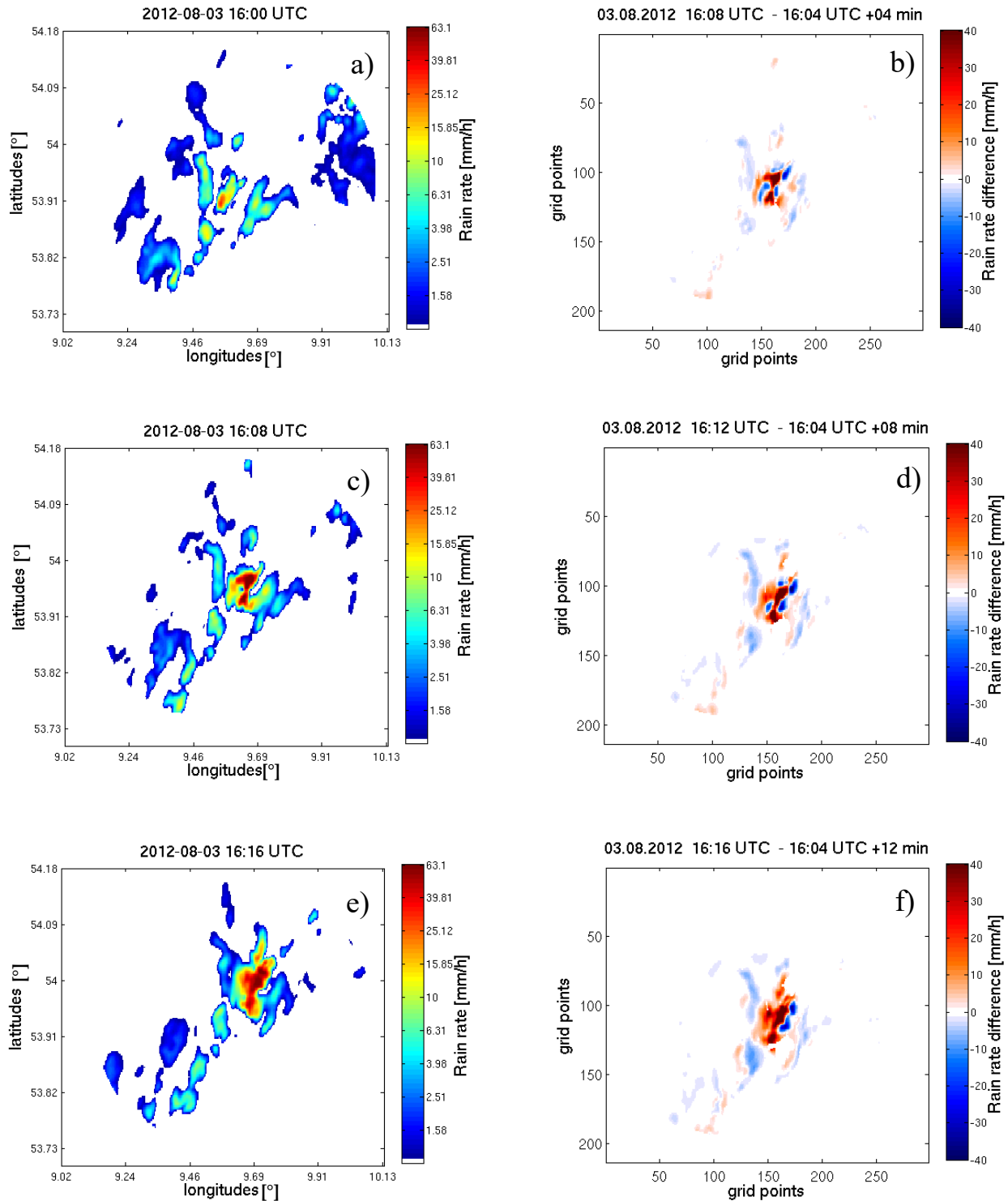


Figure 4.20: Illustration of a positive cell dynamic. The parts a) – c) show the development of a precipitation field from the 3rd of August 2012 simulated by COSMO. The parts d) – f) show only the convective evolution. The advection is subtracted. A small range around zero (about +/- 1 mm) has no color and is not visible in the figure parts b), d) and f).

4 Results and Discussion

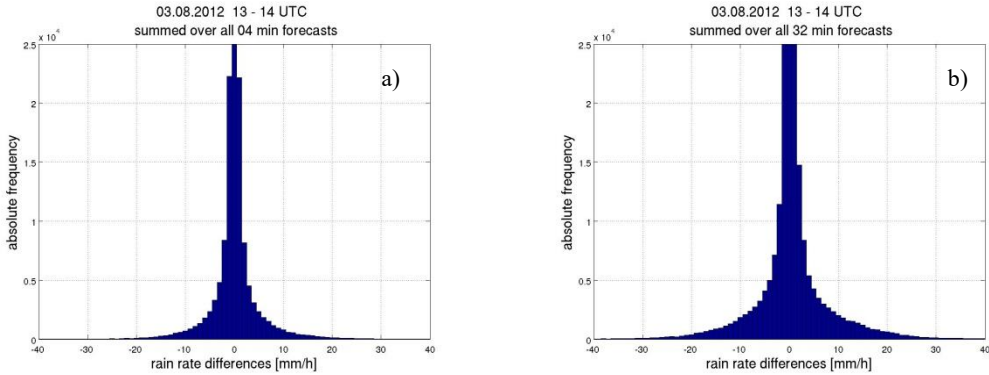


Figure 4.21: Survey of rain rate differences from the 3rd of August 2012 (PATTERN data) between 13 and 14 UTC. Every subplot presents the hourly sums per lead time, a) for the 4 min - forecasts and b) for the 32 min – forecasts.

and affect the positive and negative deviations likewise. A wrong spatial displacement of a rainfall front could provoke strong indications for convection even though no inner development takes place. This question is addressed in Chapter 4.3. The distributions of rain rate differences for the simulated data look very similar to this example. They are therefore not shown here. Differences are only due to particular precipitation events but there is no significant difference between the PATTERN and the COSMO histograms.

Because of the insufficient representation in the histograms the pie charts from Figure 4.22 show the exact percentages of the deviations in the denoted ranges. Here, only the summations over the 4 min – forecasts (a) and b)) and the 32 min – forecasts (c) and d)) are selected to compare the situation at the beginning and at the end of the forecast. First of all, it becomes clear now that the deviations that represent the convective evolution are few compared to all the small deviations around zero. In Figure 4.22 a) the fraction in a range of ± 1 mm (yellow colored) adds up to 92 %. In the summation of the 32 min – forecasts (Figure 4.22 c)) this fraction is reduced to 83 %. This reflects the widening of the histograms and the peak around zero (Figure 4.21). The fractions that represent the deviations greater than 2 mm contain only 3 % for positive deviations (dark-red) and 2 % for negative deviations (dark-blue) for the 4 – min forecasts or rather 7 % for positive deviations and 6 % for negative deviations for the 32 – min forecasts. These values represent a typical magnitude for all the other examples that are not presented here. A threshold that decides between convection or not isn't determined. So, all the deviations are counted as convection. Like in the histograms, the increase of stronger deviations with increasing lead time is visible in the pie charts. In Figure 4.22 b) and d) two changes are done. The limits between the fractions are modified and the sector from -1 mm to 1 mm is removed. So, only positive and negative deviations are confronted and divided by the colors blue and red. In the most cases these two parts are approximately equalized like in the example. The fractions of the strongest deviations (greater than ± 10 mm) are with 5 % and 6 % (Figure 4.22 b)) or 9 % and 12 % (Figure 4.22 d)) the

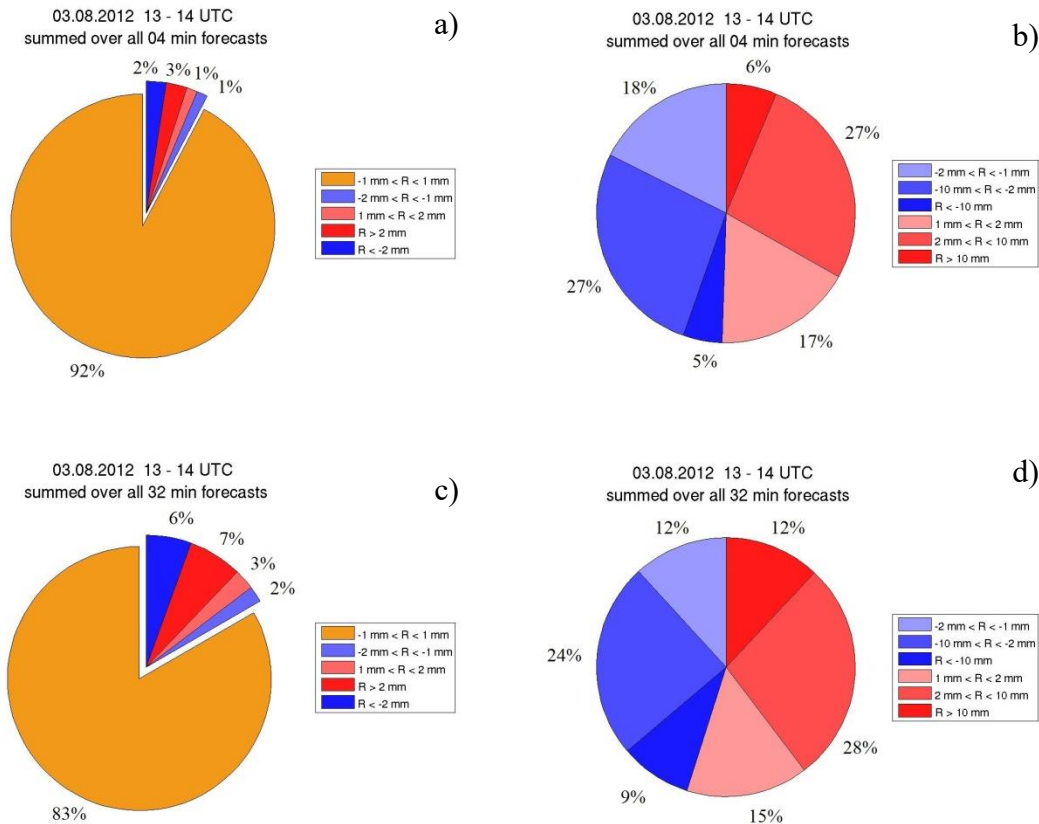


Figure 4.22: Convective evolution for the 3rd of August 2012 between 13 and 14 UTC (PATTERN data) illustrated in pie charts to get an idea about the strength of deviations and their frequencies. The first row presents the summed values over all 4 min forecasts, the second row them of all 32 min forecasts. On the left side, the pie charts contain the values around zero whereas on the right side only the values greater than 1 mm and lower than -1 mm are shown to contrast positive (red) and negative (blue) deviations.

smallest parts. With the assumption of a perfect APEX forecast this behavior proves the existence of convective evolution in the observations and simulations that is not present in the APEX forecasts. E.g. a growing rainfall cell induces lower deviations for a 4 min – forecast than for a 32 min – forecast because the cell has less time to develop.

For the quantification of the convective evolution the RMSE is used. Due to the second power of this score it is very sensitive to large forecast errors. This is harmful if there are outliers in the datasets but it weights more the stronger deviations that are rare in many of the investigated cases as can be seen in Figure 4.22. What is called “error” in the RMSE term is not an error in this case but the convective evolution. This is only possible with the assumption of perfect APEX forecasts. The RMSE is not built between modeled data and observed data directly because it would evaluate the forecast. However, the aim in this work is to evaluate the behaviour of the convective evolution in the model world and in the

4 Results and Discussion

observation world. In Figure 4.23 the RMSEs are plotted for the PATTERN forecasts as well as for the COSMO forecasts. Every red dot (COSMO) or blue circle (PATTERN) represents the RMSE of one cell dynamic image for the according lead time. The lines are the mean values of the dots/circles. The focus is on the comparison of them or in other words on the RMSE differences. With this method the simulated convective evolution of COSMO can be verified on the basis of measurements from PATTERN. However, the RMSE quantifies both the positive and negative convective evolutions. So, if the COSMO RMSE (red colored) is greater than the PATTERN RMSE (blue colored) the model will calculate a stronger convective evolution than the observation regardless of whether the development is positive or negative.

On the 19th of July 2012 (Figure 4.23 a) – c)) the mean COSMO RMSE is significantly greater than the mean PATTERN RMSE between 6 and 8 UTC. Only between 8 and 9 UTC it has values in the same magnitude as the PATTERN RMSE because there is less and weaker precipitation in the simulated field. Therefore, also the deviations are not too strong.

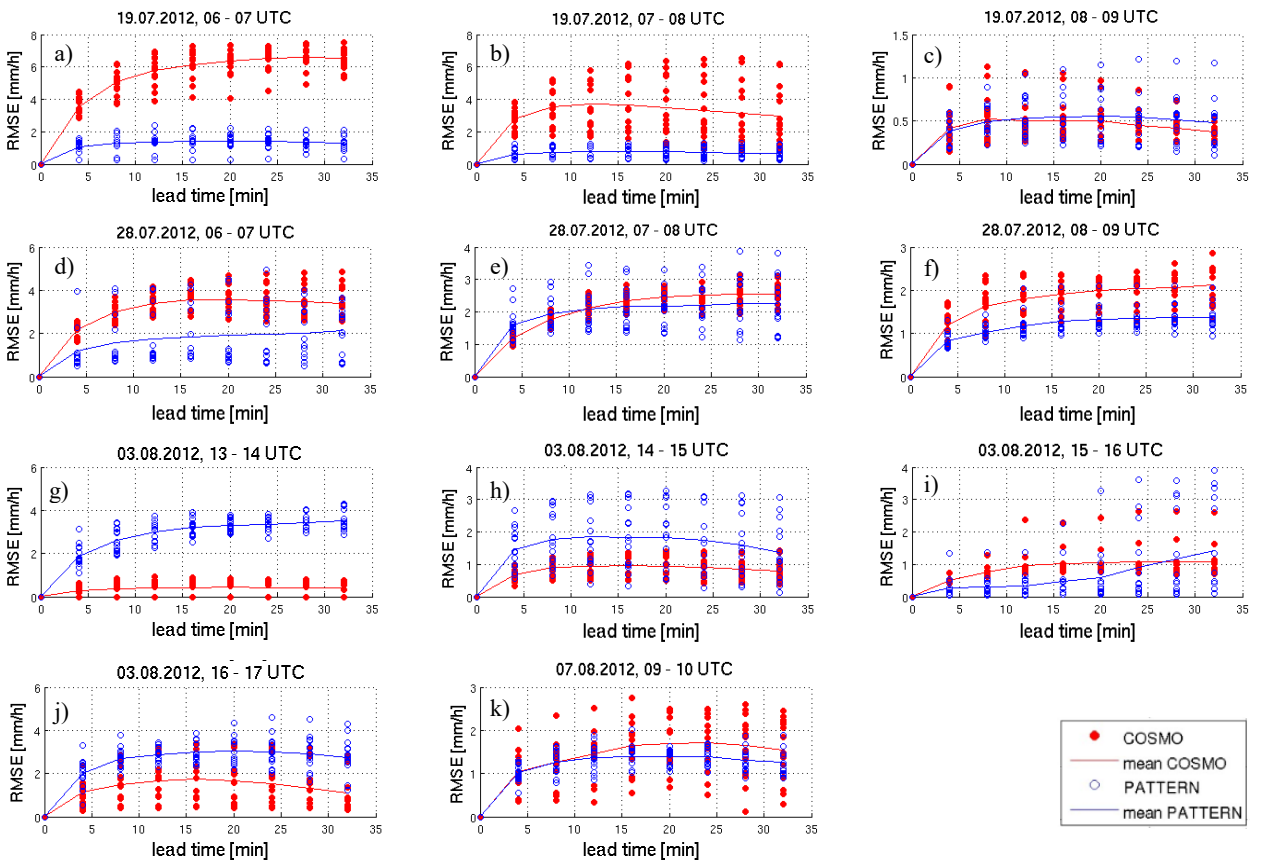


Figure 4.23: RMSE for every hour of the investigated data amount as comparison between the convective evolution of model simulated precipitation and the measured precipitation. The red (COSMO) and blue (PATTERN) dots over the lead times belong to each correlation pair within the denoted hour. The lines are the averages of the dots per lead time.

On the 28th of July 2012 (Figure 4.23 d) – f)) again the the COSMO RMSE mostly is greater than the PATTERN RMSE but the spread is smaller. This is probably because the precipitation coverage as well as the magnitudes are closer together than in the example from the 19th of July. The blue circles in Figure 4.23 c), d) and e) show that sometimes outliers influence the mean RMSE of the PATTERN datasets.

On the 3rd of August 2012, the results are not meaningful. As already mentioned the precipitation coverage in the COSMO fields between 13 and 15 UTC and in the PATTERN field between 15 and 16 UTC are very small and sometimes there are incorrect APEX forecasts. Therefore, the Figure 4.23 g) to i) should not be assessed. Only between 16 and 17 UTC the images are acceptable. Here, the mean PATTERN RMSE lies significantly over the COSMO RMSE.

In the example from the 7th of August 2012 the precipitation images are similar concerning the coverage and magnitudes. Also the mean RMSEs are not very different.

With respect to the mentioned exceptions the RMSE shows that the convective evolution of the modeled data in most cases seem to be stronger than by nature. A great influence on the comparability is given by the magnitudes of the simulated rain rates. If the maximum rain rates are small also the resulting convective evolution will be small. Another factor is the precipitation coverage. In extreme cases there is nearly no precipitation in the simulated field whereas the radars measured a much higher precipitation coverage at that time. These examples should not be consulted for the verification of the convective evolution. Figure 4.24 depicts the RMSE normed with the precipitation coverage to elimite the dependency of it. In the parts a), b), g) and j) of the figure the mean curves become closer. This proves the influence of the precipitation coverage on the RMSE in Figure 4.23. The comparison of these examples with the mean precipitation coverages per hour in Figure 4.19 confirms the approach of the mean RMSE curves: The curves with the lower RMSEs accord to the precipitation fields with the lower coverage. The standardization compensates this issue. In some examples (like in part d) of the figure) the maximum normed RMSEs reach extraordinary high values that are caused only by single dots or circles. This is due to precipitation images with nearly no rainfall. In the most cases, the dominance of one of both – the PATTERN RMSEs or the COSMO RMSEs – remains. However, Figure 4.24 h) is an example where the COSMO RMSE is greater than the PATTERN one after the scaling with the precipitation coverage. In contrast to Figure 4.23 h) the intensity of the convective evolution is stronger for the COSMO simulations in the denoted hour. The main results of Figure 4.23 and the statements about the convective evolution do not change much after the standardization but some details become clearer now.

4 Results and Discussion

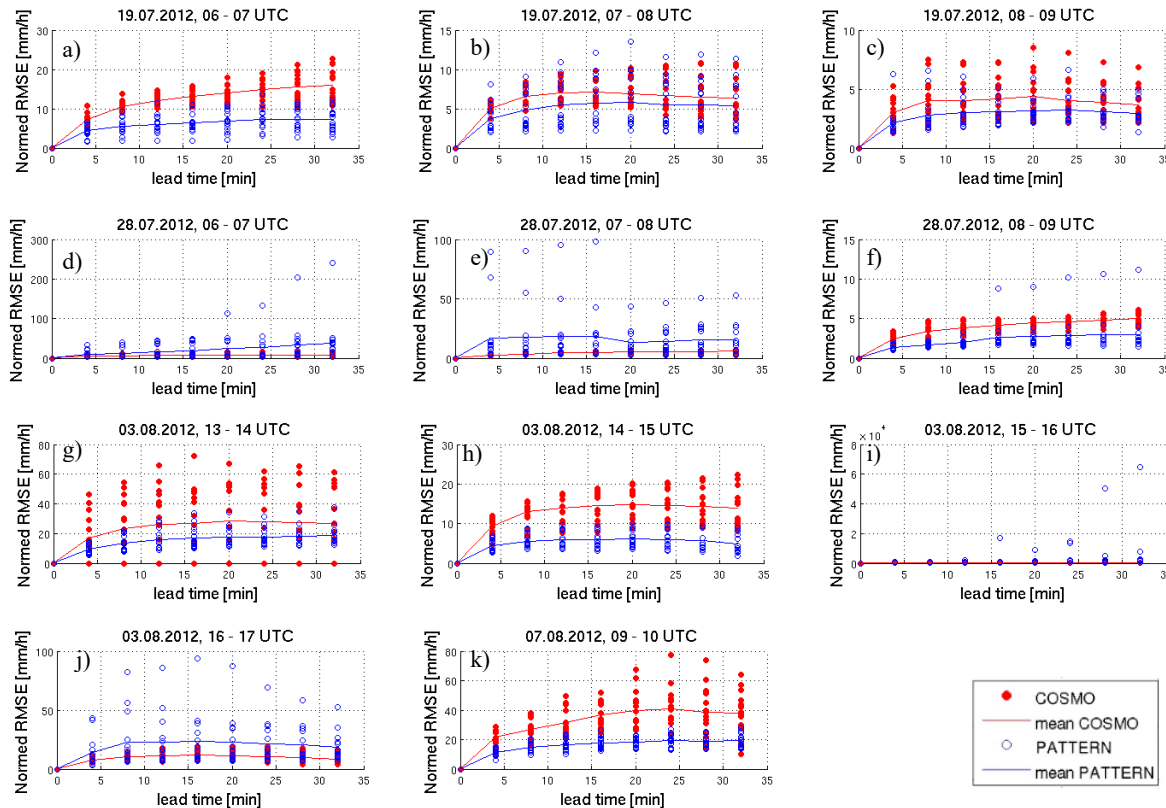


Figure 4.24: RMSE normed with the precipitation coverage for every hour of the investigated data amount as comparison between the convective evolution of model simulated precipitation and the measured precipitation. The red (COSMO) and blue (PATTERN) dots over the lead times belong to each correlation pair within the denoted hour. The lines are the averages of the dots per lead time.

In the next step, the BIAS is considered for estimating positive or negative deviations. With it the question can be answered whether the convective evolution is overestimated or underestimated by COSMO. A BIAS greater than zero means that the forecast field is overforecasted. Consequently, the simulation or the measurement has a negative convective evolution. Otherwise, the BIAS is negative which indicates that the convective evolution is positive.

As the BIAS is calculated as an average over the whole data field an unbiased field doesn't mean compulsory that there is no forecast error. It is possible that positive and negative deviations cancel each other out. Therefore, it is important to consider the BIAS always together with a score like the MAE or the RMSE.

Figure 4.25 presents the BIAS for the Golden Days separated hourly. Here, the COSMO BIAS (red) and the PATTERN BIAS (blue) are compared directly to get the information about an overestimation or underestimation of the convective evolution by COSMO. Similar to Figure 4.23 for the RMSE comparison the dots and circles are calculated from a single cell dynamic image in the denoted hour for the according lead time. The lines build the averages

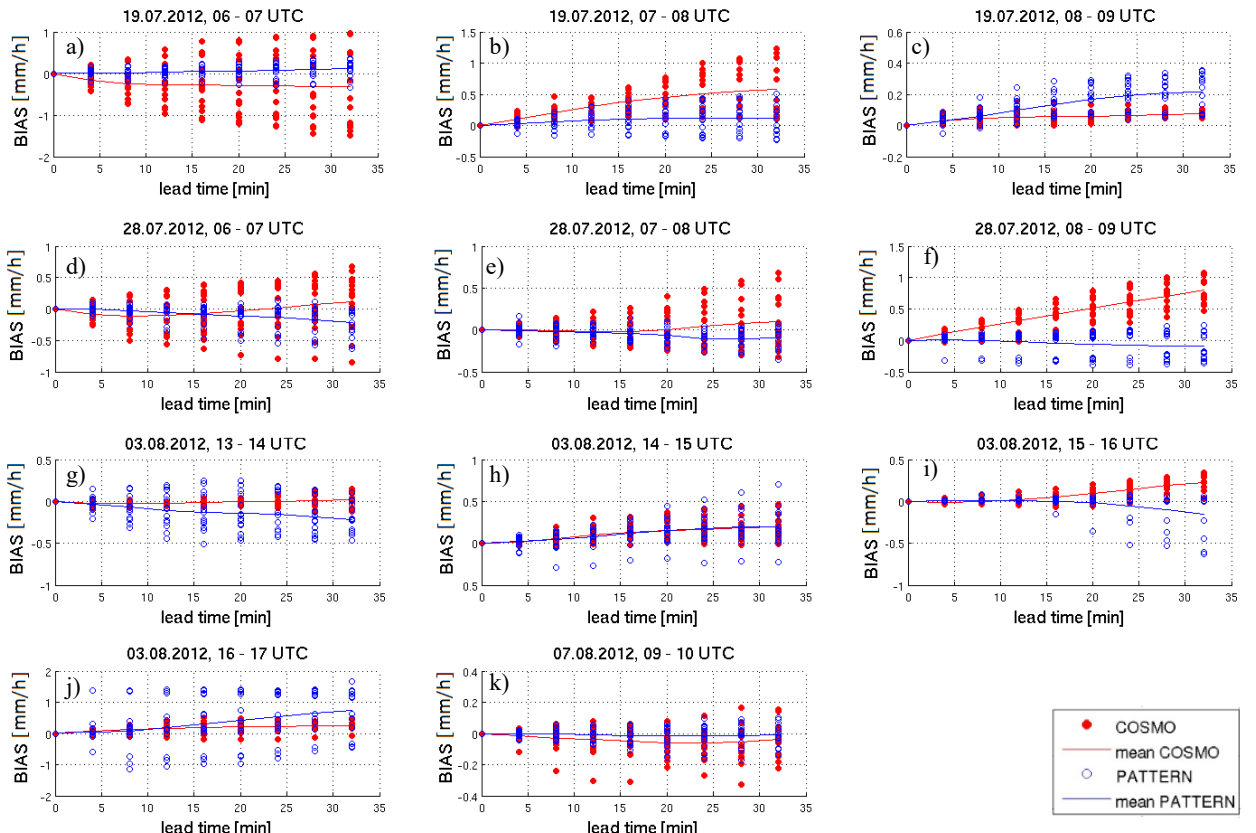


Figure 4.25: BIAS for every hour of the investigated data amount as comparison between the convective evolution of model simulated precipitation and the measured precipitation. The red (COSMO) and blue (PATTERN) dots over the lead times belong to each correlation pair within the denoted hour. The lines are the averages of the dots per lead time.

of all the dots or circles at that lead time. Figure 4.25 reveals that there is no BIAS greater than 2 mm/h or lower than -2 mm/h. So, there is no very strong convective evolution only in one direction. Many of the rain rate difference images (not shown here) confirm visually by their blurry patterns that positive and negative deviations mostly hold the balance. The mean COSMO BIAS mostly lies above zero which means that APEX forecast fields are overforecasted in the intensity. The mean PATTERN BIAS goes in the positive direction just as often as in negative direction. The deviations from zero are weak. Sometimes one curve is more in the positive sector whereas the other is in the negative sector. For example in Figure 4.25 f) the modeled rainfall field seems to attenuate between 8 and 9 UTC although the measurements show a slightly positive convective evolution.

A continuous overestimation of the convective evolution (positive and negative direction) by the model would be visible by absolute COSMO BIAS values greater than the absolute PATTERN BIAS values. Looking more at the dots and circles instead of the mean values (lines) this is actually observable: The maximum absolute deviations from zero mostly are

marked by a red dot. In all these cases also the COSMO RMSE (Figure 4.23) is greater than the PATTERN RMSE. In the other cases the PATTERN RMSE dominates.

A clear structure of overestimation or underestimation of the convective evolution cannot be found in the low number of examples investigated here. The mentioned examples with the very low precipitation coverage (3rd of August 2012, 13 – 16 UTC) should not be considered for drawing conclusions. The other plots exhibit very small BIAS values. There is a slight tendency for an overestimation of the convective evolution by COSMO but the signals are very small. In summary, the model seems to simulate qualitatively well the convective evolution. Otherwise, the BIAS values would be in another magnitude.

Of course, the assumption that the APEX forecasts are perfect is not correct. The investigation and verification of the convective evolution in this work is probably more influenced by forecast errors instead of an incorrect representation of the convective evolution by COSMO. Section 4.1 shows that the APEX forecasts are limited in the forecast quality. Consequently, the images of the convective evolution and all the following results are faulty. Therefore, in the next section 4.3 this and other errors that influence the results are collated.

4.3 Error sources and uncertainties

The data used for this work are not perfect and therefore several sources of error exist. Likewise, the verification method brings some uncertainties into the results. The errors can be categorized into three parts: the errors in the simulated data, the errors in the observation data and the forecast errors by APEX.

First of all, the model outputs from COSMO are not free from different kinds of internal model uncertainties that are caused for example in numerical errors or parameterizations. In this work, the investigated data are chosen in a way that the dates and times exactly match between model world and observation world. However, a quick look on the precipitation images reveals that the model data are often afflicted with a time lag or with a spatial offset. In extreme cases this can lead to the situation that there is no simulated precipitation at the time when the radar measurements show signals because e.g. a frontal passage is too early with no following precipitation or it is too late with no precedent precipitation. A temporal and spatial correction of the simulated rainfall fields could improve or make clearer the results of this work. A further source of error is the nesting method that is used by Beuchel (2015) to

nest down the model domain two times from 2.8 km to 1 km and again to 250 m. Moreover, the model outputs always exist on a curvilinear grid. The adaptation on a cartesian grid demands a choice between multiple values that are near the target grid point. This error is negligible but it modifies the simulated precipitation field a little bit.

The second source of errors is in the observation data. Radar measurements always contain noise, clutter and a certain measurement uncertainty. The raw data are filtered several times to get a good quality image. Besides, a radar measures on a polar grid because it is a rotatable construction. In addition, the radar area that gives the data base for this work is a composite from four precipitation radars. The processing of the raw data to the composite form is already done by Lengfeld et al. (2013). Although the measurement data are already processed there are still some peaks in the precipitation fields that are not visible on the first view but during the analysis of the convective evolution with the RMSEs this peaks cause obvious outliers. Figure 4.26 compares the RMSEs on the 28th of July 2012. On the one hand the available composite input data that are processed by Lengfeld et al. (2013) and Lengfeld et al. (2014) are plotted. On the other hand an additional filter is implemented. In the original data field single pixels, very difficult to see by eye, have enormously high precipitation rates of more than 1000 mm/h. They produce peaks in the RMSE plots that are 6 times higher than the usual RMSE values. The filter has the function to eliminate these pixels by excluding all values greater than 100 mm/h. This threshold can be chosen arbitrary but the lower it is the more data can be lost that are correct. After application of the filter the peaks are still visible but their magnitude is reduced to less than two times the usual RMSE values (Figure 4.26 b)). So, the mean RMSE is not influenced strongly anymore.

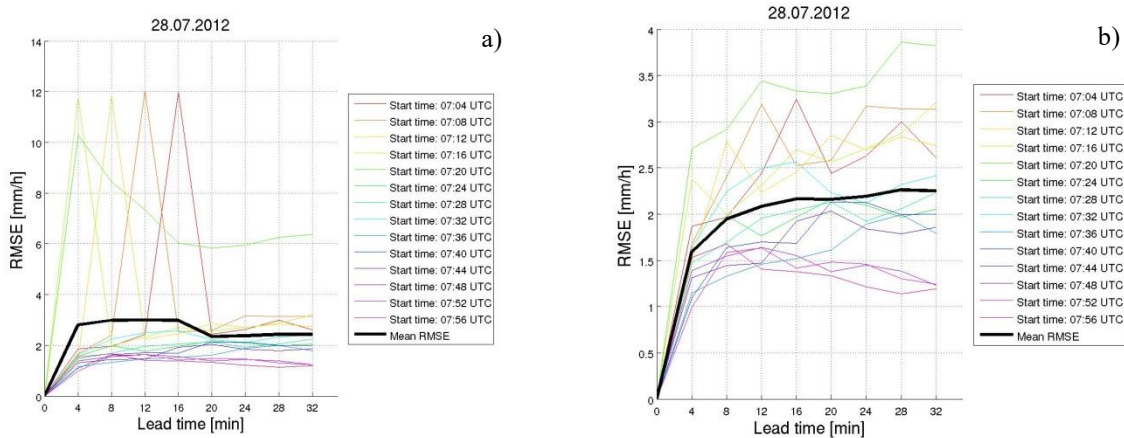


Figure 4.26: Comparison of the RMSEs from the 28th of July 2012 with a) original observation data and b) filtered observation data.

Finally, the instrument for the precipitation displacement APEX is a further source of error. For this work, it is the assumption that this nowcasting tool works perfectly. However, different categorical verification scores show that the real precipitation movement is never matched exactly. A variety of input parameters presented in Chapter 2.4 have influence on the quality of the precipitation forecast of APEX or on the verification scores of these forecasts. E.g. the threshold that determines whether a pixel counts as precipitation or not is very variable and has a great influence on the number of false alarms. Furthermore, a different temporal increment between the two input images and between the forecast timesteps can change the accuracy of the prediction. Many different settings were tested in this work but even with the perfect APEX settings the forecast would never be perfect. That is why the convective evolution quantified in this work always contains an error caused by the imprecise displacement of the precipitation fields and consequently an incorrect advective fraction of precipitation at a certain location. The quantification of this error is not part of this work but a simple thought experiment can give an idea about its possible magnitude: A precipitation front of only several hundred meters width will cross the measurement area of the weather radars. Supposed that APEX displaces the precipitation front several hundred meters too far then in the image of the convective evolution there will be a band with strong positive development and directly aside a band with strong negative development. The dimension of the error in this case will be in the magnitude of the rainfall intensity within the front. In such a case it could even dominate the deviations by the convective evolution.

Figure 4.27 proves that examples like in the thought experiment actually exist. In the panels a) and b) of the figure a thin rainfall band measured by the PATTERN X-band radars moves towards northeast. Part c) is the difference between observation and forecast that should represent the convective evolution. However, in this example the rainfall band is obviously not displaced far enough. Therefore, in the area where the front is actually located a strong positive development is indicated. In the area where the front is displaced by APEX, a strong negative deviation is indicated because in the observation field there is only weak precipitation. Consequently, the error calculated from this image is mainly based on a wrong forecast instead of real convection. Fortunately, the number of such cases seems to be rather low but it is not quantified in this work because errors like this are not always as clear as in the example above. The identification and elimination of such erroneous displacements would be a further task. This issue is addressed in Chapter 5.

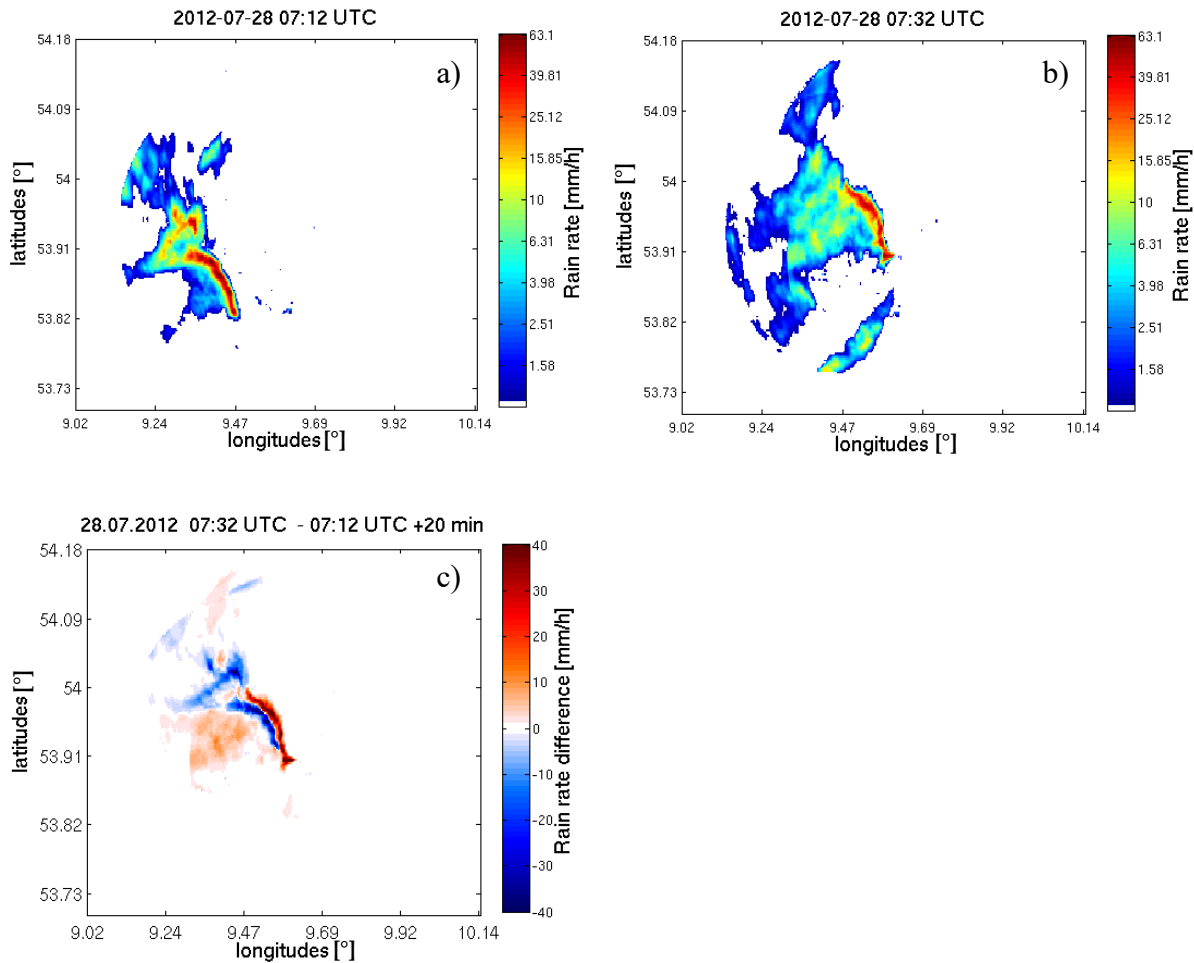


Figure 4.27: Example from PATTERN observation data with a thin high intensity rainfall band at the 28th of July 2012 between 7 and 8 UTC. The parts a) and b) of the figure show the measured event at two different times. Part c) of the figure is the difference between the observation field at 7:32 UTC and the 20 min – forecast starting from 7:12 UTC.

5 Conclusion and Outlook

In this thesis simulated precipitation fields from COSMO as well as measured precipitation fields from PATTERN are split into their advective part and the part that is induced by convective evolution to verify the latter. For the division a powerful nowcasting tool, called APEX, is used to calculate precipitation forecasts in 4 min – timesteps up to a maximum lead time of 32 min. These forecast fields are determined by the correlation of two consecutive existing precipitation fields and contain only the advective part of the precipitation as APEX does not include cell growth or decay. By subtraction from the original rainfall fields the convective evolution remains, a perfect APEX forecast assumed. Original fields in this context mean on the one hand the measured precipitation fields from the four PATTERN X-band radars in the area of Itzehohe and on the other hand the simulated fields by COSMO. For both, the observation data and the model data the APEX forecasts are calculated and evaluated separately. Whereas a classical verification would compare a simulated field with a measured field directly this methodology makes no sense in this work. Firstly, the images of model and observation look quite different on the LES scale. The model data used here are nested down from 2.8 km to 250 m, so small scale phenomena are not depicted accurately. This fact is not an obstacle because with the methodology used in this work only the behavior of the precipitation is investigated. Secondly, with a direct comparison the separation between advection and convective evolution would not be possible. The investigated period is restricted to the Golden Days in the year 2012 that are characterized by simultaneous occurrence of precipitation at all four X-band radars. Precipitation is a highly fluctuating quantity and its prediction is not trivial. The investigation and verification of the convective development as it is depicted in weather prediction models is an important component especially on the LES scale. Severe weather like heavy rain mostly appears very short-term and locally restricted. In sectors like traffic and aviation or for flash flood warnings by the media the meteorological models has to be as exact as possible.

The results of this work can be divided into two parts. The first part deals with the application of the APEX tool on observation data as well as on simulation data and their evaluation. For both, the forecasts with PATTERN data and the forecasts with COSMO data there are examples for good displacements of the rainfall fields and examples with erroneous displacements. Although APEX was adapted and tuned to the existing circumstances (e.g. adaptation of the grid resolution and the timestep, determination of different thresholds, tuning of some filters or other parameters, smoothing of the calculated wind field, etc.) there

are still some few cases that produce very low verification scores. Often these cases contain an extreme low precipitation coverage with single small rainfall cells. They are responsible for a high false alarm rate. Beside the subjective analysis of the rainfall images and their displacement the categorical verification scores CSI, FAR and POD provide an opportunity for the objective analysis. In good cases the mean CSI of one hour lies around 60 % accuracy for a 32 min – forecast. The non – averaged CSI values also go up to 90 %. So, for single correlation pairs there are only few misses and false alarms. In bad cases it can be decreased to nearly zero after a 32 min – forecast.

A comparison of all the investigated CSI values from the COSMO forecasts and the PATTERN forecasts shows that mostly the COSMO forecasts score higher than the PATTERN forecasts. The cases with nearly no precipitation coverage need to be disregarded to get this result more clearly. Still on the basis of the CSI an extrapolation of the CSI curves to lead times higher than 32 min gives the answer whether the COSMO forecasts or the PATTERN forecast reach a longer lead time with the same forecast quality. With the available data and under consideration of some exceptional cases the difference between the lead times after a decrease to a factor of $1/e$ amounts 15 min in favor of COSMO. This was expected as the modeled data are typically smoother than measured data. It means that there are less sharp edges or precipitation areas of only few pixels that would produce more false alarms and consequently lower CSI scores. Moreover, with the assumption of perfect APEX forecasts this result shows that the convective evolution (considered only in the spatial extension) is lower in model than in the observations.

The second part of the results deals with analysis and verification of the convective evolution (considered in the intensity) that is extracted with the help of APEX from the total precipitation. Instead of categorical scores that only decide between ‘precipitation yes’ or ‘precipitation no’ continuous variables like the RMSE and the BIAS are used here to quantify the convective evolution. The first perception by looking at the fields of convective evolution and the according histograms is that the most part of the deviations from zero is near zero or in other words, the convective evolution is weak in the investigated data. About 90 % of the precipitation classified as convective evolution is between – 1 mm/h and + 1 mm/h when the values of one hour summed over all 4 min – forecasts are considered. This fraction could be derived from deviations by chance. The fraction of convective evolution with absolute values greater than 2 mm/h is typically about 5 %. This value arises to the double or triple in the most cases when the summations of all the 32 min – forecasts within one hour are considered. The increasing of stronger deviations from the APEX forecast with increasing lead time is comprehensible. A cell growth or decay proceeds further after 32 min than after 4 min starting from the initial fields. In fact, the assumption of perfect APEX forecast is not correct and the

stronger deviations with increasing lead time also could be due to greater forecast errors with increasing lead time.

The quantitative evaluation of the convective evolution and the comparison between model and observation happens with help of the RMSE. With respect to some exceptions (the fields with very low precipitation coverage) the results show a stronger convective evolution for the ‘model world’ than for the observed data because the COSMO RMSEs mostly are greater. Thereby, it is not defined whether the evolution is positive or negative because of the square in the RMSE term. For the quantification of overestimations or underestimations of the convective evolution by COSMO the BIAS is used in the next step. It shows only weak signals which indicates positive and negative deviations in the fields of convective evolution mostly are balanced. The maximum signals originate from the COSMO BIAS in most cases which means a slight tendency for an overestimation of the convective evolution in positive as well as in negative direction by COSMO. However, the amount of the investigated data is very limited and a clear structure is not visible. This fact leads to the assumption that the model behavior of the convective evolution matches quite well the behavior in reality.

In conclusion, only considering the categorical scores the model shows a better performance (15 min higher lead time) with the same forecast quality than in the forecasts with PATTERN data. Following from this, its simulated convective evolution seems to be weaker than in the observations. Comparing the deviations in the intensity representing the convective evolution the model shows a slight overestimation but the deviations are very small and there is no clear structure recognizable. Altogether the model seems to match the natural convective evolution quite well.

Additionally, a compilation of errors that occur in the whole process shows that the results could be more clearly after the removal or improvement of some error sources. First of all, the amount of data used in this work is very small. For getting representative results it would be recommendable to investigate more data. However, this would increase the computing time enormously. A reduction of the CPU time would be advantageous. A second point is the data quality of the PATTERN X-band radars. Although the data are already processed there are some peaks sometimes not visible by eye. Applying scores like the RMSE immediately strong outliers are visible because of the quadrature.

A further error source that should not be underestimated is the APEX tool that is used for extracting the advective part of the total precipitation. An example is shown where slightly erroneous displacements could form convective evolutions that do not exist in fact. Such cases make the whole interpretation of results difficult.

For the operational application of the method used in this thesis there are two possibilities for

its improvement: the tuning of APEX or the filtering of its outputs. An idea for the filtering could be to let the forecast field wiggle around its target position and then to minimize the forecast error. This way, the correct position of the forecast field after the specific timestep could be better found. Another approach could be to implement a procedure that recognizes spatial patterns like a frontal passage. With the help of additional data (pressure gradient, temperature field, etc.) the velocity of such synoptic phenomena could be better estimated. Moreover, the wind is a highly fluctuation quantity in its velocity as well as in its direction. Strong deviations of the wind direction between two consecutive input fields of the APEX algorithm has to be identified to avoid wrong displacements. Often a low precipitation coverage was the problem to investigate and compare the data adequately. This leads to the question how much precipitation is necessary to classify a rainfall image as qualitatively good. The investigation of the dependency of the results on the precipitation coverage could be an interesting topic. A kind of quality index for APEX that contains such examples as provided above could indicate and remove all the cases that are not evaluable.

Moreover, the same procedure could be done with another nowcasting tool and then the results can be compared. Indeed every precipitation tracker and extrapolator has its own intricacies and so it is not always possible to compare the results under the same conditions.

Further improvement could be done with an additional visualization tool. In Chapter 4 the convective development is plotted in two dimensions. An interesting new perspective would be opened by a 3D - bar chart of the precipitation field where on every pixel a pillar of two sections indicates the fraction of advective rainfall and convective development. With this kind of figure the forecasted fields by APEX and the difference to the original data fields would be visible within one plot. It could also provide information about wrong forecast fields for example when a negative convective evolution is greater than the advective rainfall at a certain pixel. The pillar would be negative. This unrealistic case would expose errors immediately.

In this work, only the deterministic approach is considered. After Rossa et al. (2008) probabilistic QPF is an alternative approach that can be applied on high resolution rainfall predictions. An example for this is Mittermaier (2007). The imprecise initial conditions and the variation of parameters in parameterization schemes build the base for the probabilistic QPF (Rossa et al., 2008). For global models ensemble forecasting with different initial conditions is already daily routine. In high resolution models and in nowcasting this method becomes more and more popular. According to Rossa et al. (2008) even the radar community is interested in it and uses the error characteristics of radar measurements to produce probabilistic QPEs. Here, Germann et al. (2006) is a popular example.

List of Abbreviations and Symbols

LES	Large-eddy simulation
BMBF	Bundesministerium für Bildung und Forschung
HDCP ²	High Definition Clouds and Precipitation for Climate Prediction
ICON	Icosahedral non-hydrostatic
MI	Meteorologisches Institut
MPI	Max Planck Institut
MPI-M	Max Planck Institut für Meteorologie
DWD	Deutscher Wetterdienst
PATTERN	Precipitation and Attenuation Estimates from a High Resolution Weather Radar Network
COSMO	Consortium for Small-scale Modeling
APEX	Automated Precipitation Extrapolator
NWP	Numerical weather prediction
TREC	Tracking of Radar Echo with Correlation
COTREC	Continuity of TREC
GDST	Growth and Decay Storm Tracker
LAC	Local area correlation
CMS	Correlation meta surface
QPF	Quantitative precipitation forecast
QPE	Quantitative precipitation estimate
DQPF	Deterministic quantitative precipitation forecast
ME	Mean error
MSE	Mean square error
RMSE	Root mean square error
SS	Skill score
FBI	Frequency Bias
POD	Probability of Detection
FAR	False alarm ratio
CSI	Critical success index
TS	Threat score
F	False alarm rate
ETS	Equitable threat score
BS	Brier score
BSS	Brier skill score

List of Abbreviations and Symbols

RPS	Rank probability score
ECMWF	European Centre for Medium-Range Weather Forecasts
DFG	German Science Foundation
HHG	Geomatikum Hamburg
BKM	Bekmünde
QNS	Quarnstedt
HWT	Hungriger Wolf
MOD	Moordorf
HRWR	High Resolution Weather Radar
MRR	Micro rain radar
RG	Rain gauge
LM	Lokalmodell
GME	Globalmodell Europa
CCLM	COSMO Climate Limited-area Model
ART	Aerosols and Reactive Trace gases
CPU	Central Processing Unit
FILTER_ROWS	APEX input parameter
FILTER_COLS	APEX input parameter
MAX_SHIFT	APEX input parameter
CORR_BOXSIZE	APEX input parameter
X_RES	APEX input parameter
Y_RES	APEX input parameter
TIME_SPACING	APEX input parameter
ANGLE_TOL	APEX input parameter
RAIN_THRESH	APEX input parameter
WX_MIN	APEX input parameter
RANGE	APEX input parameter
SIGMA	APEX input parameter
Z_THRESH	APEX input parameter
SPEED_LIMIT	APEX input parameter
SEARCH_RADIUS	APEX input parameter

Ψ_F	forecasted rainfall field
Ψ_I	initial rainfall field
t	time
τ	forecast timestep
x_I	coordinate of the initial rainfall field
y_I	coordinate of the initial rainfall field
x_F	coordinate of the forecast rainfall field
y_F	coordinate of the forecast rainfall field
u	velocity component from west to east
v	velocity component from north to south
γ	lag cross correlation coefficient
S	sub-image
x	horizontal coordinate
y	horizontal coordinate
i	lag from x
j	lag from y

References

- Baldauf, M., J. Förstner, S. Klink, T. Reinhardt, C. Schraff, A. Seifert and K. Stephan (2011): Kurze Beschreibung des Lokal-Modells Kürzefrist COSMO-DE (LMK) und seiner Datenbanken auf dem Datenserver des DWD.** Technical report, Deutscher Wetterdienst, Frankfurter Straße 135, 63067 Offenbach.
- Beuchel, Svenja, 2015:** *Virtual Radar Laboratory: A Sensitivity Study of a Radar Forward Operator*, Master's Thesis
- Brooks, H. E., Kay, M. hart, J.A., 1998:** *Objective limits on forecasting skill of rare events*. 19th Conferences Severe Local Storms. American Meteorological Society: Minneapolis, MN; 552-555
- Casati, B. Ross, G., Stephenson, D.B., 2004:** *A new intensity-scale approach for the verification of spatial precipitation forecasts*. Meteorological Applications, **11**, 141-154.
- Davis, C., Brown, B., Bullock, R., 2006:** *Object-based verification of precipitation forecasts. Part I: methods and application to mesoscale rain areas*. Monthly Weather Review, **134**, 1772-1784
- Ebert, E., McBride, J.L., 2000:** *Verification of precipitation in weather systems: determination of systematic errors*. Journal of Hydrology, **239**, 809-819
- Ebert, Elizabeth, 2008:** *Fuzzy verification of high-resolution gridded forecasts: a review and proposed framework*, Meteorological Applications, **15**, 51-64
- Feiertag, N., Clemens, M., Münster, H., Ament, F (2011):** *High Resolution Precipitation Observation with Overlapping X-Band Radars*, http://pattern.zmaw.de/fileadmin/user_upload/pattern/Documents/SAB_Nov2011_poster.pdf, accessed: 12th March 2015
- Germann, U., Zawadzki, I., 2004:** *Scale dependence of the predictability of precipitation from continental radar images. Part II: probability forecasts*. Journal of Applied Meteorology, **43**, 74-89.

- Germann, U., Berenguer, M., Sempere-Torres, D., Salvadè, G., 2006:** *Ensemble radar precipitation estimation – a new topic on the radar horizon*, Proceedings 4th European Conference on Radar in Meteorology and Hydrology, **18-22**, Barcelona, Spain
- Jolliffe, I.T., Stephenson, D.B., 2003:** *Forecast verification. A practitioner's guide in atmospheric science*. Wiley and Sons Ltd, **pp 240**
- Lengfeld, K., Clemens, M., Feiertag, N., Ament, F., 2012:** *PATTERN. Precipitation and Attenuation Estimates from a High Resolution Weather Radar Network: Design of the Experiment*, ERAD Seventh European Conference on Radar Meteorology and Hydrology (ERAD), Toulouse, France
- Lengfeld, K., Clemens, M. Münster, H., Ament, F., 2013:** *PATTERN: Advantages of High-Resolution Weather Radar Networks*, Proceedings of AMS 36th Conference on Radar Meteorology, Breckenridge, CO, USA
- Lengfeld, K., Clemens, M. Münster, H., Ament, F., 2014:** *Performance of high-resolution X-band weather radar networks – the PATTERN example*, *Atmos. Meas. Tech.*, **7**, 4151-4166
- Li, L., W. Schmid, J. Joss, 1995:** *Nowcasting of motion and growth of precipitation with radar over a complex orography*, *Journal of Applied Meteorology*, **34**, 1286-1300
- Marzban, C., Sandgathe, S., 2006:** *Cluster analysis for verification of precipitation forecast for local convective storms*, *Atmospheric Research*, **83**, 221-224
- Mittermaier, M.P., 2007:** *Improving short-range high-resolution model precipitation forecast skill using time-lagged ensembles*. *Q. J. Roy. Meteor. Soc.*, **133**, 1-19
- Nurmi, P., 2003:** *Recommendations on the verification of local weather forecasts*. ECMWF Tech. Memo 430:18.t http://old.ecmwf.int/publications/library/ecpublications/_pdf/tm/401-500/tm430.pdf, accessed: 21th August 2015
- Pierce Clive, Seed Alan, Ballard Sue, Simonin David and Li Zihong, 2012:** *Nowcasting, Doppler Radar Observations – Weather Radar, Wind Profiler, Ionospheric Radar, and Other Advanced Applications*, Dr. Joan Bech (Ed.), ISBN: 978-953-51-0496-4, InTech, Available from: <http://www.intechopen.com/books/doppler-radar-observations-weather-radar-wind-profiler-ionospheric-radar-and-other-advanced-applications/nowcasting>
- Rinehart, R. E., E. T. Garvey, 1978:** *Three-dimensional storm motion detection by conventional weather radar*, *Nature*, **279**, 287-289

Roberts, N. M., Lean, H. W., 2008: *Scale-selective verification of rainfall accumulations from high-resolution forecasts of convective events.* Monthly Weather Review, **136**, 78-97.

Rossa, Andrea, Nurmi, Pertti, Ebert, Elizabeth, 2008: *Overview of methods for the verification of quantitative precipitation forecasts,* Precipitation: Advances in Measurements, Estimation and Precipitation, **16**, 417-450

Ruzunski, Evan, 2010: *NOWCASTING FOR A HIGH-RESOLUTION WEATHER RADAR NETWORK,* Diss., Colorado State University

Schättler, G., U. Doms and C. Schraff, 2013: *A Description of the Nonhydrostatic Regional COSMO-Model.* Technical report, Consortium for Small-Scale Modelling. Part VII: User's Guide.

Segawa, T., Honda, Y., 2007: *The verification of high-resolution precipitation forecasts of the operational JMA mesoscale model.* In 3rd International Verification Methods Workshop, Reading, 31 January – 2 February 2007.

Schulzweida, Uwe, 2015: *CDO User's Guide, Climate Data Operators Version 1.6.9*

Van Horne, M.P, 2003: *Short-Term Precipitation Nowcasting for Composite Radar Rainfall Fields,* Master's Thesis

Wilks, D.S., 2006: *Statistical methods in the atmospheric sciences. An introduction,* 2nd edn. Academic Press, San Diego, pp 627

Wolfson, M. M., B. E. Forman, R. G. Hallowell, M. P. Moore, 1999: *The growth and decay storm tracker,* Eighth Conference on Aviation, Range and Aerospace Meteorology. American Meteorological Society.

Wünsch, Daniel, 2013: *Analyse von Niederschlagsereignissen im Raum Itzehohe anhand synoptischer Strukturen.* Bachelor thesis.

Zepeda-Arce, J., Foufoula-Georgiou, E., Drogemeier, K. K., 2000: *Space-time rainfall organization and its role in validating quantitative precipitation forecasts.* Journal of Geophysical Research, **105**(D8):10, 129-10,146.

[1] http://www.eumetcal.org/resources/ukmeteocal/verification/www/english/msg/ver_categ_forec/uos2/uos2_ko1.htm, accessed: 6th August 2015

[2] http://www.eumetcal.org/resources/ukmeteocal/verification/www/english/msg/ver_categ_forec/uos2/uos2_ko1.htm, accessed: 21th August 2015

[3] http://www.eumetcal.org/intralibrary/open_virtual_file_path/i2055n15861t/english/msg/ver_categ_forec/uos2/uos2_ko2.htm, accessed: 21th August 2015

[4] http://www.eumetcal.org/intralibrary/open_virtual_file_path/i2055n15861t/english/msg/ver_categ_forec/uos2/uos2_ko3.htm, accessed: 21th August 2015

[5] <http://pattern.zmaw.de/Startseite.1839+M599243d419b.0.html>, accessed: 11th March 2015

Appendix

A. Survey of the measured precipitation events

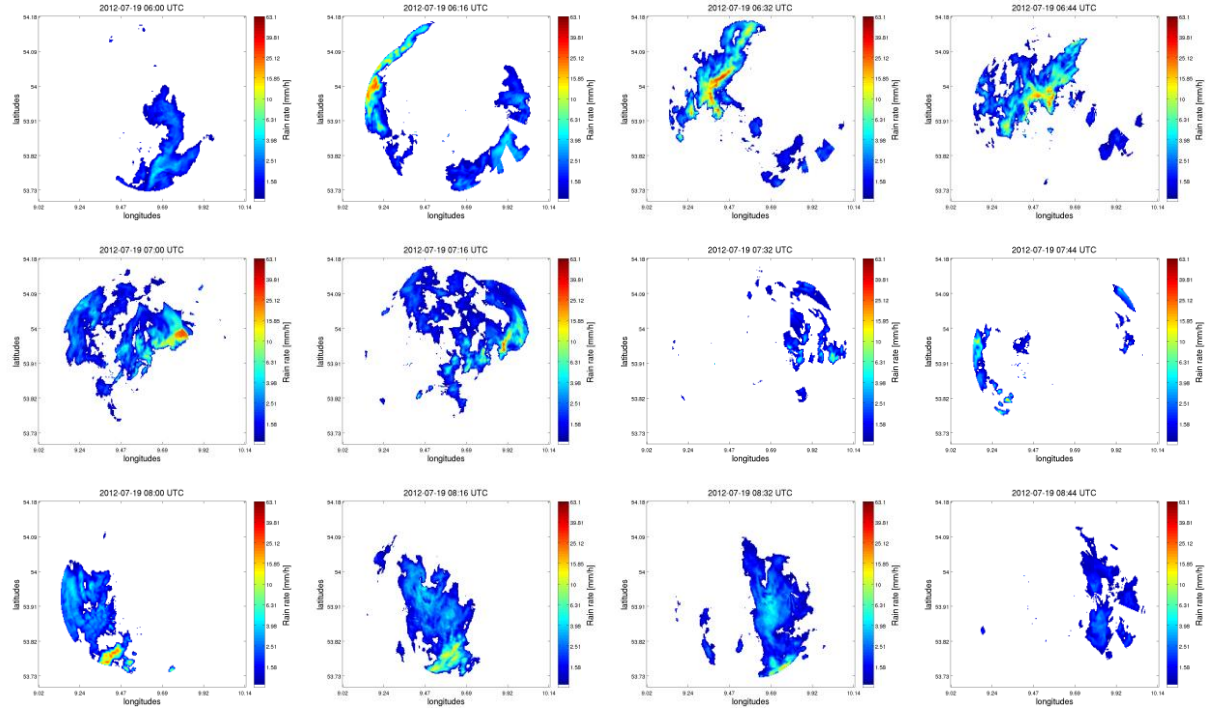


Figure A.1: PATTERN measurements from 2012/07/19, 08 – 09 UTC.

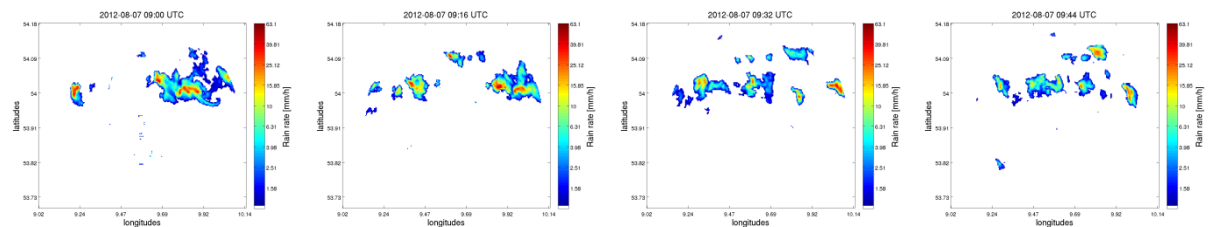


Figure A.2: PATTERN measurements from 2012/08/07, 09 – 10 UTC.

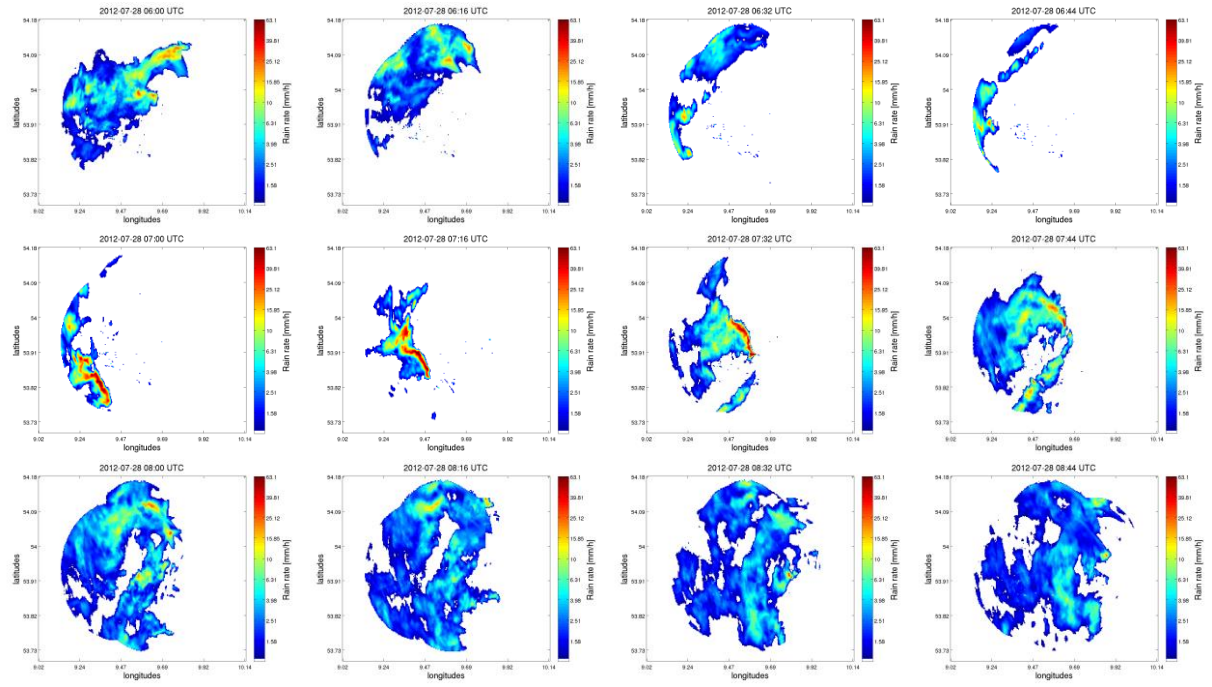


Figure A.3: PATTERN measurements from 2012/07/28, 08 – 09 UTC.

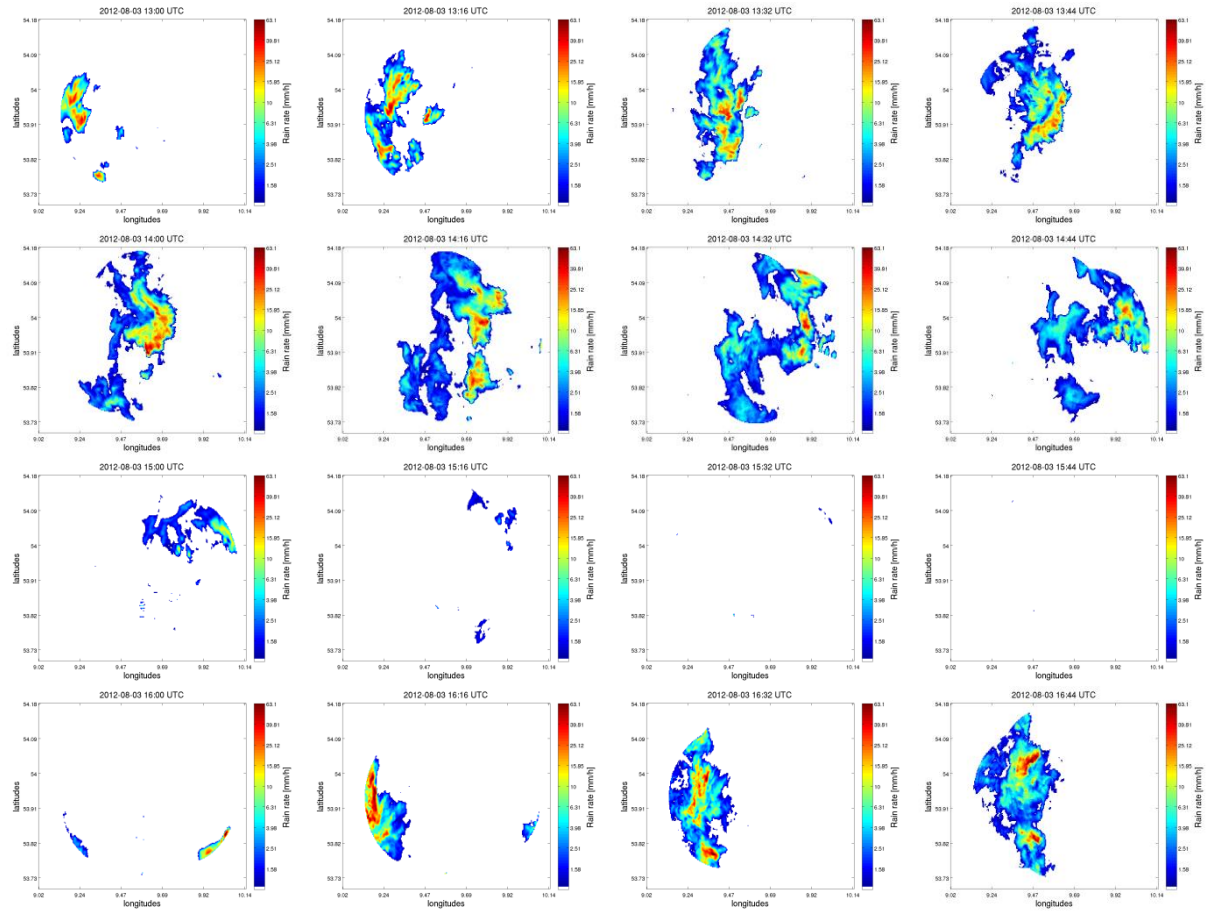


Figure A.4: PATTERN measurements from 2012/08/03, 13 – 17 UTC.

B. Survey of the simulated precipitation events

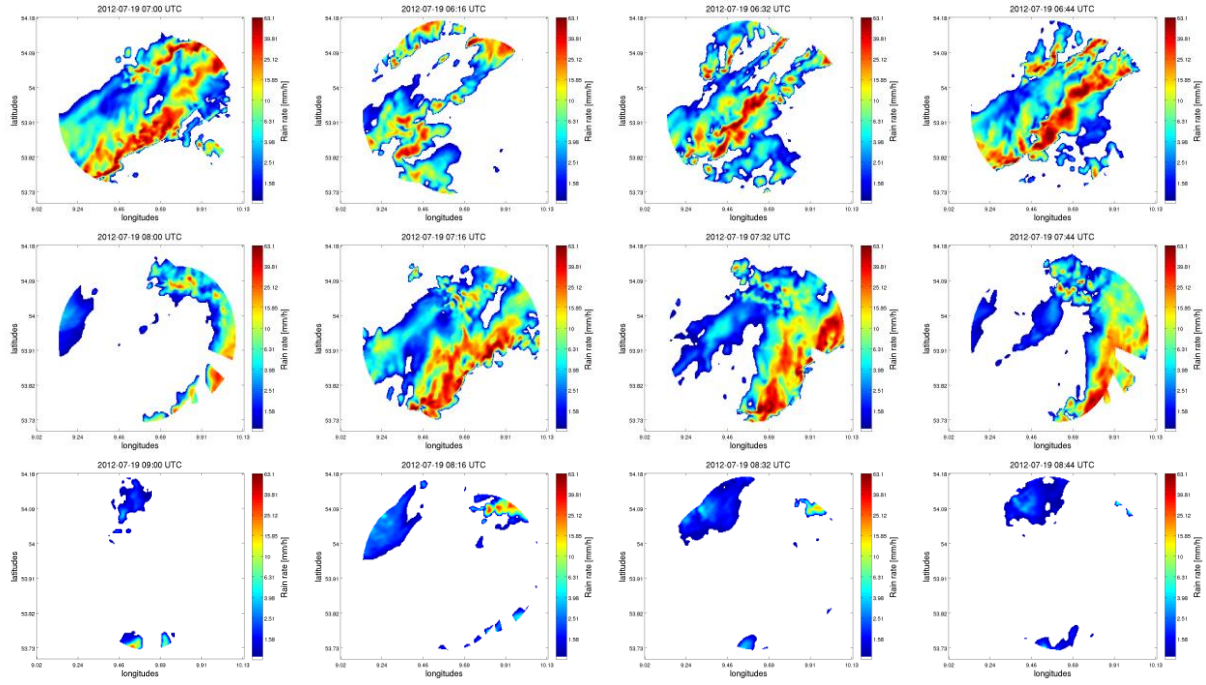


Figure B.1: COSMO simulations from 2012/07/19, 08 – 09 UTC.

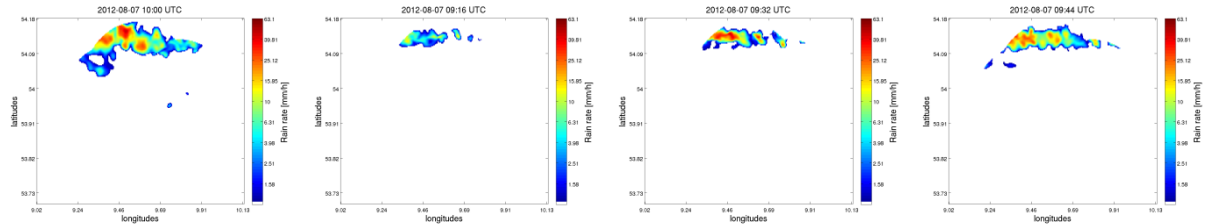


Figure B.2: COSMO simulations from 2012/08/07, 09 – 10 UTC.

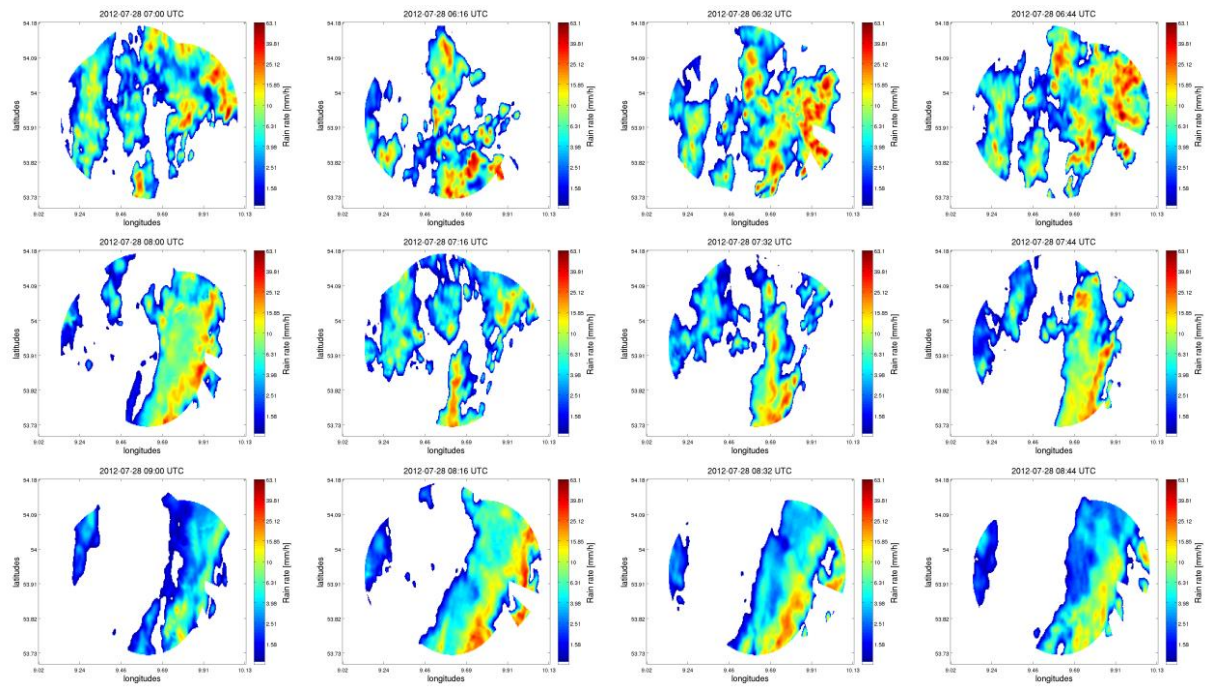


Figure B.3: COSMO simulations from 2012/07/28, 06 – 09 UTC.

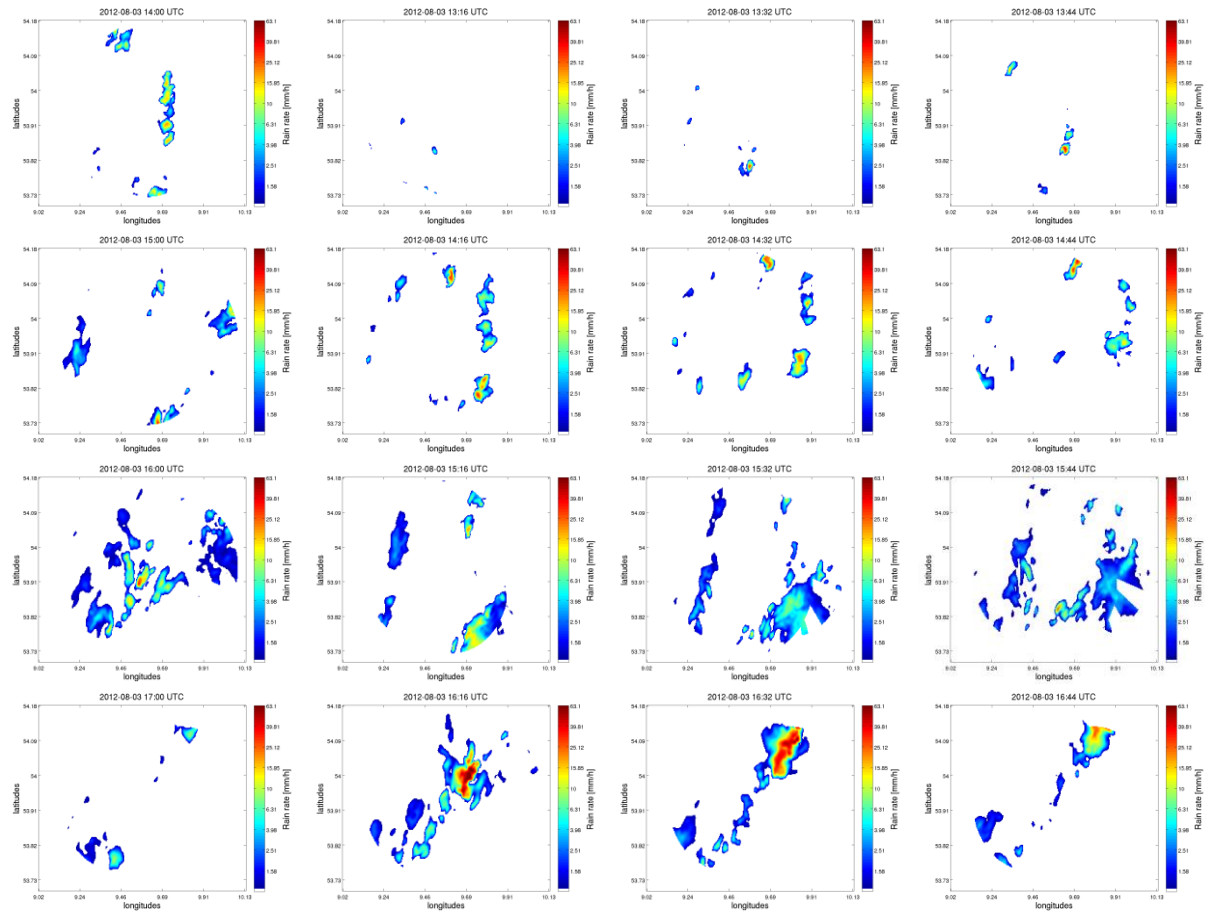


Figure B.4: COSMO simulations from 2012/08/03, 13 – 17 UTC.

Acknowledgement

The making of this master's thesis was only possible with a qualified team of scientific workers behind me. First of all, I would like to express my sincere gratitude to my advisors Prof. Dr. Felix Ament and Dr. Verena Grützun for their professional advice. They always supported me with pleasure and could motivate me when the work began to stumble. Just as well, thanks goes to the whole workgroup of Prof. Dr. Felix Ament because regularly they gave the chance to discuss current problems within the weekly working group meeting. Especially, Dr. Marco Clemens, Katharina Lengfeld and Claire Merker are named here. Their work and experience with the PATTERN radars and precipitation investigations in general could often be a great support. I'm also very thankful for the corrections of my supervisors and David Grawe.

Likewise, motivation was given by my fellow students, especially Timur Eckmann and Akio Hansen with whom I shared an office. Many little discussions always helped to find the right direction, to solve persistent computer and programming problems or they gave reasons to laugh together what boosted the power of endurance.

Finally, I would like to thank my family and all the people that accompanied me temporary for their spiritual support. During a time period of more than one year many things changed also in the private sector. That makes it not always easy to keep going on. Therefore a great thank to all who never doubted about the finishing of this work.

Eidesstattliche Versicherung

Ich versichere an Eides statt, dass ich diese Masterarbeit selbstständig verfasst habe. Ich versichere, dass ich keine anderen als die angegebenen Quellen – insbesondere keine im Quellenverzeichnis nicht genannten Internet-Quellen – verwendet habe und dass die eingereichte Arbeit weder vollständig noch in wesentlichen Teilen Gegenstand eines anderen Prüfungsverfahrens gewesen ist. Die eingereichte schriftliche Fassung entspricht der auf dem elektronischen Speichermedium. Des Weiteren bin ich damit einverstanden, dass ein Exemplar der Abschlussarbeit der Institutsbibliothek zur Verfügung gestellt wird.

X

Ort, Datum, Unterschrift